THE CANADA–FRANCE DEEP FIELDS–PHOTOMETRIC REDSHIFT SURVEY:
AN INVESTIGATION OF GALAXY EVOLUTION USING PHOTOMETRIC REDSHIFTS

by

Mark Brodwin

A thesis submitted in conformity with the requirements
for the degree of Doctor of Philosophy
Graduate Department of Astronomy and Astrophysics
University of Toronto

Abstract

The Canada–France Deep Fields–Photometric Redshift Survey:
An Investigation of Galaxy Evolution Using Photometric Redshifts

Mark Brodwin
Doctor of Philosophy
Graduate Department of Astronomy and Astrophysics
University of Toronto
2004

Progress in the study of galaxy evolution has traditionally followed from improvements in spectroscopic measurement techniques and subsequent groundbreaking surveys. The advent of large format CCD detectors, coupled with the demonstrated success of the photometric redshift method, has given rise to a new, potentially very powerful alternative. It has, in fact, motivated the present detailed investigation of the potential of photometric redshift surveys to complement, or in some cases, supersede traditional spectroscopic surveys in galaxy evolution studies.

This Thesis describes a new deep, wide–field, multi–colour imaging survey, 10 times deeper and 30 times larger than its spectroscopic predecessor, the Canada–France Redshift Survey (CFRS). Highly accurate photometric redshifts, calibrated using hundreds of spectroscopic CFRS galaxies, were measured for tens of thousands of objects, with typical dispersions of only $\sigma/(1+z) \lesssim 0.06$ to $I_{\mathrm{AB}} = 24$ for $z \leq 1.3$.

A new Bayesian method to measure the galaxy redshift distribution is developed. The accuracy of the method, which incorporates the full redshift likelihood function of each galaxy in an iterative analysis, is demonstrated in extensive Monte Carlo simulations. I_{AB} and R_{AB} redshift distributions, along with the run of median redshifts, are measured in various magnitude ranges, with special attention given to quantifying both random and systematic errors.

We measure the evolution of galaxy correlations with redshift, a primary observable of the structure formation process, correcting for the dilutive effect of photometric redshift errors on the clustering signal. The high $z \sim 3$ correlation amplitude seen in this work provides compelling evidence for the biased galaxy formation paradigm. The measured galaxy correlations from $0 \lesssim z \lesssim 3$ are in excellent agreement with the findings of the largest, state–of–the–art spectroscopic studies.

For the 1– and 2–point statistics of the galaxy distribution studied in this Thesis, the measurement accuracy is limited not by the photometric redshift error, but rather by the effect of cosmic variance, whose contribution to the total error budget is dominant. Therefore, future studies will be well served by adopting the photometric redshift approach, the efficiency of which will enable them to survey the hundreds or thousands of square degrees required to obtain a fair sample of the Universe.

This Thesis is dedicated to my grandmothers, Ethel Brodwin and the late Marjorie Dykhuis, and to my parents, Barry Brodwin, Susan Dykhuis and Murray Gold. Your love, support, encouragement, and unswerving faith in me made this work possible, and made me who I am today...

Acknowledgements

Contents

List of Figures

List of Tables

Chapter 1

Introduction

The evolution of the galaxy population has been the almost exclusive purview of spectroscopic redshift surveys over the last quarter century. These pioneering surveys have confirmed the clumpy nature of the galaxy distribution, including the existence of walls, voids and filaments, demonstrated differential evolution between red and blue galaxies to $z \sim 1$, and uncovered a population of normal, star forming galaxies as far back as $z \sim 4$.

In the wake of the convincing demonstration of the photometric redshift method in the Hubble Deep Field (HDF), we designed the present survey to thoroughly test the potential of this novel method as a powerful new tool with which to study galaxy evolution. In this Thesis we compute accurate photometric redshifts in a deep, wide–angle, ground–based imaging survey hundreds of times bigger than the HDF. Further, we conduct a detailed study of the errors inherent in the method, including how to incorporate them in statistical measures of the galaxy population such as the redshift distribution and the two point correlation function. We conclude that the method not only has extraordinary potential, but in fact will take the lead in the next generation of extremely wide–field photometric redshift surveys designed to unravel the process of galaxy formation.

1.1   A Brief History of Galaxy Redshift Surveys

Since the first CFA redshift survey over twenty years ago (Tonry and Davis 1979) a large fraction of the world's telescope time has been devoted to observing larger galaxy samples over longer lookback times. The CFA survey conclusively demonstrated the non-random nature of the 3–D galaxy distribution, in the form of voids, walls and filaments (Davis et al. 1982), providing powerful evidence for the current hierarchical structure formation paradigm. The original goal of the early surveys was to measure the

cosmological parameters — the galaxies were seen as simple tracers of the density distribution embedded in the background cosmology. While the discovery of dramatic evolution in the galaxy population stymied this goal, a new, perhaps more ambitious field of research has emerged: the study of the evolution of the galaxies themselves.

The Canada–France Redshift Survey (CFRS, Lilly et al. 1995b) extended the study of galaxies from the local Universe to $z \sim 1$, when the Universe was half its present age. This survey made the first measurements of the evolution of the luminosity and correlation functions over $0 \lesssim z \lesssim 1$ (Lilly et al. 1995c, Le Fèvre et al. 1996). It also made the first measurement of the star formation history of the Universe since $z \sim 1$ (Lilly et al. 1996).

Following the CFRS another Canadian project, the CNOC2 redshift survey (Yee et al. 2000), focussed on observing a large sample (~ 6000) of relatively bright galaxies in the intermediate redshift regime $0.1 \lesssim z \lesssim 0.6$, allowing a study of the clustering properties of a volume limited sample of galaxies, as a function of brightness and colour (Carlberg et al. 2000, Shepherd et al. 2001). While strongly reliant on galaxy colour, the dependence of the clustering strength on intrinsic luminosity has, until very recently, been difficult to measure with high significance, both locally and at cosmological distances.

The study of the high redshift $z \sim 3$ and $z \sim 4$ Universe was opened up by Steidel et al. (1996; 1999) who combined a photometric preselection technique with spectroscopic follow–up on the 10m Keck telescopes. These surveys isolated galaxies through a flux decrement across the Lα line imposed on their spectrum by intergalactic hydrogen absorption along the line of sight. This highly efficient selection technique allowed hundreds of so–called Lyman Break Galaxies (LBGs) to be studied, leading to measurements of their clustering properties and luminosity density.

The luminosity density at $z \sim 3$ was combined with the measurements at $z \leq 1$ from the CFRS to form the most ubiquitous plot in astronomy over the last few years, the Lilly–Madau plot (Madau et al. 1996), showing the evolution of the cosmic star formation rate, as inferred by the UV luminosity density. The $1 \lesssim z \lesssim 2$ points were filled in soon after using photometric redshifts in the Hubble Deep Field (Connolly et al. 1997). The original studies, which saw a sharp decline in the star formation rate at $z \gtrsim 2$, ignored the effects of dust. Based on template fitting of extinction–corrected spectral synthesis models to spectroscopically confirmed LBGs, Sawicki and Yee (1998) showed that even small amounts of dust have a dramatic effect at high redshift, leading to a star formation rate which rises rapidly from $0 < z < 1$ and remains roughly constant thereafter out to $z \gtrsim 4$. It is interesting to note that the discovery of the $z > 2$ population, as well as an understanding of its spectral characteristics, required photometric techniques.

The high clustering amplitude observed in LBGs, similar to that in the local Universe, provided

the most dramatic observational evidence for a biased picture of galaxy formation, in which the first galaxies to form do so in rare peaks of the underlying dark matter distribution. Following the ideas first elucidated by Kaiser (1984) and developed by Bardeen et al. (1986), these rare peaks should be more highly clustered than the dark matter distribution as a whole. A careful count–in–cells analysis of photometric LBG candidates (Porciani and Giavalisco 2002) provided the first clear evidence of the shallower correlation function slope of the LBGs, as well as the most accurate measurement of the clustering amplitude, both important clues to the origin of these objects. These results were confirmed soon after using the most recent spectroscopic catalogue (Adelberger et al. 2003).

The star formation rate and correlation function are powerful statistical tools we can employ to establish connections between apparently disparate populations observed at different redshifts and in different wavelengths. Due to the close relationship of the 2–point function to the matter power spectrum, surveys designed to measure galaxy clustering trivariate in redshift, luminosity and spectral type offer a unique opportunity to trace the gravitational growth of structure and provide the primary observable to confront theories of galaxy formation.

Despite the rapid improvement in our knowledge due to these surveys and others, there is still considerable uncertainty over the basic cosmography of the Universe due primarily to the effect of cosmic variance. The various statistical measurements of the galaxy population rely on obtaining a fair sample of the Universe, which, until recently, has not been feasible either locally or at high redshift.

Important recent progress in defining the baseline properties of galaxies in the local Universe ($z \sim 0.1$) has been made by two extremely wide–field surveys, the 2dF (Colless et al. 2001) and SDSS (York et al. 2000). These surveys, sampling over 10^3 deg^2, have finally accurately measured the normalization of the local luminosity function (Norberg et al. 2002b, Blanton et al. 2003) as well as the colour– and luminosity–dependent clustering properties of local galaxies (Norberg et al. 2002a, Zehavi et al. 2002). The survey strategies of these local efforts cannot be applied at high redshift since even with the most sensitive detectors and highest multiplexing capabilities available today a deep (AB ~ 24) 10^3 deg^2 spectroscopic redshift survey of objects to $z \sim 1$ and beyond would take $\sim 10^2$ years to complete. Undaunted, two large spectroscopic projects, the Virmos–VLT Deep Survey (VVDS, Le Fèvre et al. 2003) and DEEP2 (Davis et al. 2003), currently underway, will survey a couple of square degrees to this depth over the next few years.

1.2   Weaknesses and Biases Inherent in Spectroscopic Redshift Surveys

While medium to high resolution spectroscopic observations are the only way to study the astrophysics of individual galaxies (e.g. chemical abundances, star formation rates, rotation curves and velocity dispersions), the use of low resolution spectra required in faint galaxy redshift surveys introduces several ubiquitous biases to the resulting galaxy samples.

The main problem is the reliance on strong emission or absorption features in the spectra. For faint galaxies near the survey limit, the galaxy continuum is rarely observed, and the redshift determination depends entirely on the strong emission lines. This property of the technique leads to two important biases and a dangerous potential systematic error.

One major bias is the relative insensitivity to quiescent galaxies with low rates of star formation, and hence low equivalent width emission lines. Another is the lack of sensitivity above $z \sim 1.3$ where [O II] 3727 Å, the only strong emission line longward of Lyα in the observed–frame optical spectrum, must compete with much brighter sky lines, increased fringing and falling detector sensitivity. Between $1.5 \lesssim z \lesssim 2.5$ the lack of bright emission lines has so hindered the sensitivity of traditional spectroscopic searches that it has been dubbed the "redshift desert".

The advent of high–quality near–IR spectrographs should remedy this situation, however the capabilities of current near–IR spectrographs are at least a decade behind their optical counterparts, making them inefficient survey instruments. An original technique to improve the sky subtraction in optical spectroscopy, and hence utilize UV lines normally too faint to detect reliably, is being developed in a new study, the Gemini Deep Deep Survey (Glazebrook et al. 2003). The field sizes are still on the order of arcminutes, however, and do not as yet allow accurate n–point measurements of the galaxy density distribution.

All spectroscopic techniques share a vulnerability to systematic errors in determining redshifts for faint, single emission line objects. There is a substantial risk of misidentifying the spectral line, leading to wildly discrepant redshifts. Multiple observations often simply confirm the single–line nature of the spectrum and hence do not resolve the uncertainty.

While the redshift information obtained for objects with multiple, bright emission lines is essentially error–free, the observational cost involved is quite large. With the advent of multi–object spectroscopy, surveys like the CFRS and CNOC2 were able to simultaneously put slits on $50 - 100$ objects, of which about 85% would yield redshifts. In contrast, the VVDS survey has a multiplexing factor approaching 1000 rendering it far more efficient. However with $\sim 60,000$ galaxies per square degree to AB ~ 24 at

least another order of magnitude in efficiency is needed before spectroscopic surveys of $\gtrsim$ 100 square degrees can be attempted.

1.3 Validation of a New Method: Photometric Redshifts

The idea of using galaxy photometry alone to estimate galaxy redshifts goes back to Baum (1962), with more recent work by Koo (1985) and Loh and Spillar (1986). Despite the promise of these early works the method was not widely adopted by the astronomical community, which viewed it with a fair measure of skepticism.

Not until the acquisition of the ultra–deep *UBVI* Hubble Deep Field (HDF, Williams et al. 1996) images did the photometric redshift method gain widespread acceptance (see conference proceeding edited by Weynmann et al. 1999). In a seminal paper Hogg et al. (1998) compared the photometric redshift estimates of several groups to unpublished spectroscopic redshifts of the same objects. Despite the limited photometric wavelength coverage and the lack of a calibratory sample, the photometric redshift algorithms were accurate for galaxies out to at least $z \sim 1.3$.

As more spectroscopic redshifts in the HDF became available, and the photometric redshift algorithms got more sophisticated, four important properties of the method emerged. First, the photometric redshift method is in principle accurate over the full redshift range $0 \leq z \leq 6$ given contiguous broad–band optical imaging and a least one near infrared band (c.f. Benítez 2000). There is no redshift regime in which the method fails (i.e. no photometric redshift desert).

Since the redshift signal in this method comes from continuum features (such as the 4000 Å and Lyman breaks), the second property of the method is that it is highly independent of galaxy star formation rate. The redshift accuracy, while slightly better for early type galaxies at $z \leq 1.3$ due to their larger 4000 Å break, is conservatively $dz \lesssim 0.1$ for *all* types of galaxies. While this average statistical error precludes doing the kind of science typically reserved for high resolution spectroscopy, it is more than adequate for many statistical studies of the galaxy population.

A rather sobering realization, which emerged from a detailed comparison of photometric redshifts with later, expanded spectroscopic catalogues of the HDF, was the surprisingly large fraction of catastrophic spectroscopic redshift errors caused by incorrect single–line identifications. Rather than a rare problem, the error rate is of order $\sim 10\%$ in final spectroscopic catalogues (e.g. Fernández–Soto et al. 2001). Being fundamentally a continuum method, the third property is that photometric redshifts are immune to this kind of catastrophic error, and should, in fact, be used to confirm all uncertain spectroscopic measurements.

Finally, the fourth and most important advantage of the photometric redshift method is its minimal observational cost. In approximately the time it takes to observe a single spectroscopic mask, it is feasible to obtain deep, multi–band imaging data of sufficient signal–to–noise to produce accurate photometric redshifts for tens of thousands of objects, without regard to galaxy type.

1.4   This Thesis

The primary goal of this Thesis is to conduct a detailed investigation into the properties of photometric redshifts and assess their potential to advance our knowledge of galaxy evolution, in anticipation of the next generation of large imaging surveys such as the CFHT Legacy Survey (CFHTLS). The highest quality subset of the ongoing 1 deg^2 *UBVI* (AB $\sim$ 25) Canada–France Deep Fields (CFDF) imaging survey, supplemented with additional multi–band imaging, was forged into a new *UBVRIZ* Photometric Redshift Survey (PRS). The specific science goals of the CFDF–PRS are as follows:

- Calculate photometric redshifts, calibrated using hundreds of CFRS spectroscopic redshifts, for tens of thousands of galaxies independent of spectral type.

- Analyze the error properties of the photometric method, given our filters and imaging depths, to identify the trustworthy redshift and magnitude regimes, as well as to allow an estimation of *both* the random and systematic errors inherent in their use.

- Devise a method to optimally use the bulk redshift information contained in the galaxy colours to improve the accuracy of statistical analyses of the full galaxy distribution.

- Using the above machinery, make the most accurate measurement to date of the faint galaxy redshift distribution to beyond $z \sim 1$. This information is critical for the extraction of cosmological parameters from a deprojection of the convergence power spectrum in weak lensing cosmic shear studies.

- Measure the galaxy–galaxy angular correlation function in photometric redshift bins, explicitly incorporating the complete photometric redshift probability distributions. Deproject the angular functions using our measured redshift distributions to obtain the evolution of the comoving correlation length over the full redshift range $0 \lesssim z \lesssim 3$.

- Assess the contribution of cosmic variance in our $30' \times 30'$ fields to the total error budget in our statistical measurements, and explore the implications on the relative efficiency of photometric redshift surveys for such measurements.

Chapter 2

Data Observations and Reduction

This chapter describes the acquisition, reduction, and calibration of the Canada–France Deep Fields (CFDF) data set. Due to the scope and complexity of the project considerable attention has been paid to maintaining data integrity and uniformity over the full survey. Although this Thesis is based on the CFDF Photometric Redshift Survey (CFDF–PRS), we describe the reduction of the full CFDF data set in the first few Sections. We turn our focus exclusively to the PRS in Section §2.5 and beyond.

2.1 Observations Log

The CFDF imaging survey consists of data taken primarily from the Canada–France–Hawaii telescope (CFHT) on the UH8k (Metzger et al. 1995) and CFH12k (Cuillandre et al. 2000) mosaic CCD cameras. Supplementary data was taken at Kitt Peak National Observatory's (KPNO) 4m Mayall Telescope and the Cerro Tololo Inter–American Observatory's (CTIO) Blanco Telescope. Table 2.1 provides a Log of the CFDF Observations.

The original survey, undertaken before I joined the project, called for $BVRI$ imaging on the UH8k camera at CFHT. The UH8k is a mosaic of 8 3–edge–buttable 2048×4096 thick CCDs, providing a $28' \times 28'$ field of view. The BVI data was acquired in a series of runs in 1996–1997, but the planned R–band imaging was lost to bad weather. As both the blue and red response of the UH8k is quite poor, supplementary U–band data was obtained on NOAO facilities and Z–data, uncommon even 5 years ago, was not pursued as it was considered beyond the scope of the project.

When I joined the project, simulations of photometric redshift accuracy that I conducted (Brodwin et al. 1999) indicated that R and, in particular, Z–band imaging was required. Supplementary imaging on the successor to the UH8k, the CFH12k, was obtained in these filters for all four CFDF fields. The

CFH12k is a 12 CCD mosaic camera, providing a contiguous $42' \times 28'$ field of view. The thin chips have quantum efficiencies twice that of the UH8k at $\lambda \sim 6000$ Å, and up to 10 times better at the blue and red limits (4000 Å and 10000 Å, respectively). Therefore, supplementary B data was acquired to replace lower quality UH8k data in the 03hr and 11hr fields. Finally, a considerable amount of supplementary CFH12k R– and I–band data was obtained through a shared project with C. Pritchet.

When available CFH12k data was used in place of the original UH8k imaging, as the data is significantly deeper and of much higher quality.

2.2 Preprocessing

2.2.1 Bias, Overscan, and Dark Subtraction

The normally routine operations of bias, overscan and dark subtraction were actually quite involved in the UH8k data. There was considerable non–linear structure in the overscan pattern, which varied from frame to frame. After some testing we found that this pattern could be adequately fitted with a fourth order Legendre polynomial, following which the overscan regions were trimmed.

Removal of the dark current, appreciable in the UH8k ($\sim 0.1\,e^-/s$), was complicated due to a phenomenon dubbed "dark jumping" by the CFHT staff. Briefly, the UH8k's eight chips are arranged in two banks, which are electronically independent. In roughly 20% of exposures all four chips in one or both banks produce an anomalously low dark level. As the dark level is a significant fraction of the total sky counts in typical B band exposures, it was imperative to determine how much dark current, the normal or low level, was under each science image.

To determine this we did two full reductions, consisting of overscan and dark subtraction using both the low and normal mode dark frames. After dividing a twilight flat field one of the two resulting science images generally looked considerably flatter (i.e. had the smallest flat–field residuals). Repeating this for each UH8k frame identified which dark level was present and accurately removed it. The CFH12k images have extremely constant bias and dark properties, and as such, subtraction of a simple medianed dark image worked very well.

2.2.2 Flat Fielding

Whenever good quality twilight flats were available they were applied (using min/max rejection to remove stars) as a first order flat–field correction, designed in particular to remove the pixel–to–pixel sensitivity variations in the CCDs. However, large scale flat–field patterns require a skyflat, or *superflat*,

made from the science data itself. Such flats naturally account for the night sky spectral characteristics and therefore do not require illumination corrections. More importantly they capture the variability, both spatial and temporal, of the night sky in the science fields. In order to detect and extract galaxies uniformly across the images it is imperative to minimize such variations in the final sky flux.

Superflats were constructed using the standard method of dithering the science exposures by the smallest offsets greater than the diameter of the largest objects. In retrospect the ideal dither pattern would have maximally moved the telescope approximately $40'' - 60''$. Unfortunately, many of the original UH8k observations had offsets considerably smaller than this, which necessitated the development of a rather complex masking algorithm to prevent the ghosting caused by incomplete object rejection in the medianing process that creates the superflat.

Toward Better Superflats: Object Masking

We devised an algorithm to produce optimal flat–fields in the presence of an insufficiently large dither pattern. The basic idea is to identify all pixels not representative of the sky background and, using bad pixel masks, omit them from the superflat construction. Typical bad pixel masks take into account bad columns, hot pixels, and other chip defects which are constant from exposure to exposure. We create such a mask by selecting the extreme valued pixels in bright twilight flat images. However, we also have to create an object mask to prevent ghost images from contaminating the superflat.

We run Sextractor (Bertin and Arnouts 1996) with detection parameters designed to extract all bright or extended objects in each image. SExtractor requires a relatively flat input image in order to accurately compute the sky background and rms variation. We therefore first divide out the usual twilight flat–field frame. Due to different gain settings and quantum efficiencies, each chip in mosaic cameras has a unique sky level. In order to produce a final science image with a uniform sky background, we scale the flat–fields in each chip by the reciprocal of the mean sky level near the centre of the mosaic. In the rare cases where a suitable twilight flat was unavailable, we substituted a rough superflat consisting of the simple median of the science images. In this case severe ghosting patterns are produced, but the resulting images are only used to extract an object catalogue and are discarded afterwards.

With this object catalogue in hand, along with a SExtractor estimate of the area and FWHM of each object, we developed an automated procedure that extends the masked region by dropping a circle of diameter $f \times$FWHM centered on the object position. The parameter f, varied from 1.3 to 2.0 depending on the object area. Thus we extend the rejected pixels down into the wings of each object.

We also developed a procedure that allowed an interactive assessment of the object mask, including the option to recompute it with a change of SExtractor or mask extension parameters. Finally, direct

manipulation of the object mask was performed, masking areas omitted by the above procedure, in particular regions containing scattered light and satellite trails.

With the final bad pixel and object masks in hand, a final superflat image consisting only of valid sky pixels was generated. The sky itself was variable on a timescale of 3–5 hours, less for the Z–band. We applied temporally proximal superflats to the twilight sky flattened images, or, in the absence of twilight flats, directly to the dark–subtracted images. An example of the results of this algorithm is shown in Appendix A (Figure A.1).

2.2.3   De–Fringing the CFH12k Images

As is common in CCDs with thin chips, fringing was a problem at the longer wavelengths in the CFH12k data. The fringing was negligible in the R–band, but had to be removed in the I– and Z–bands where it added variations of $\sim 5\%$ and $\sim 10\%$, respectively, to the sky background. The magnitude of the fringing forced a change to the superflat procedure described above, as the presence of the fringes prevented SExtractor from working properly. Our philosophy remained to render the background as flat as possible, accepting that our procedure may corrupt the photometric integrity at the $\sim 1\% - 2\%$ level. Photometric error at this level is negligible compared with the systematic error that can be introduced into the galaxy detection process by a varying sky background. The modified routine is as follows.

A simple median of the dark–subtracted sky frames was used to produce an initial fringe frame, by subtracting off the average of the median and the mean of the sky value in each chip. What remains is the fringe pattern, contaminated by a second order ghosting effect. This was found to not be severe since the fringe frame is subtracted off rather than divided out.

The `rmfringe` task of the `mscred` package distributed with the IRAF[1] reduction environment was used to scale each chip of the initial fringe frame to best correct a reference image (i.e. one image in a temporally contiguous set of observations). In practice a single scale factor did not optimally remove the fringe pattern across the full mosaic, and therefore individual scale factors were determined for all 12 chips. The final fringe frame was constructed by appropriately scaling each chip of the initial fringe frame. This final frame was then subtracted from each science frame in a short series of exposures, scaled to each successive frame by the ratio its sky counts to those of the reference image. In practice the scaled fringe pattern was only stable on the timescale of 2–3 hours, after which time a new reference image with new scalings in each chip was required.

After removal of the fringing, the usual superflat algorithm described above is implemented to produce

---

[1]IRAF is distributed by the National Optical Astronomy Observatories, which are operated by the Association of Universities for Research in Astronomy, Inc., under cooperative agreement with the National Science Foundation.

the final flat science frames. An example of the fringe frame correction is presented in Figure A.2.

2.3 Astrometric Correction

In order to produce distortion–free images with a uniform pixel scale we devised a two step astrometric correction procedure. In each field we project each chip of a reference image onto a common, undistorted, astrometrically calibrated plane, the center of which is the tangent point of the mosaic and is coincident with its optical center. We then derive an extremely precise *relative* astrometric solution using a large catalogue extracted from the reference image itself. Thus we can accurately project all our pointings in all filters to the same undistorted plane.

We used the larger CFH12k images for reference images as they are a superset of the full *UBVRIZ* multi–colour data set (i.e. smaller UH8k and NOAO pfccd quadrants could be easily mapped onto the full CFH12k area). We used I–band or Z–band CFH12k reference images as they typically had the highest number of objects. The absolute world coordinate system (WCS) of the reference image was computed using the United States Naval Observatory (USNO A2.0) catalogue (Monet 1998) as an external reference, using a third order polynomial to adequately map the camera distortions in each chip.

The reference image was then projected to the tangent plane using a 17×17 pixel^2 sinc interpolation kernel. We found the sinc interpolation was superior to the polynomial interpolations, as the latter left residual large scale fringe–like patterns in the sky background. The rare cases where ringing occurred with the sinc kernel did not affect the data because, as they were typically in the regions around saturated stars and chip defects, they were carefully masked out as described in Section §2.6.

The USNO A2.0 catalogue, with typically 40–80 stars in each chip of our reference image, produced a root–mean–square (RMS) dispersion in the astrometric solution of $\sim 0.3'' - 0.4''$. This is the absolute accuracy of the CFDF astrometry. An example, showing the USNO stars overplotted on CFDF data is shown in Figure A.3.

We required much better registration in order to combine our multiple pointings in each band, and to measure accurate colours from filter to filter. In fact, our science goals required a maximum RMS registration error of $\lesssim 1$ pixel ($0.206''$) over the full 8092×8092 pixels^2 common to our full multi–colour data set.

The WCS of the reference image was copied to all subsequent pointings in the same field. We then extracted a large catalogue (~ 3000) of bright, compact objects from our reference image and interactively improved the astrometric solutions of all subsequent pointings using this much larger catalogue, adjusting

for tangent point shifts and slight rotations of the camera. This internal astrometric solution had RMS registration errors of better than $0.1''$, or about half a pixel. After projecting these images to the tangent plane, the slight residual sky gradients not corrected by flat–fielding were fitted and removed.

We corrected for seeing and transparency variations using the `mscimatch` task. This consists of fitting an additive sky brightness correction and a multiplicative transparency correction to thousands of bright objects across the field. Thus all the images were effectively photometrically calibrated to the reference image. The projected images were then stacked using a median combine with a clipped 3–σ rejection algorithm, subject to bad pixel masking of chip defects.

This procedure was repeated for all the other filters, using the large catalogue extracted from the reference image as the astrometric catalogue. A simple linear offset, computed and executed using `geomap` and `geotran`, respectively, is sufficient to map all additional filters onto the original I–band reference frame.

The four U–band quadrant images and some of the UH8k final stacks, created with identical procedures before the CFH12k data acquisition was complete, were similarly mapped onto the final CFH12k WCS. Although this involved another interpolation the RMS astrometric error in the full CFDF is $\sim 0.08''$ (~ 0.4 pixels) for both the UH8k and CFH12k stacks, and slightly worse (~ 1 pixel) for the U–band data over the full field of view. Thus we achieved the astrometric accuracy needed to measure the robust colours required for reliable photometric redshifts.

2.4 Photometric Calibration

Our instrumental magnitudes were calibrated to AB magnitudes in our native filter system using standards from Landolt (1992) and Christian et al. (1985). We reduced the standards exactly as the science images, including bias, overscan and dark subtraction, twilight flat correction, de–fringing if necessary, and superflat correction. The final astrometric solution was applied and the standards were projected onto the tangent plane. This process produced uniform, distortion–free standard images. We did not combine the standards, preferring instead to derive airmass corrections where possible from sequences of standard star exposures. However as our fields were all observed quite close to zenith, the extinction corrections are small. All standards were visually inspected, and saturated stars and stars falling on CCD defects were removed.

Sample airmass and photometric calibration plots from the 03hr field are shown in Figure 2.1.

Table 2.1. CFDF Observations Log

Field	R.A./Dec. (J2000)	Band	Exp. Time (hours)	Seeing (arcsec)	Area (deg^2)	Telescope/ CCD	Date (mm/yy)
0300+00	03:02:40	U	10.8	1.0	0.25	CTIO/pfccd	06/97
	+00:10:21	B	2.0	0.80	0.33	CFHT/CFH12k	10/00
		V	4.2	1.3	0.25	CFHT/UH8k	12/96
		R	1.5	0.95	0.33	CFHT/CFH12k	[09,10,11]/00
		I	6.2	0.70	0.33	CFHT/CFH12k	[09,10]/00
		Z	4.8	0.65	0.33	CFHT/CFH12k	10/00
1415+52	14:17:54	U	10.0	1.4	0.25	KPNO/pfccd	03/97
	+52:30:31	B	5.3	0.8	0.25	CFHT/UH8k	06/97
		V	2.3	1.0	0.25	CFHT/UH8k	06/97
		R	1.0	0.95	0.33	CFHT/CFH12k	04/00
		I	2.6	0.70	0.25	CFHT/UH8k	06/97
		Z	5.0	0.70	0.33	CFHT/CFH12k	04/99, [03,04]/00
2215+00	22:17:48	U	12.0	1.4	0.12	CTIO/pfccd	06/97
	+00:17:13	B	5.5	0.8	0.25	CFHT/UH8k	09/97
		V	2.7	1.0	0.25	CFHT/UH8k	06/97
		R	1.2	0.90	0.33	CFHT/CFH12k	[09,10]/99
		I	6.3	0.75	0.33	CFHT/CFH12k	[09,10]/99
		Z	4.0	0.52	0.33	CFHT/CFH12k	10/00
1130+00	11:30:02	B	1.0	0.90	0.33	CFHT/CFH12k	04/00
	-00:00:05	V	3.3	0.8	0.25	CFHT/UH8k	05/97
		R	1.0	1.0	0.33	CFHT/CFH12k	04/00
		I	7.4	1.0	0.25	CFHT/UH8k	12/96,05/97
		Z	4.3	0.8	0.33	CFHT/CFH12k	04/99, 04/00

Note. — Some of the original UH8k BVI imaging was replaced with superior CFH12k data.

U–data only exists in the 03hr, 14hr and half of the 22hr field.
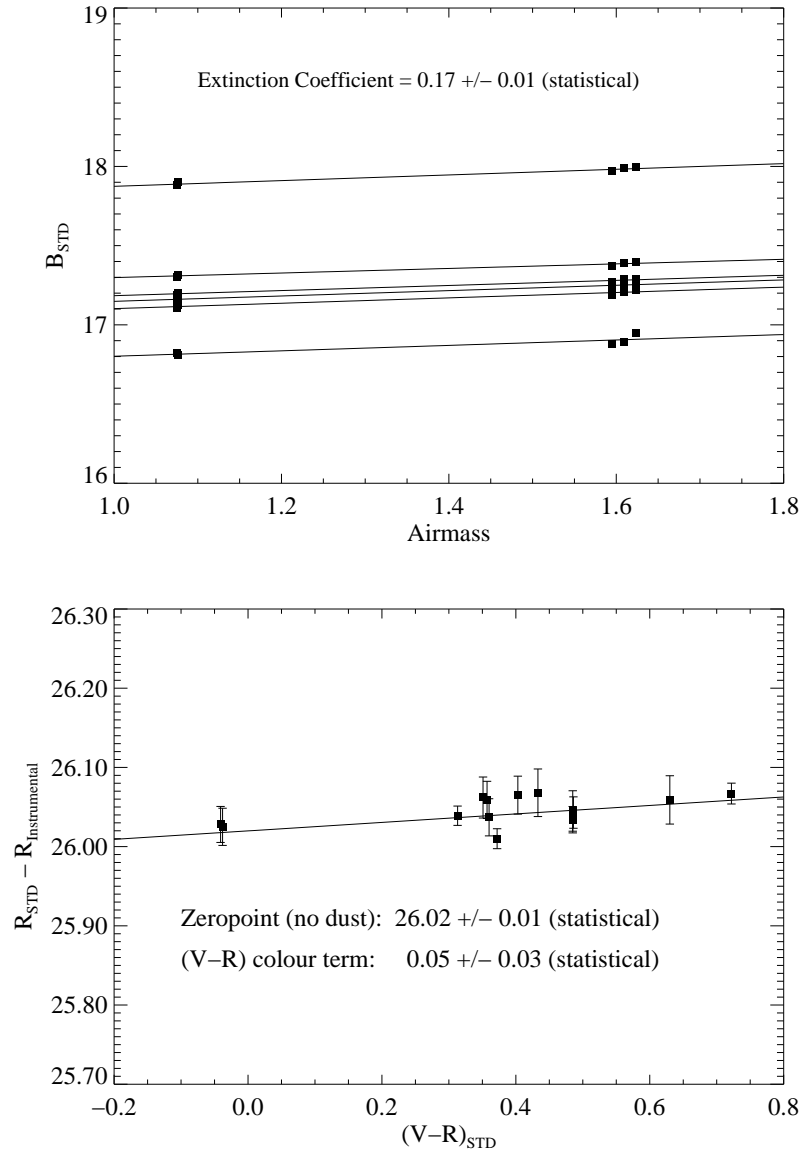
Figure 2.1 *Top:* Extinction curves for standard stars in the *B*–band. The error bars are smaller than the symbol size for these bright standards. *Bottom:* Photometric calibration in the *R*–band for stars corrected to 1 airmass. The colour and airmass terms derived in the CFDF agree with the values provided by CFHT.

2.4.1 Z–band Calibration

Because faint Z–band standards were not available when the CFDF data was acquired, we extrapolate the Z–band zeropoint from our other photometry by exploiting the roughly linear relationship between the $(V-I)$ and $(I-Z)$ colours of main sequence stars. Put simply, we can predict the Z magnitudes of the main sequence stars in our science fields using their measured V and I magnitudes, and therefore use these stars as standards to derive the Z–band zeropoint. This method has been used before (e.g. Karkut 1998), usually under the assumption that the main sequence passes through $(V-I) = (I-Z) = 0$.

Using 24 main sequence model spectra between O5V and M6V taken from Kurucz (1996), we compute the stellar colours in the CFDF filter set. As Figure 2.2 shows the colour–colour plot is indeed quite linear and very nearly goes through the origin. Of course in the CFDF we expect a much redder distribution of stars given the shape of the stellar initial mass function.
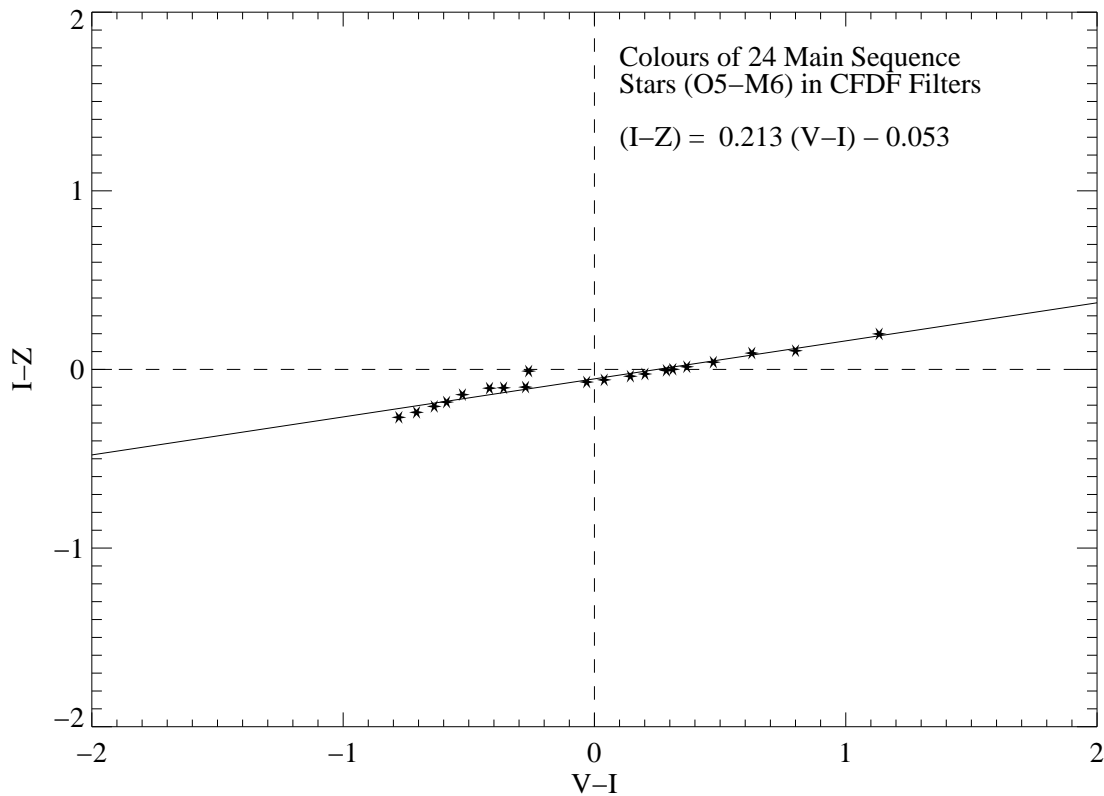
Figure 2.2 $(I-Z)$ vs. $(V-I)$ colour–colour plot for model main sequence stars from Kurucz (1996). The linear relation passes near, but not through, the origin for the CFDF filter set.

Encouraged by this confirmation of the method, we plot in Figure 2.3 $(I-M_Z)$ vs. $(V-I)$ for bright, unsaturated stellar objects in the CFDF 14hr field, where M_Z is the instrumental Z–band magnitude. We morphologically isolate stars using the SExtractor neural network star/galaxy classifier (CLASS_STAR).

14hr Z–band calibration

$$(I–M_Z) = 0.194 \, (V–I) + 24.77$$

Class_Star > 0.98

$$(I–M_Z) = 0.218 \, (V–I) + 24.75$$

$(V–I)_{\text{Vega, no dust extinction}}$
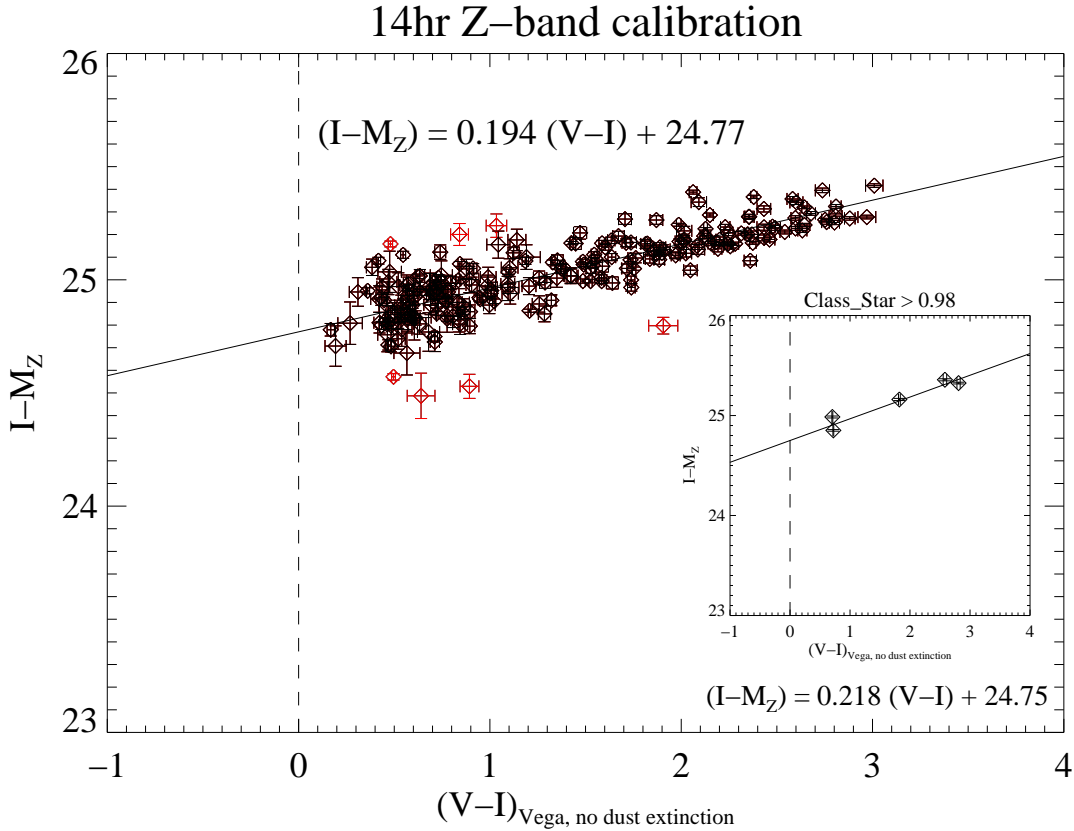
Figure 2.3 $(I - M_Z)$ vs. $(V - I)$ colour–colour plot for bright, unsaturated, morphological stars in the 14hr field. The Z–band zeropoint is extrapolated from this linear relation (see text). *Inset:* The same relation for only the most certain stars. The slope exactly matches that of the model star colour–colour relation (Figure 2.2).

The Figure shows all stars (CLASS_STAR > 0.95) with $18.5 < V_{\text{AB}}, I_{\text{AB}} < 22.0$. The red objects are rejected as $\geq 3\sigma$ outliers. A straight line fits the data very well, with the extrapolation to the origin of $(V - I)$ identifying the Z–band zeropoint, ignoring for the moment the small (~ 0.05) offset discovered in Figure 2.2. The slope is quite close to that predicted for main sequence stars as well, giving confidence in both the stellar selection and the method in general. In fact when a stricter morphological stellar selection is made (CLASS_STAR > 0.98, see inset of Figure 2.3), the predicted slope is precisely matched within the statistical error (0.007).

The formal statistical error on the Z–band zeropoint was only ~ 0.01, which obviously underestimates the true error. We nominally take the zeropoint error to be at least 0.05, based on the model stellar spectra of Figure 2.2, and from the field–to–field variance of the derived Z–band zeropoints. At this point we don't adjust the zeropoints for the offset predicted by the model stars, as we further refine the photometric calibration using the CFRS spectroscopic redshift sample in Section §4.2.

Table 2.2. Schlegel et al. (1998) Dust Extinction Corrections

Field	l	b	$E(B-V)$[1]
0300+00	177.60	-48.25	0.097
1415+52	96.38	60.06	0.009
2215+00	63.28	-43.97	0.061
1130+00	263.80	56.56	0.023

[1] Reddening values are linearly interpolated from the nearest 4 pixels in the Schlegel et al. (1998) dust maps.

2.4.2 Galactic Extinction Correction

Our zeropoints were corrected for galactic absorption using the $E(B-V)$ values in our fields from Schlegel et al. (1998) dust maps, listed in Table 2.2. We adopt an $R_V = 3.1$ extinction curve, where R_V is the ratio of the V–band extinction and the relative extinction between B– and V–bands, $E(B-V)$. To derive the dust extinction correction in each filter, we multiply the $E(B-V)$ values in Table 2.2 by $A_i/[E(B-V)] = \{4.968, 4.320, 3.315, 2.634, 1.940, 1.540\}$ for $i = \{U, B, V, R, I, Z\}$, where these values are extrapolated from Schlegel et al. (1998) for filters with our effective wavelengths.

2.4.3 Conversion to AB Magnitudes

We convert our magnitudes to the AB system of Oke (1974), computing the specific offsets for our filter/QE combination. We list in Table 2.3 the offsets for all the filters used in the CFDF. For simplicity we scale our calibrated images to a common AB zeropoint of 30.0, such that

$$\text{AB} = 30.0 - 2.5 \log(\text{counts}) \tag{2.1}$$

in all bands.

2.5 CFDF Photometric Redshift Survey

In order to produce accurate and reliable photometric redshifts, the full CFDF survey was culled down to approximately half the original survey size, keeping only the fields containing high quality 6 band *UBVRIZ* photometry. As Table 2.1 shows, U–band imaging only exists in 2.5 of the original 4 CFDF fields. It has been convincingly demonstrated (Gwyn 1995, Brodwin et al. 1999) that accurate pho-

Table 2.3.   AB Offsets for CFDF Filters

Filter	Camera	AB offset
U	KPNO pfccd	0.739
	CTIO pfccd	0.798
B	UH8K	-0.131
	CFH12K	-0.133
V	UH8K	0.002
R	CFH12K	0.226
I	UH8K	0.447
	CFH12K	0.447
Z	CFH12K	0.567

Note. — Magnitudes are computed as AB = Vega + AB offset

tometric redshifts at $z < 0.5$ require U–band data in the absence of infrared imaging. We therefore summarily reject the 11hr field, along with the half of the 22hr field lacking U–data.

Additional conditions for accurate photometric redshifts include an accurate photometric calibration and the existence of a spectroscopic training set to tweak the redshift algorithm. In particular, the CFDF Z–band zeropoint is not precisely known (see above). In §4.2 we use the CFRS spectroscopic sample to improve our photometric calibration and hence our redshift accuracy. As the 11hr field is not an original CFRS field and has no such training set, we feel its removal is justified for the PRS component of the CFDF.

The final CFDF–PRS area therefore consists of the three CFRS fields targeted in the original CFDF — the 03hr and 14hr fields, along with half of the 22hr field. These fields cover approximately $\frac{5}{8}$ deg^2, but the PRS area is further reduced by detailed masking of photometrically unreliable areas as described in the next Section.

2.6   Masking of Saturated Stars and Residual CCD Defects

With the calibrated CFDF–PRS stacks in hand, we now perform a detailed masking of bright, saturated stars (and ensuing charge bleeding), scattered light caused by inadequate baffling (common in UH8k data), remnant cosmetic CCD defects that survived the median stacking, and an entire UH8k CCD whose abysmal charge transfer efficiency (CTE) renders it photometrically non–linear and hence useless.

The final 14hr Z–band image is shown in Figure 2.4 with the masked areas, consisting of circular and rectangular regions, overlayed. While some masked areas appear problem–free in this Z–image, they are rejected based on unacceptable features in one of the other PRS bands. Figure 2.5 schematically shows the masked areas in the full PRS. All objects down to $I_{AB} = 24$ are plotted, with the rejected objects in red. The 03hr and 22hr fields are on the upper and lower left, respectively, and the 14hr field is on the right.

The area common to the UH8k and CFH12k cameras is in the central 8 CFH12k chips. Comparing this Figure with Figure 2.4 we see that there is no I–band data in the top and bottom CFH12k chips in the 14hr field, which makes sense as this field only has UH8k imaging in the I–band (see Table 2.1).

The Figure also shows examples of the various reasons for masking. Aside from ubiquitous saturated stars, we see the long, thin, diagonal areas (masked as a linear sequence of circles) rejected in Figure 2.4 due to scattered light in the UH8k images. The chip at the lower left of the 14hr UH8k region is the one rejected due to bad CTE. It is visibly rejected in the 03hr field as well, this time on the upper right. Fortunately the bad UH8k chip falls in the lower half of the 22hr field, which is already rejected for lack of U–band data. Therefore the full 0.125 deg^2 that was imaged in U is usable in the PRS.

Only the unmasked area in *all 6 filters* is accepted as part of the CFDF–PRS. This extremely conservative cut leaves only 0.45 deg^2, or less than half of the original survey area, but the remaining data is of very high quality and uniformity, and has the wavelength coverage necessary for robust photometric redshifts.

2.7 Catalogue Extraction

Rather than detect objects in a single filter, we have chosen to employ an optimal multi–band detection method. Following Szalay et al. (1999), we construct a χ^2 detection image from which we extract the CFDF–PRS catalogues. The χ^2 detection image is the quadrature sum of the images in each band, weighted by a noise map,

$$\chi^2 = \frac{1}{n} \sum_{i=1}^{n} \left(\frac{a_i}{\sigma_i} \right)^2, \tag{2.2}$$

where a_i and σ_i are the i–th background–subtracted image and noise map, respectively, and n is the number of broadband filters. The χ^2 image is therefore a pixel by pixel weighted sum of the multi–colour imaging. The variance maps suppress the rate of false extractions due to noise spikes, while allowing faint object detection in smoother regions.

We ran SExtractor twice to produce both the background–subtracted pixel values (a_i) and the variance maps (σ_i^2) in each band. We median smoothed the resulting χ^2 image using a 3×3 pixel^2 kernel

to reduce the small–scale noise, introduced by the relatively inferior blue UH8k data, on the basis that structure on scales smaller than this smoothing kernel ($\sim 0.6''$) is simply noise. The final SExtractor extraction parameters were determined empirically and are listed in Table 2.4. Note the deblending parameters are set to maximally allow the separation of nearby objects. A detailed examination in all three fields showed that the only cases where single objects were incorrectly split into two or more detections were on or near massively saturated stars, which are masked out of the final catalogues anyway.

Table 2.4   SExtractor Extraction Parameters

```
#----------------------------- Extraction --------------------------------

DETECT_MINAREA  2                     # minimum number of pixels above threshold
DETECT_THRESH   2.0                   # <sigmas> or <threshold>,<ZP> in mag.arcsec-2

FILTER          Y                     # apply filter for detection ("Y" or "N")?
FILTER_NAME     sex/gauss_2.0_3x3.conv # name of the file containing the filter

DEBLEND_NTHRESH 64                    # Number of deblending sub-thresholds
DEBLEND_MINCONT 0.000001              # Minimum contrast parameter for deblending

CLEAN           Y                     # Clean spurious detections? (Y or N)?
CLEAN_PARAM     1.0                   # Cleaning efficiency
#-------------------------------------------------------------------------
```

After a careful inspection of the χ^2 images in each field, we concluded that the bluer filters were contributing substantial noise to the final detection image, offsetting in a sense the vastly superior red (RIZ) CFH12k images. We elected to exclude the noisiest blue filters in each field, so as to minimize the degradation of the χ^2 image while retaining sensitivity to the bluest objects. Specifically, our final χ^2 images are composed of $\{BRIZ, UVRIZ, BVIZ\}$ in the $\{03\mathrm{hr}, 14\mathrm{hr}, 22\mathrm{hr}\}$ fields. The 22hr R data, acquired as shared data with C. Pritchet (see §2.1), was omitted from the detection image as it was not adequately dithered to cover the gaps between the chips, leading to unacceptable artifacts in the final χ^2 image.

It is important to point out that while we use these χ^2 images to detect objects down to the faintest flux levels, our primary science analyses are based on objects detected at $\geq 10\sigma$ in the I band (see Section §5.3.2). Therefore the issue of which blue bands were used in each field for the construction of the χ^2 detection image is of no consequence.

2.8   CFDF–PRS Photometric Catalogue

Using SExtractor in double–image mode, we measured total magnitudes (MAG_AUTO) for every object detected in the χ^2 images, along with morphological parameters such as the full width at half–max (FWHM) and peak flux. We use these total magnitudes to define our magnitude–limited samples and for best–estimate magnitudes of individual objects. However for photometric redshifts accurate colours are required, and we therefore measure aperture magnitudes as well.

Although large apertures provide the most robust colours, our fields are sufficiently deep that crowding becomes a significant issue for faint galaxies. We therefore conducted tests to determine the smallest diameter with which aperture magnitudes faithfully reproduce the colour–colour diagram of stars taken with larger apertures. We arrived at a minimum diameter of $2.5''$, which is approximately twice our worst seeing.

Accurate colours require similar seeing in all bands. We convolved all our images to match the point spread function of the worst seeing image in each field ($1.3'' - 1.4''$), and measured $2.5''$ diameter aperture colours using the `apphot` package in IRAF. We also measured a concentration parameter, the ($0.75'' - 3''$) aperture magnitude difference, in the best–seeing unconvolved Z–band image, discussed further in Section §3.4.

2.8.1   Magnitude Errors

For a photometric redshift survey, the errors on the magnitudes are at least as important as the magnitudes themselves. This is because it is the magnitude errors that effectively select the best–fit template spectrum, by weighting the flux in each band. In standard photometry packages magnitudes errors are estimated as the quadrature sum of the Poisson errors in the object and sky fluxes (measured in an aperture around the object), along with an estimate of the error in the sky background level measurement. These error estimates are strongly dependent on the assumption that the sky noise is uncorrelated (i.e. that Poisson statistics apply). For objects fainter than the sky background, the Poisson sky error is the dominant contribution to the magnitude error.

The fringe and superflat frames derived from the data itself de–fringe and flatten the images extremely well, but also correlate the sky noise on small scales. This correlation causes a large underestimate of the Poisson sky noise when only measured in the immediate vicinity of each object, as is common with photometry packages. Indeed, the errors estimated by both SExtractor and IRAF, while similar to each other, significantly underestimate the Poisson sky error directly measured in the raw data. As we were unable to trust the magnitude errors reported by both IRAF and SExtractor, a separate error estimate

Table 2.5.   Final AB $5\sigma/2.5''$ Photometric Sensitivities in the CFDF–PRS.

Field	U	B	V	R	I	Z
03hr	25.17	25.41	25.04	25.15	25.04	24.26
14hr	25.88	25.33	25.04	25.21	24.51	24.47
22hr	25.96	25.23	25.18	25.42	25.36	24.65

was devised.

We estimate the true sky noise by measuring the flux in ten thousand $2.5''$ diameter apertures placed randomly throughout the unmasked areas of our images and computing a histogram of the measured aperture flux counts. The majority of the time we expect to photometer empty sky — even the Hubble Deep Field is fully $\sim 95\%$ sky pixels (Gardner and Satyapal 2000) — and therefore the standard distribution of the histogram gives a direct measure of the true sky noise. By chance we will occasionally photometer parts of galaxies, however these will all be positive definite. We therefore fit a Gaussian to only the negative side of the distributions to derive the Poisson sky error in $2.5''$ apertures in each band. The distributions for the 22hr field are shown in Figure 2.6.

We take these measured sky errors as the final flux errors in the CFDF–PRS, subject to the constraint of a minimum 5% magnitude error. Despite substantial effort to maintain rigorous control of systematics in the reduction pipeline, we cannot exclude the possibility of systematic band–to–band uncertainties at this level.

We ignore the contributions to the magnitude error due to the object flux and the uncertainty in the sky level estimate. The former is only important for the brightest objects, which have statistical Poisson magnitude errors well below our minimum systematic error. The latter is not relevant in our analysis as we don't estimate the sky noise locally assuming Poisson statistics, rather we measure it directly. The final photometric sensitivities for the CFDF–PRS are presented in Table 2.5.

We have also confirmed that a similar, simpler method to estimate the sky variance produces essentially identical results. We bin the final images such that each individual pixel represents the area of circular $2.5''$ apertures in the unbinned images. This mitigates the effect of small–scale correlations introduced by the reduction procedure. A simple standard deviation of the pixel values in these binned images produces results consistent with our simulations.

With final catalogues in hand, we proceed to verify the integrity of the CFDF–PRS data by subjecting it to a variety of internal tests and comparisons with other surveys.
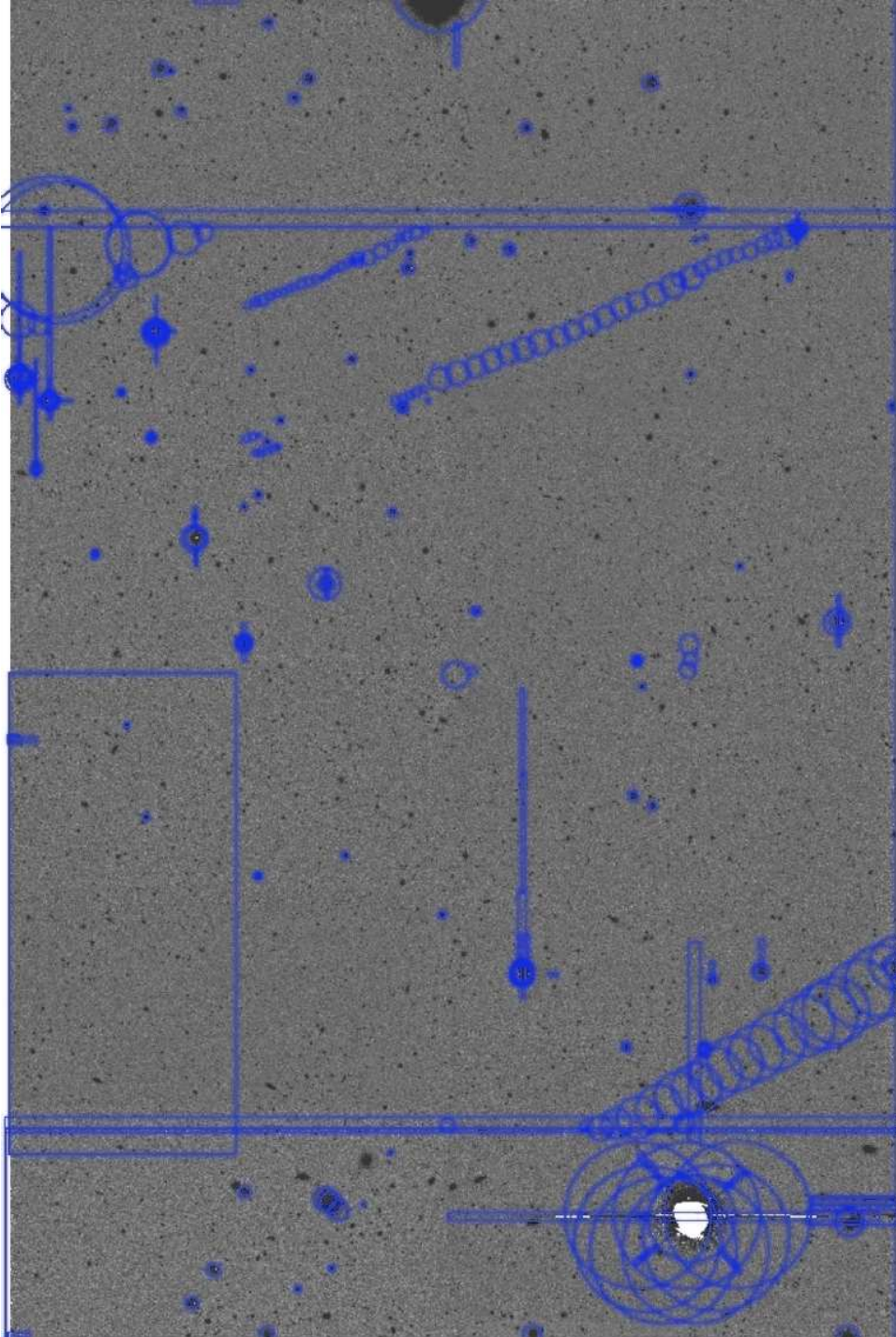
Figure 2.4 Masked regions plotted on the Z–band image in the CFDF–PRS 14hr field.
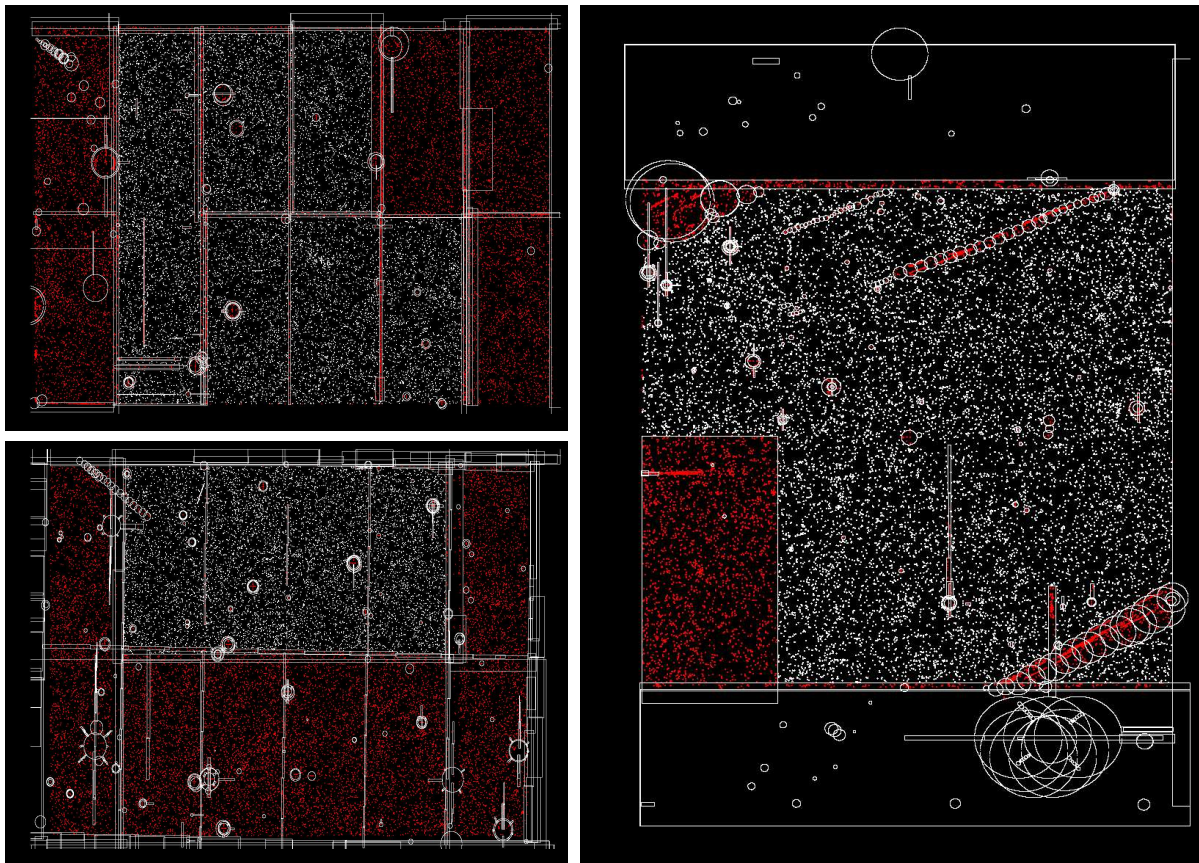
Figure 2.5 CFDF–PRS objects down to $I_{AB} = 24$. The objects removed from the final PRS catalogue are plotted in red. Only those objects with full *UBVRIZ* photometry are used in the PRS. The 03hr and 22hr fields are at upper and lower left, respectively. The 14hr field is on the right. Note that all fields are the same size — they are only scaled differently for this Figure. See text for a description of the features displayed here.
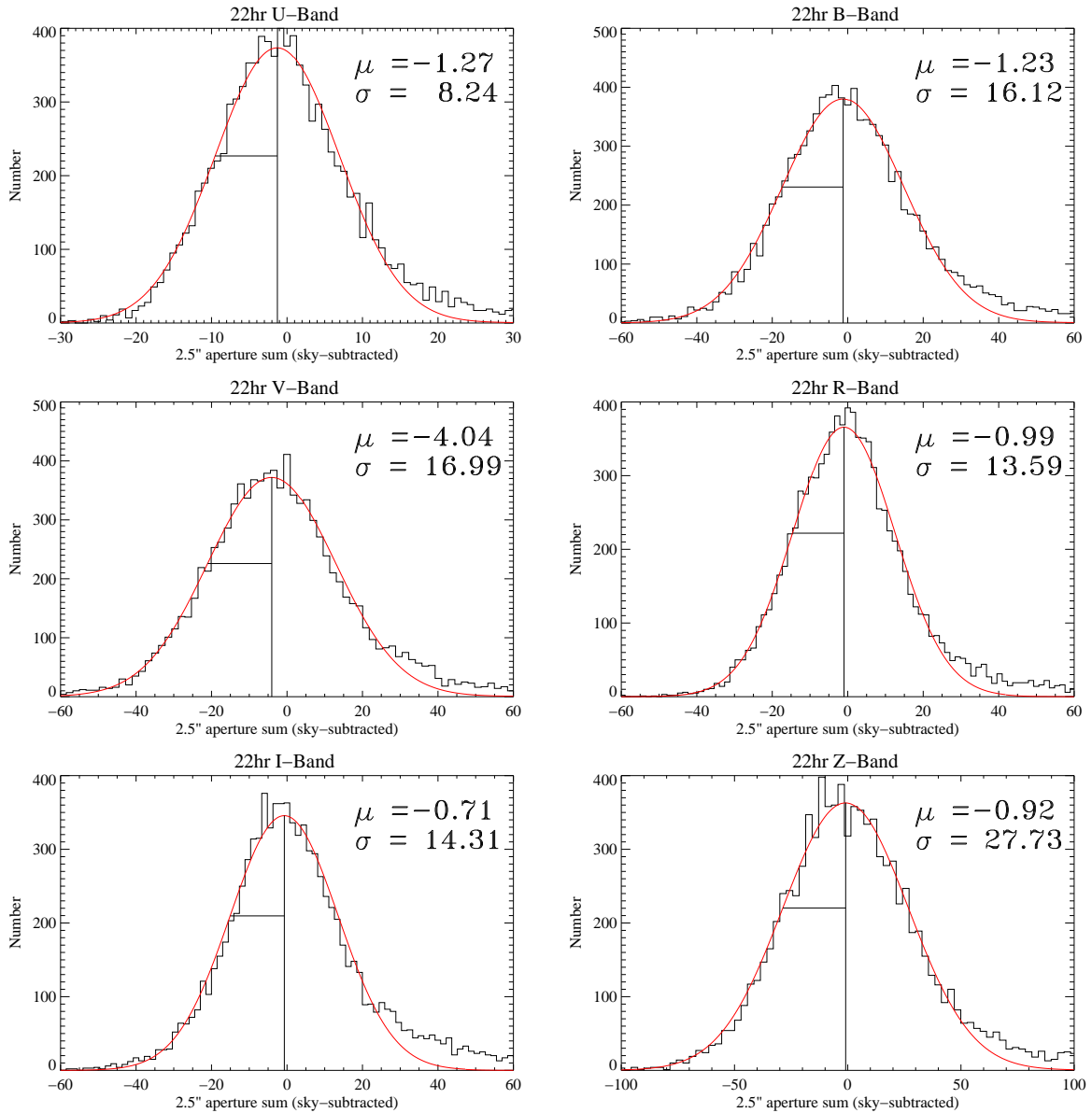
Figure 2.6   Sky noise histograms in 2.5″ diameter apertures for the 22hr field in ADUs, where $AB = 30.0 - 2.5 \log(\text{counts})$. Parameters for the best–fit Gaussians, fitted only to the negative flux values, are listed in each panel.

Chapter 3

Data Characterization and Verification

In this Chapter we present some of the tests that were conducted to ensure the scientific integrity of the final CFDF–PRS dataset. We compare our final photometric calibration against the external CFRS (Lilly et al. 1995b) photometry, verify that our galaxy colours agree with the redshifted spectral energy distributions of locally measured galaxies, and compare our number counts with the deepest *UBVRIZ* counts in the literature. Finally we discuss in detail the algorithm we have developed to identify the stellar component of the survey and remove it from the final galaxy catalogues.

3.1   Comparison With CFRS Photometry

In this Section we test our photometric calibration using the CFRS photometric catalogue. As the CFRS photometry was not corrected for dust extinction, we have removed this correction from our photometry for the purpose of this comparison. Figure 3.1 shows the results for the three CFDF–PRS fields, with the blue and red horizontal lines drawn at $\Delta m = [0.0, -0.1]$ mag to guide the eye. The 03hr and 22hr fields have systematic offsets of $\lesssim 0.1$ mag, whereas the 14hr field matches almost exactly.

Perhaps the most striking feature of this Figure is how much smaller the scatter in the 22hr field is compared with the other fields. This is likely due to the heterogeneous nature of the CFRS survey, which was formed as a merger of two separate, smaller projects (one French and one Canadian). The CFRS fields were observed using different survey strategies (e.g. different mosaic patterns and exposure times) and were reduced using separate algorithms by different CFRS team members. Specifically, the
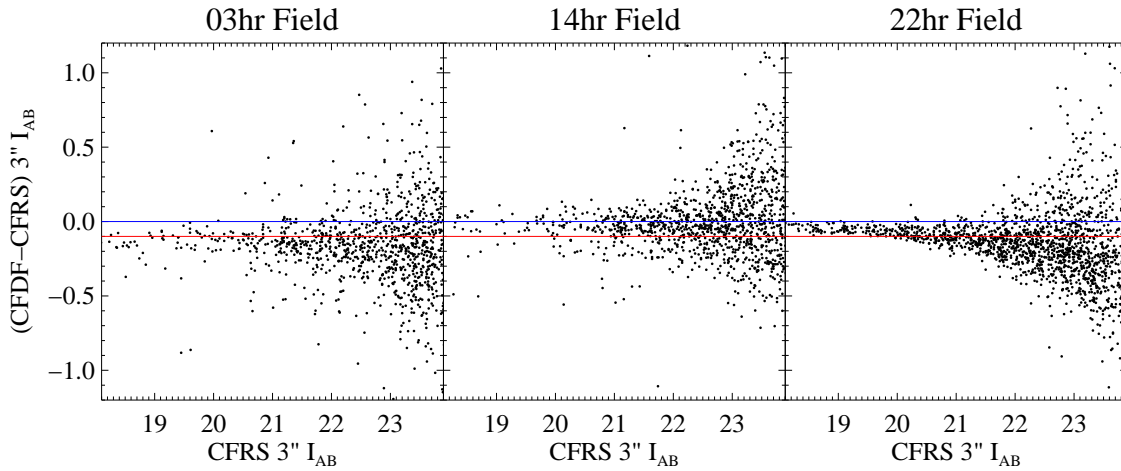
Figure 3.1 Comparison With CFRS Photometry. The blue and red lines denote the $\Delta m = [0.0, -0.1]$ levels, respectively. The calibrations in all three fields agree within $\lesssim 0.1$ mags, although the 14hr field agrees almost perfectly. The varying tightness of the agreement between fields is due to the heterogeneous nature of the CFRS imaging.

final 03hr data (originally a French field) had quite mediocre image quality, compared with the 14hr and 22hr fields. These Canadian fields were subjected to an exacting reduction algorithm, quite similar to that employed in the CFDF. The 14hr field, however, only had 45 minutes of imaging, compared with 60 minutes in the 22hr field.

With this background in mind, the field to field differences apparent in Figure 3.1 are not particularly surprising. In fact, the 03hr and 22hr CFDF–PRS I–band imaging, with superior CFH12k imaging and identical reduction procedures described in the previous Chapter, demonstrate the differences inherent in the original CFRS imaging. Note that these differences are almost entirely statistical in nature, with the systematic offsets being limited to $\lesssim 0.1$ mag.

We have rechecked and confirmed the accuracy of the photometric calibrations in these fields. One important difference between these two fields and the 14hr field is the amount of dust extinction present. Whereas in the 14hr field the dust correction is negligible, in the 03hr and 22hr fields, it is substantial, with Schlegel et al. (1998) $E(B-V)$ values of ~ 0.1 and 0.06, leading to I–band extinctions of ~ 0.2 and ~ 0.1 mag. To reiterate, the comparison in Figure 3.1 is made *without applying* these dust corrections (i.e. the surveys would appear *more* discrepant otherwise), since no dust corrections were applied in the CFRS. So while the application of these dust corrections is therefore not the cause of the discrepancy, we note that the difference in the absolute calibration is below the *value* of the dust correction we employ, which is uncertain in its own right (32% 2–σ random plus 10% systematic errors (for details, see Schlegel et al. 1998)). Considering all other possible systematic errors (i.e. different cameras, filters, reduction algorithms, etc.), we are quite satisfied to agree within this astrophysical uncertainty. It should also be

noted that in Section §4.2 we will be further adjusting our photometric zeropoints using a novel form of calibration refinement that takes advantage of the large spectroscopic redshift sample in our fields. These adjustments are all small however ($\lesssim$ 0.1 mag) and do not substantially change the result of Figure 3.1.

3.2 Colour–Colour Plots

A comparison of the colours of our objects with those derived from empirically measured galaxy templates is a good test of the overall scientific integrity of the survey. Additionally, a good match is important since our first scientific goal is to calculate photometric redshifts using a template–fitting algorithm. In Figure 3.2 we plot the $(B-R)_{\mathrm{AB}}$ vs. $(R-I)_{\mathrm{AB}}$ colour-colour diagram for the $18.5 \leq I_{\mathrm{AB}} \leq 24$ objects in the CFDF–PRS 14hr field. We have overplotted the redshift tracks of the non–evolving Coleman et al. (1980) empirical galaxy templates in steps of $\Delta z = 0.25$. The data are well represented by the full colour span of this template set, although some interpolation between the individual templates set will likely be needed. We will make extensive use of colour–colour plots such as this in §3.4 to aid with star/galaxy separation.

3.3 Number Counts

Another excellent way to verify the scientific integrity of deep imaging data is to compare the measured number counts with external surveys of similar or greater depth. Measurements of the I–band and B–band number counts were made in the first paper we published based on the original CFDF UH8k imaging data (McCracken et al. 2001). In this Section we recompute the number counts from the final catalogues, produced from the full UH8k+CFH12k reduction and calibration algorithm described in detail in Chapter 2, in order to demonstrate the robustness of the reduction and the impressive depth of the data.

As we have chosen the I–band as our selection band, we study these number counts in detail in Figure 3.3, where we plot the results for each CFDF–PRS field individually and for the full survey. In the I–band we are fortunate to have a survey of large areal coverage, the wider but shallower Postman et al. (1998) survey, to compare with. At the faint end, we plot the average number counts from the Hubble Deep Fields (HDF) North and South, as measured by Metcalfe et al. (2001). The error bars, calculated as simple Poisson statistics, are smaller than the symbol size for both the CFDF–PRS and the Postman et al. (1998) survey.
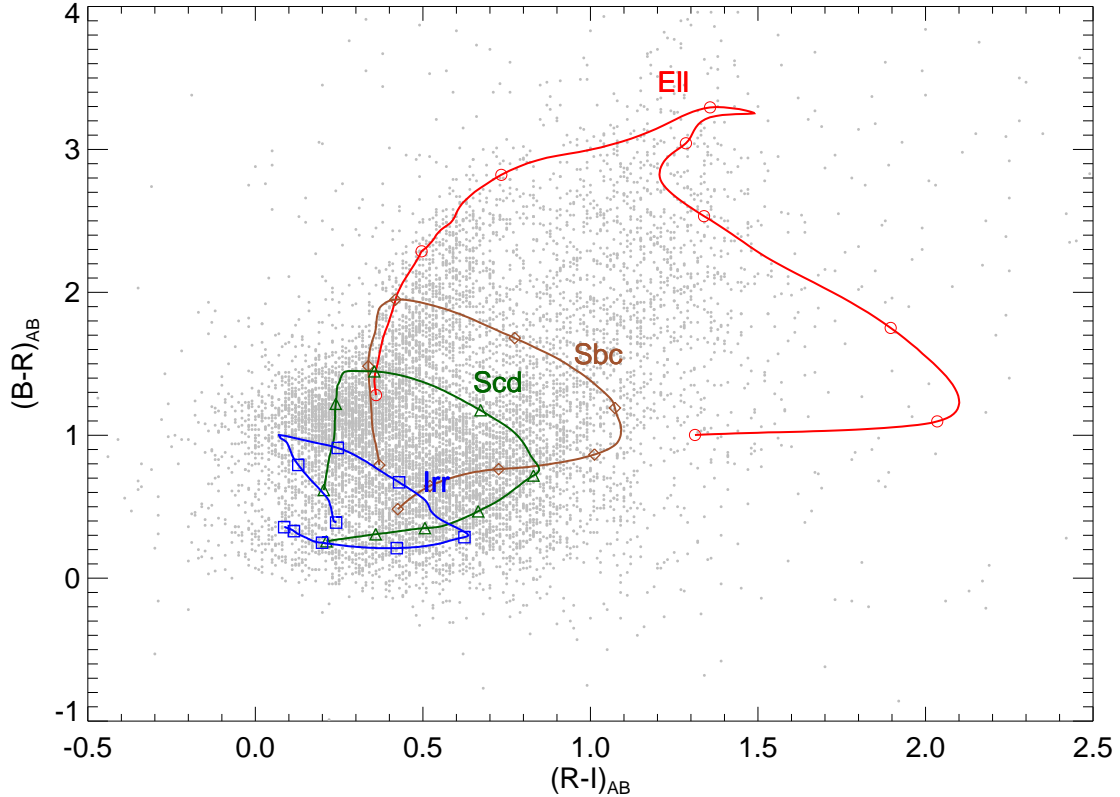
Figure 3.2 $(B - R)_{AB}$ vs. $(R - I)_{AB}$ plot for $18.5 \leq I_{AB} \leq 24$ objects in the CFDF–PRS 14hr field, with the redshift tracks of non–evolving Coleman et al. (1980) SEDs overplotted. The tracks begin on the left side of the plot and the open symbols denote $\Delta z = 0.25$ redshift intervals.

The Figure demonstrates the excellent agreement between our I–band number counts and the Postman et al. (1998) results, in each field and for the combined survey, over the range $20 \lesssim I_{AB} \lesssim 24$. At very bright magnitudes $I_{AB} \lesssim 20$ we clearly have a contribution from stars, in particular in the 22hr field. We will address the identification and removal of the stellar component in the next Section. At the faint end, we agree very well with the HDF points to $I_{AB} \sim 25$, although the HDF number counts appear to have a slightly higher normalization than both our data and that of Postman et al. (1998). Considering that the sum of the two HDF fields cover just 0.006 times our area, and that each HDF field is smaller than the correlation length of galaxies at $z \sim 1$, it is very likely the HDF number counts suffer from a large uncertainty due to cosmic variance. Nevertheless, the slope of the HDF number counts agrees very well with our own.

As will be explained in Chapter 5, we limit our analysis in the CFDF–PRS to the $I_{AB} \leq 24$ regime. We can see in the Figure how at this limiting magnitude, denoted by the dashed line, we are quite far from the magnitude at which our counts begin to turn over. In fact, from completeness simulations we conducted based on data inferior to the present survey in both depth and cosmetic quality (McCracken
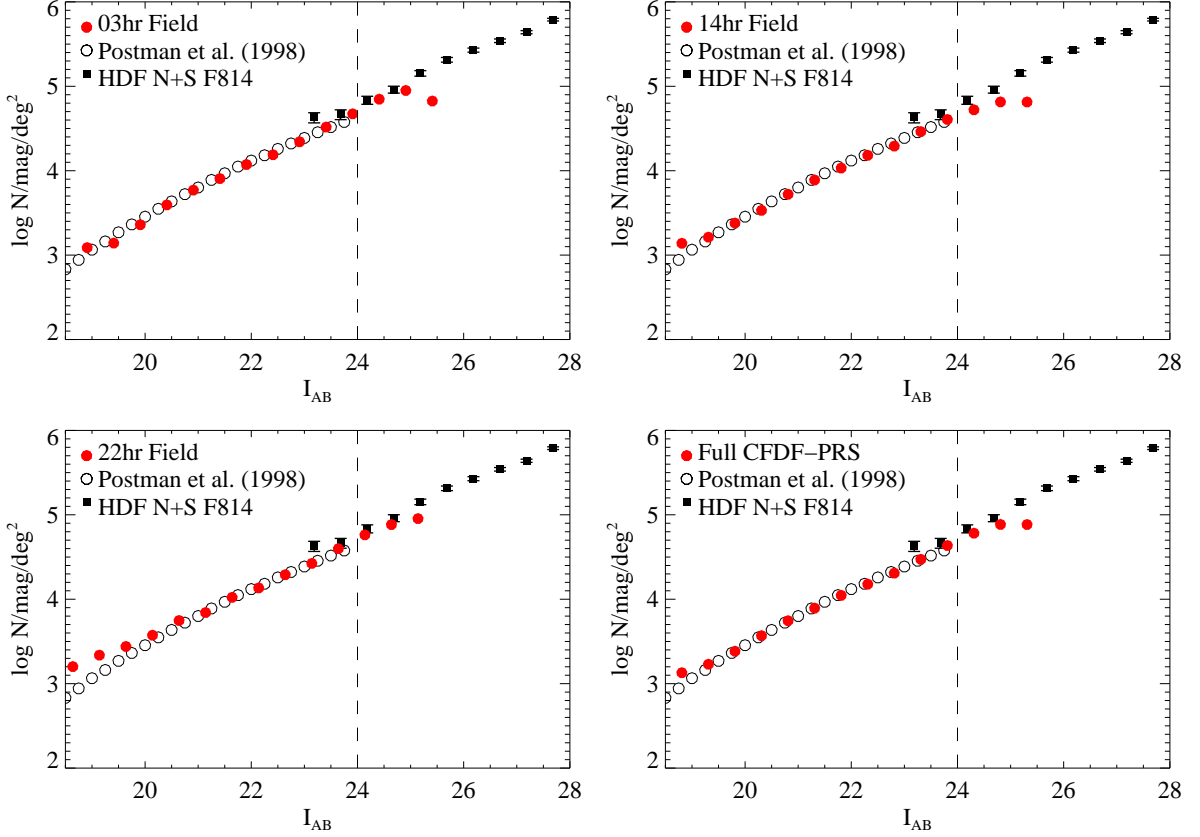
Figure   3.3 Raw I_{AB} number counts in the CFDF–PRS (filled circles). The open circles are from Postman et al. (1998) and the filled squares are the average of the Hubble Deep Field North and South number counts. Errors in the latter are Poissonian. The dashed line in each panel illustrates that the $I_{AB} \le 24$ limit we will adopt in Chapter 5 is considerably brighter than the magnitude at which our counts begin to turn over.

et al. 2001), we expect to be at least $\sim 90\%$ complete to $I_{AB} \sim 24$, with the formal 50% completeness limit occurring at $I_{AB} \sim 25.5$.

We have also computed number counts in the *UBVR* bands for the full CFDF–PRS survey, and these are presented in Figure 3.4. The number counts in all 4 bands agree well with previous results from the literature, including the overall amplitude, the slope and even the curvature. No attempt was made to convert the counts from these disparate surveys to a common magnitude system, other than to apply approximate corrections to bring them to the AB system we are using. We have used the original errors for those surveys that reported them, and have adopted Poisson errors otherwise. We point out that our fields are considerably larger, by factors ranging from 20 to 400, than all the deep surveys we compare with.

In the *U*–band we once again compare our survey to the HDF data, along with the WHT Deep Field (Metcalfe et al. 2001) and the Hogg et al. (1997) surveys. The AB correction is largest and most
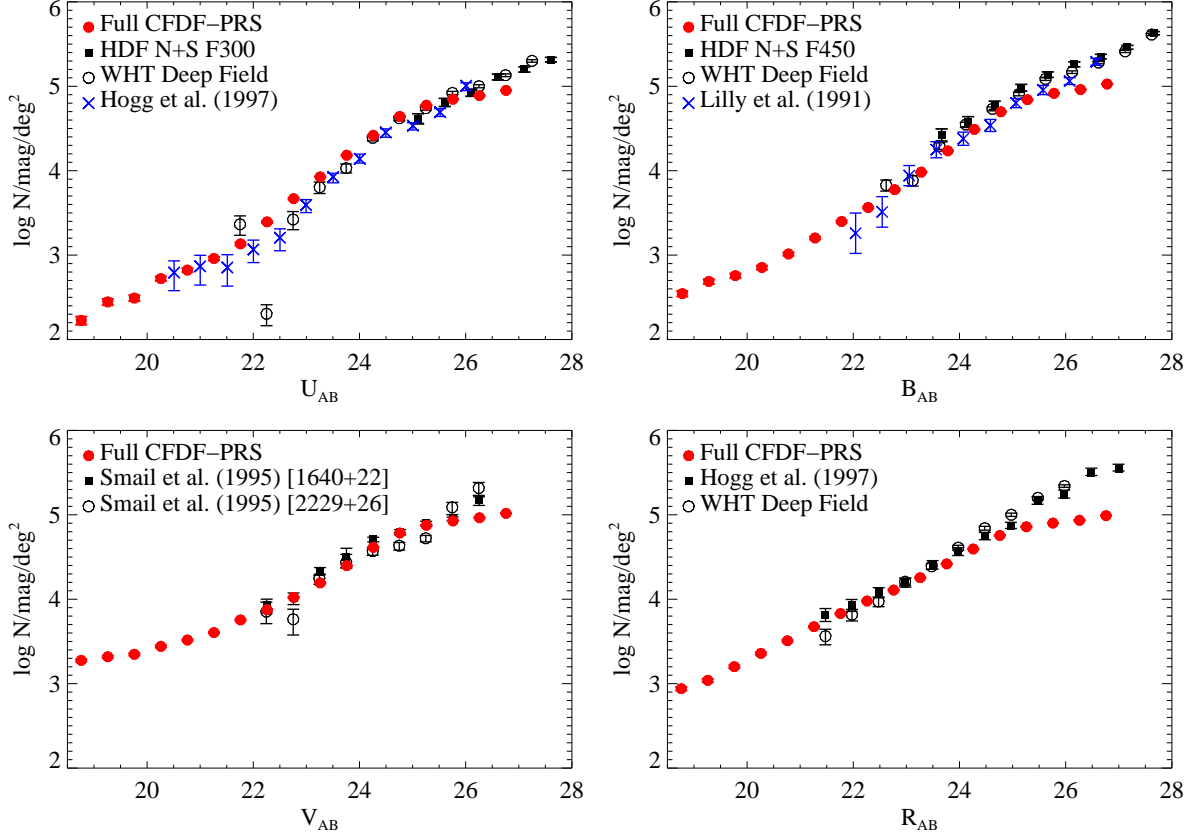
Figure 3.4 $(UBVR)_{AB}$ Number Counts in the CFDF–PRS compared with a selection of deep counts from the literature.

uncertain for the U–data, especially for the extremely blue HST F300 filter. Nevertheless, our results agree quite well with these other surveys to $U_{AB} \sim 26$.

The B–band counts agree very well with the Lilly et al. (1991), WHT Deep Field and HDF deep number counts to $B_{AB} \sim 25.5$. In the V–band we compare with the Smail et al. (1995) measurements in two separate fields, with our counts approximately the average of the two to $V_{AB} \sim 25.7$. The R–band CFDF–PRS counts agree very well with the Hogg et al. (1997) and WHT Deep Field counts to $R_{AB} \sim 25$.

As with the I–band, the $UBVR$ number counts in the literature are well reproduced in our data, which represents a significant improvement over previous studies in terms of the field size for a survey of this depth. Owing to the novelty (and difficulty) of the working in the Z–band, we could not find any comparison studies for our Z–band number counts other than the Sloan Digital Sky Survey (SDSS), which overlaps with our sample only for $Z_{AB} < 20$, where we are most affected by the presence of stars in our raw number counts. We therefore defer a comparison with the SDSS until the next Section where we describe and implement our star/galaxy classification.

3.4 Star/Galaxy Separation

Accurate studies of the galaxy population from multi–colour imaging surveys require extremely clean galaxy samples, devoid of stars, cosmic rays, and CCD artifacts. Our reduction procedure, described in Chapter 2, removes all transient phenomena (e.g. cosmic rays, satellite trails, asteroids), whereas the detailed masking of the final images excludes regions of scattered light and the charge bleeding due to saturated stars. The only remaining non–extragalactic sources are regular unsaturated stars themselves. This Section describes the procedure we have adopted to rid the CFDF–PRS galaxy catalogue of this stellar contamination.

As this is a photometric redshift survey, in which galaxy redshifts are assigned via comparison of observed object spectral energy distributions (SEDs) against redshifted galaxy template SEDS (to be described in detail in Section §4.1), it is logical to hypothesize that including model stellar templates in the fitting algorithm will properly identify the stars. Several groups (e. g. Chen et al. 2002, Firth et al. 2002) have tried to implement this idea with mixed results. While most stars are properly classified as such, a large fraction of galaxies are misclassified as stars. The reason is likely that the model stellar templates are not sufficiently accurate and detailed to produce a worse fit to observed galaxy SEDs than actual galaxy templates, at least when both are convolved through broadband ($\sim 20\%$) filters. In particular, neither empirical nor model spectra are particularly accurate for the reddest and coolest (L and T) dwarf stars.

For most analyses it is preferable to retain some stars rather than incorrectly reject real galaxies. As such, imaging surveys typically employ a simple morphological star/galaxy separation, which is only reliable at high signal–to–noise and at magnitudes bright enough so that galaxies are resolved. This limit is typically between $21 \leq I_{\mathrm{AB}} \leq 22$ for ground–based imaging.

We have instead devised an empirical, hybrid technique that incorporates both morphological and 4 color–color planes of information into a star/galaxy separation algorithm. We have tested the method and shown it to be reliable down to at least $I_{\mathrm{AB}} \sim 24$. The algorithm is essentially a weighted voting scheme. The probabilities associated with each object's position in a concentration parameter–magnitude plane and 4 color–color planes are taken together to produce the overall likelihood of the object being a star.

3.4.1 Morphological Component

After substantial testing, we have adopted a concentration parameter of the difference of $(0.75'' - 3'')$ aperture magnitudes in our Z–band image in which the seeing varies from $0.5'' - 0.7''$ in the three CFDF–
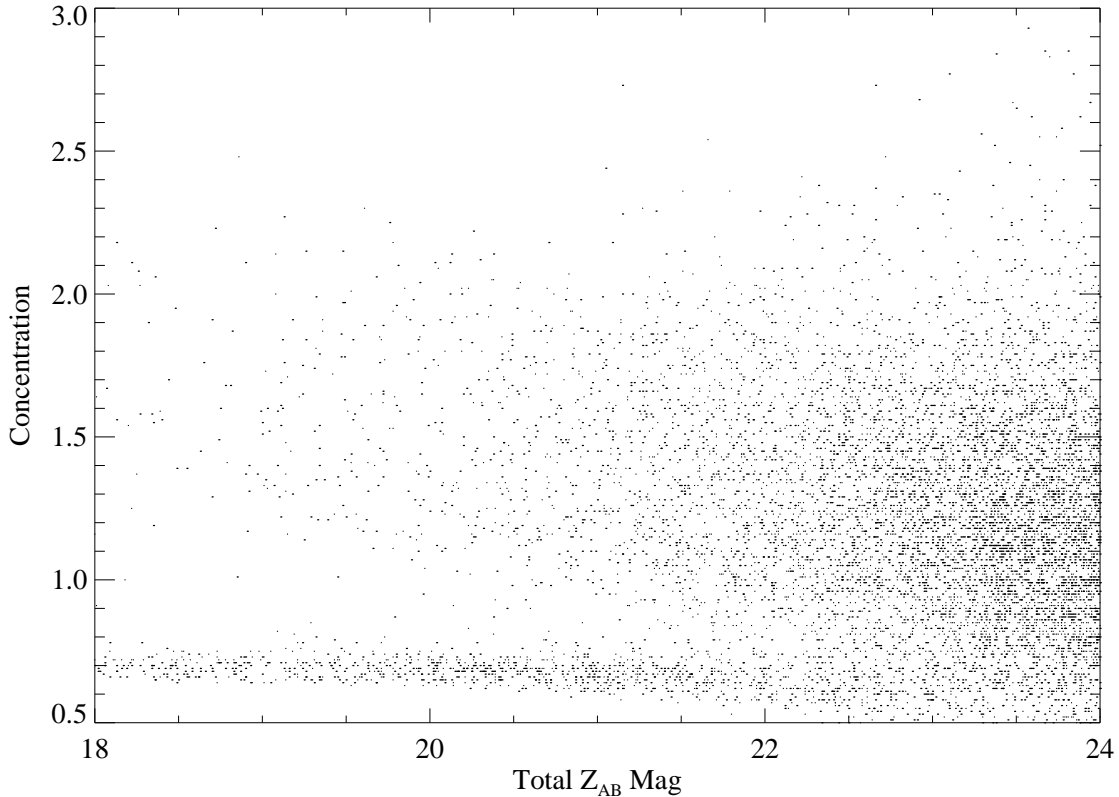
Figure 3.5 This plot of the concentration parameter $((0.75'' - 3''))$ aperture magnitude difference) vs. total Z_{AB} magnitude in the CFDF–PRS 22hr field shows the clean separation of stars and galaxies at relatively bright $Z_{\mathrm{AB}} \lesssim 21.5$ magnitudes.

PRS fields. More concentrated objects have smaller concentration parameters. As shown in Figure 3.5, this concentration parameter cleanly separates stars and galaxies at $Z_{\mathrm{AB}} \lesssim 21.5$. The stars appear as a thin, nearly horizontal line in this plane, representing the unresolved objects, whereas the fully resolved galaxies have much larger concentration parameters. At magnitudes fainter than about $Z_{\mathrm{AB}} \sim 22$, the ability to distinguish the smallest galaxies from the stars is essentially lost. Although the stars remain in the morphological stellar locus to the faintest magnitudes, increasing photometric errors, coupled with decreasing apparent galaxy sizes, conspire to contaminate this stellar locus with galaxies.

We extracted from plots like Figure 3.5 a sample of morphologically selected stars with magnitudes between $19.0 \leq Z_{\mathrm{AB}} \leq 21.0$ (hereafter referred to as $Z21$) in each CFDF–PRS field. In order to determine the extension of the morphological stellar locus to $Z_{\mathrm{AB}} > 21.0$, we twice scaled the Z–band images in each field, rendering them 2 and 4 magnitudes fainter, respectively. We then translated these scaled images by $\sim 10'$ and added them back to the original Z–band images, ensuring that the image noise properties were unaltered in the process. Details of this technique, which we will employ again in
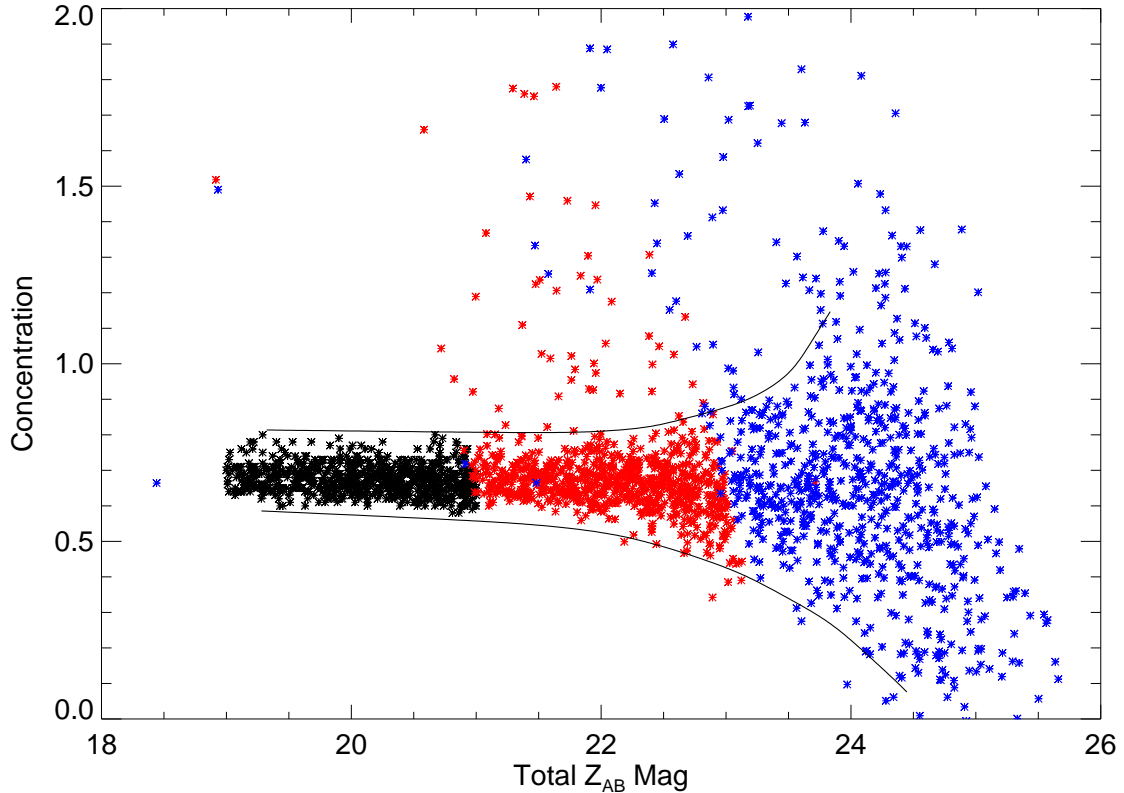
Figure 3.6 Concentration parameter vs. Z_{AB} magnitude for the morphologically selected $Z21$ stellar sample (black symbols), and progressively fainter $21 < Z_{AB} \leq 23$ (red symbols) and $23 < Z_{AB} \leq 25$ (blue symbols) reproductions of it. The black curves roughly illustrate the envelope of the widening stellar locus. The distant outliers are stars that by chance fell on top of another object during the translation part of the faintening technique described fully in Appendix B.

Section §4.3, are given in Appendix B. Figure 3.6 shows the result of this technique for the 22hr field, where the black symbols are the $Z21$ sample of Figure 3.5 and the red and blue symbols are the same morphological stars made 2 and 4 magnitudes fainter, respectively. The main effect of the decreasing signal to noise is a gradual broadening of the stellar locus, becoming quite pronounced at $Z_{AB} > 23.5$. The black curves are drawn to guide the eye to this general trend. The red and blue outliers are those stars which by chance fell on top of another object after the translation in the faintening process. They are therefore no longer true morphological point sources, and are not useful in assessing the effect of signal to noise on the morphological classification of stars. We will quantify in Section §3.4.3 how we use this morphological information to classify stars in the CFDF–PRS.

3.4.2   Colour Component

In addition to the standard morphological information, we also use the full multi–colour nature of the dataset to improve our stellar classification system. Figure 3.7 shows colour–colour plots for the 14hr field for the $Z21$ sample (black symbols) as well as its fainter extensions (once again red and blue symbols as in Figure 3.6) as a function of limiting magnitude. While the stellar loci diffuse out into each colour–colour plane with decreasing signal–to–noise, the degradation with depth is not as dramatic as with the morphological concentration parameter to $I_{AB} \sim 24$. Note that the stellar locus occupies a relatively narrow region of the colour–colour plane, whereas the general galaxy sample, defined here for simplicity as objects above the main stellar locus in plots like Figure 3.5, fills the plane much more broadly.

Figure 3.8 shows the four adjacent colour–colour plots we can form with our $UBVRIZ$ multi–colour imaging, using the $Z21$ sample in the 03hr field. It appears that the stellar loci of the bluer colour–colour plots (upper panels) are less well–defined and may therefore provide less discriminatory power compared to the redder ones (lower panels). This is simply an artifact of the red I_{AB} magnitude selection coupled with the essentially red spectral energy distribution of most stars. For example, at $I_{AB} \sim 24$ the majority of stars have $U_{AB} \gtrsim 26$ and hence the signal–to–noise is in fact quite a lot lower for the $(U - B)$ vs. $(B - V)$ plot. Although the two reddest (lower) plots in the Figure place much stricter limits on the range of colour space identified as stellar, we impose the requirement that potentially stellar objects fall on all four independent stellar loci, as well as being morphologically compact. Having described the morphological and colour properties of the $Z21$ calibration sample we now describe the quantitative implementation of our star/galaxy classification system.
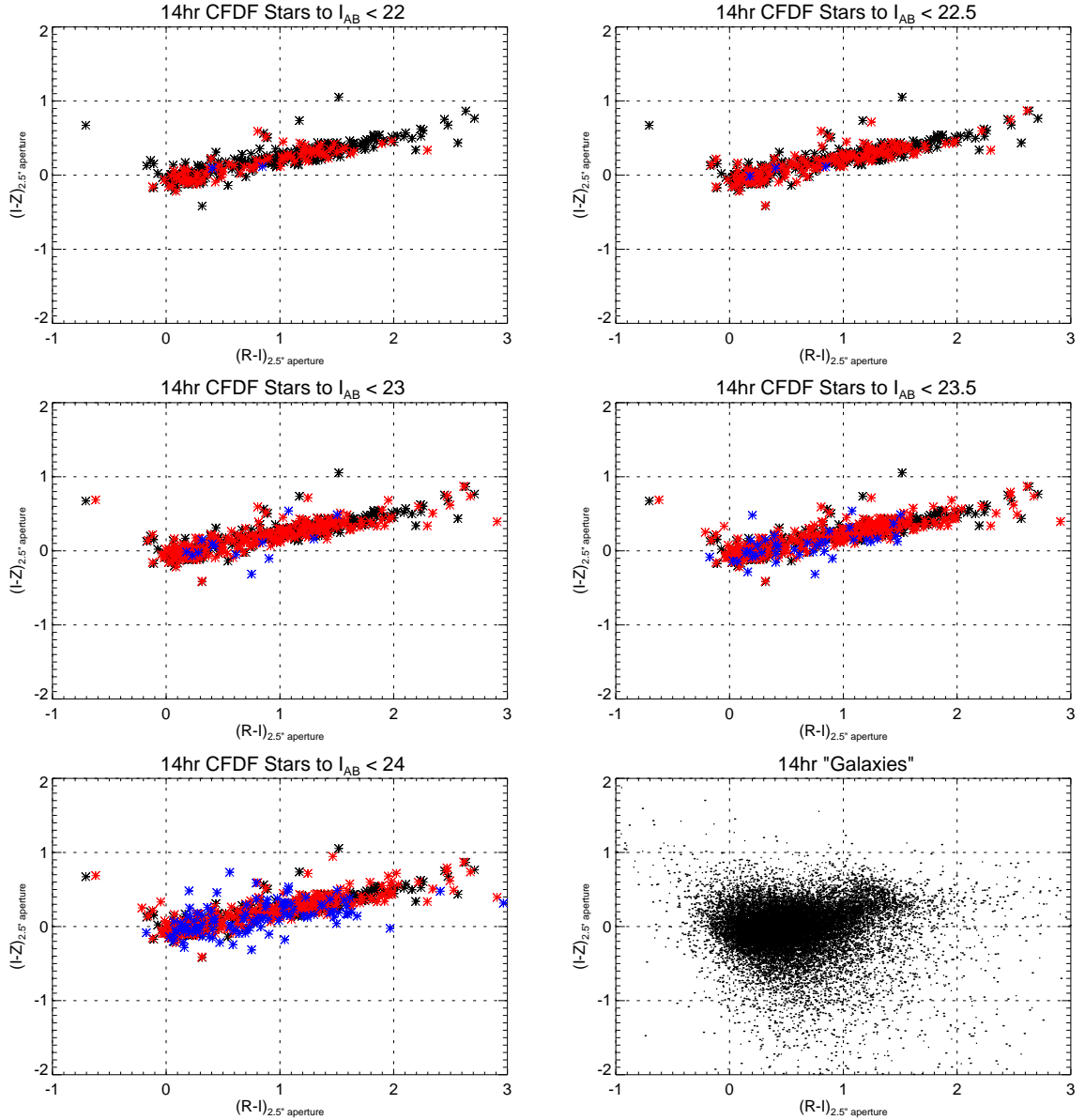
Figure 3.7 $(I - Z)$ vs. $(R - I)$ for the $Z21$ sample (black symbols) in the CFDF–PRS 14hr field as a function of limiting magnitude. The red and blue symbols are the same stars made 2 and 4 magnitudes fainter using the procedure detailed in Appendix B. Clearly the colours are is less affected by the decreasing signal–to–noise than the morphological concentration parameter. The stellar locus in these red filters remains quite narrow in this colour plane compared with the general galaxy population in the final panel (lower right).
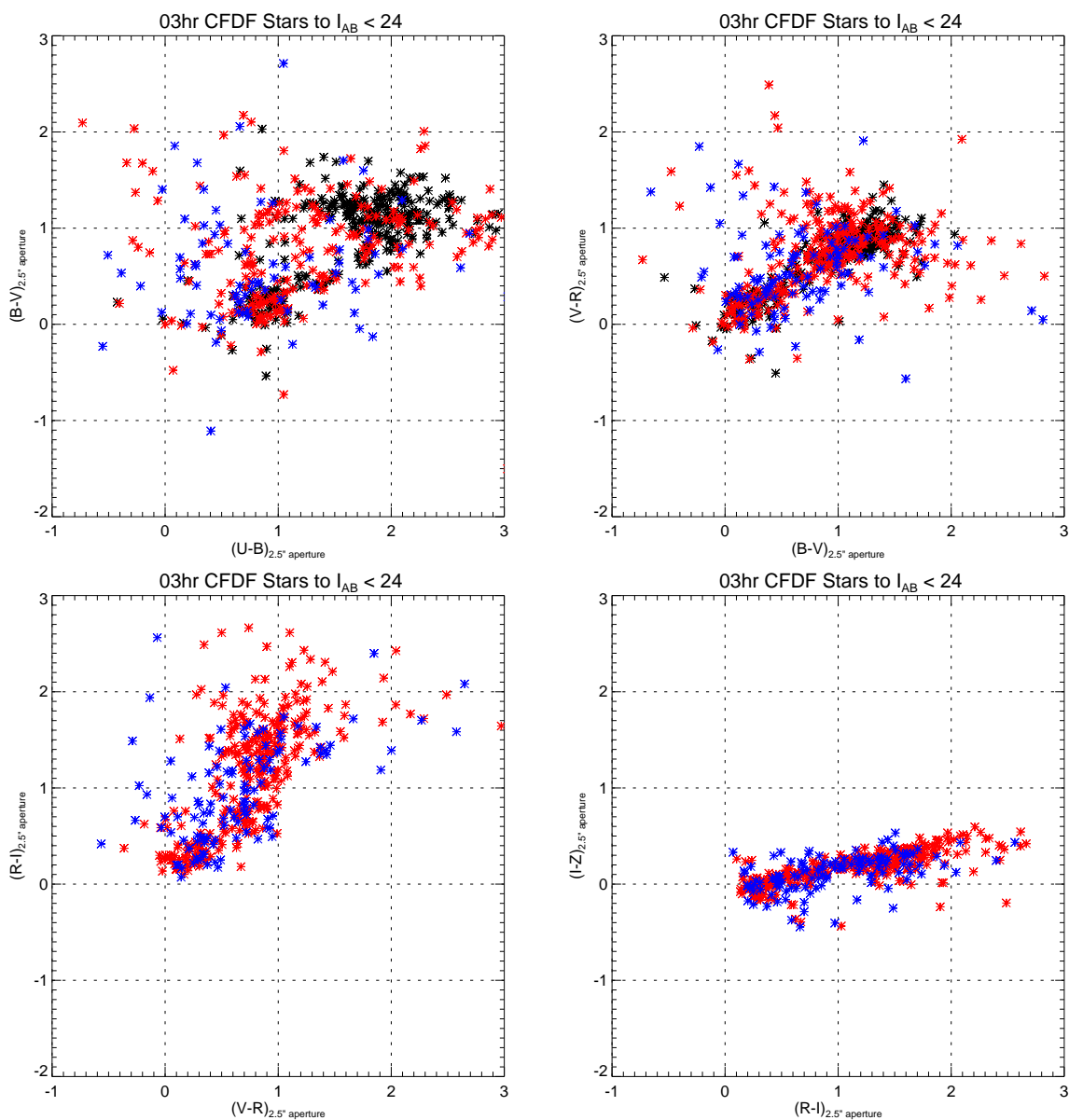
Figure 3.8 Colour–colour plots for the extended $Z21$ morphologically selected stars in the CFDF–PRS 03hr field. The bluer colour–colour plots (upper panels) have less sharply defined stellar loci than the redder ones (lower panels), in part due to lower S/N (see text), but the effect is not severe as shown in Figure 3.10.

3.4.3   Quantitative Voting Algorithm

While the stellar regions in the morphological and colour–colour planes are relatively well defined, there is no simple set of magnitude and colour cuts that clearly selects all stars without misclassifying some galaxies. The philosophy we adopted is that false negatives for stellarity were far more preferable than false positives, as we wish to prevent the systematic removal of any part of the galaxy distribution.

We instead devised a sort of voting scheme in which objects are assigned a stellarity probability composed of the product of the morphological and colour probabilities. To be more precise, we created smoothed, normalized, 2–dimensional histograms of each of our five independent measures of stellarity: the single morphological concentration parameter–magnitude plane and the 4 colour–colour planes. These are shown in Figures 3.9 and 3.10, respectively. The morphological surface is constructed inde-
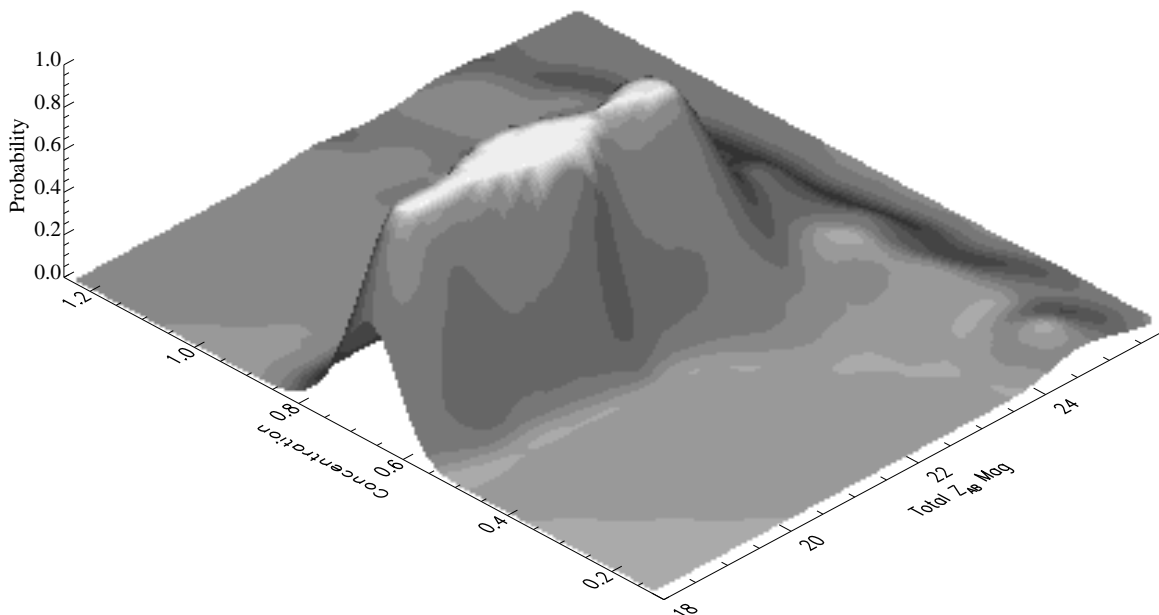
Figure   3.9 Two dimensional histogram of concentration parameter vs. Z_{AB} magnitude in the 22hr CFDF–PRS field, normalized to unit maximum. We interpret the surface value corresponding to each position in this plane as proportional to the *morphological probability* of being a star.

pendently for each field as it is strongly seeing dependent, and quite different from field to field. The shape of the surface, however is quite similar for all three fields, with the primary property that the morphological stellarity signal is quite strong at bright magnitudes, and falls off quickly beyond $Z_{AB} \sim 23$.

We normalize these surface to have a maximum value of unity, and associate the height above the concentration parameter–magnitude plane as proportional to the *morphological probability* of being a star. Each CFDF–PRS object is assigned such a morphological stellar probability.
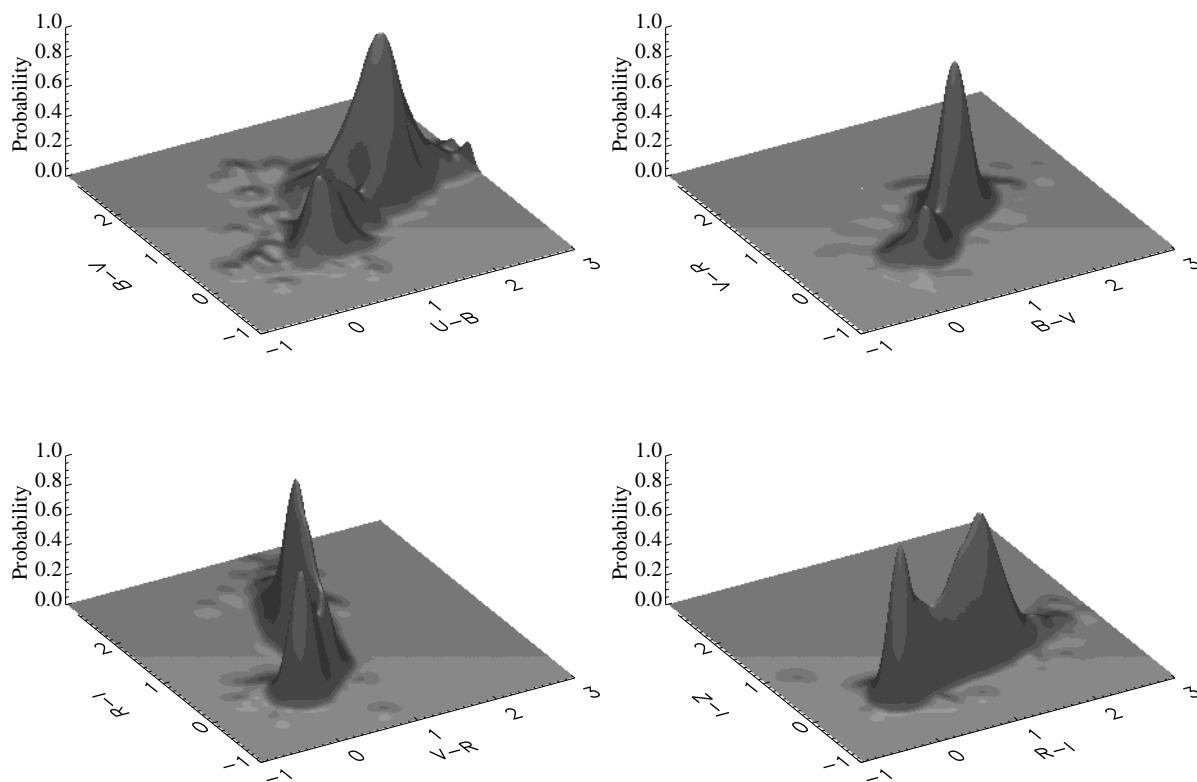
Figure 3.10 Two dimensional histograms of all four colour–colour plots of the extended $Z21$ sample in all three CFDF–PRS fields, normalized to unit maximum. We interpret the surface values corresponding to each position in these planes as proportional to the *colour probability* of being a star for each two colour combination.

Despite the less impressive appearance of the stellar loci in the upper panels of Figure 3.8, the 2–dimensional histograms of the colour–colour plots show that very few objects fall off the main stellar loci, even for the bluest colours. These colours are computed from images smoothed to have seeing profiles equivalent to the worst seeing image in each field. As such we combine the colour–colour plots from all three fields to reduce the noise in these final colour–colour surfaces. As with the morphological surface, we assign four *colour probabilities* to each CFDF–PRS object based on its location in each of the four colour–colour planes.

We would like to combine the 5 independent probabilities into a final likelihood for each object of being a star. At bright magnitudes the morphological information is more robust and should be more heavily weighted, whereas at the faint end the color information has much more discriminatory power.

We adopted the following weighting scheme that accounts for these properties. Defining P_M as the *morphological probability* and

$$P_C = P_\text{UBV} \times P_\text{BVR} \times P_\text{VRI} \times P_\text{RIZ} \qquad (3.1)$$

as the final *colour probability*, we define the overall stellar probability as

$$P_\star = P_M \times P_C^\beta \qquad (3.2)$$

where

$$\beta = \begin{pmatrix} 0.5 \\ 1.0 \\ 2.0 \\ 4.0 \end{pmatrix} \text{ for } \begin{pmatrix} Z_\text{AB} \leq 21.5 \\ 21.5 < Z_\text{AB} \leq 22.5 \\ 22.5 < Z_\text{AB} \leq 23.0 \\ Z_\text{AB} > 23.0 \end{pmatrix} \qquad (3.3)$$

At bright magnitudes the morphological probability has twice the weight of the final colour probability. When $\beta = 1$ there is equal weight between the two. Between $22.5 < Z_\text{AB} \leq 23.0$, the colour probability has double the weight of the morphological probability, and beyond $Z_\text{AB} > 23.0$ it has 4 times the weight.

3.4.4 External Constraint: Stellar Number Counts

With our final stellar probability in hand for each CFDF–PRS object, we can identify the objects most likely to be stars. However we still require knowledge of the number of stars present as a function of magnitude. This is because while our method ranks objects in terms of their relative likelihood of being stars, we don't know the value of the final probability that correctly divides the stars from the galaxy population as a function of magnitude.

In each field, the expected number counts of stars are taken from the Bahcall and Soneira (1980) models, which we found matched the observed counts of morphological stars at bright magnitudes in all 3 CFDF–PRS fields. In each magnitude bin dm, if the Bahcall and Soneira (1980) model predicts $N_\star(dm)$ stars, we label as stars the $N_\star(dm)$ objects with the highest stellar likelihood in our hybrid method. The philosophy of the method may be summarized as follows. Given that the $N_\star(dm)$ stars are present in each magnitude bin, the idea is to rank the objects in terms of likelihood of being stars and then to remove the $N_\star(dm)$ most likely objects. It is, of course, a statistical correction and is strictly appropriate only for statistical analyses of the galaxy population. However, it is significantly better than simply ignoring the stars below the morphological classification limit.

3.4.5   Tests of the Stellar Classification Algorithm

We conducted three tests to evaluate the reliability of the algorithm. The first test uses the angular correlation function to determine the clustering properties of the objects classified as stars. The second method compares the Z–band number counts with the much brighter SDSS survey. Finally, we conduct a direct assessment of the algorithm using the CFRS catalog of spectroscopically confirmed stars and galaxies.

Angular Correlations

We calculated the angular correlation function, $\omega(\theta)$, using the Landy and Szalay (1993) estimator

$$\omega(\theta) = \frac{DD - 2DR + RR}{RR} \tag{3.4}$$

for the objects classified as stellar by our hybrid method. As the first panel of Figure 3.11 illustrates, the angular correlation function of the objects classified as stars in the 22hr field is consistent with zero at all angular scales within Poisson errors. While necessary, this is not sufficient evidence to conclude the classifier is working properly. We see this by repeating the exercise with a randomly selected sample of objects classified as galaxies, taking a number *equal* to the number of stars in the field. This is shown in the upper right panel in the Figure. While the purpose was to illustrate the difference between the stellar and extragalactic samples, the result is instead indicative that there are too few objects in either of these samples to convincingly measure the angular correlation function.

We instead approached the problem from another perspective. In the lower left panel of Figure 3.11, we plot $\omega(\theta)$ for the full 22hr CFDF–PRS sample between $18.5 \leq I_{\mathrm{AB}} \leq 24$. For simplicity we adopt a power–law parametrization of the angular correlation function, $\omega(\theta) = A_\omega \theta^{-0.8}$, and neglect the correction for the integral constraint by limiting our fitting range to $\theta \leq 150''$. A more rigorous, in–depth correlation analysis is presented in Chapter 7.

In the final panel we plot $\omega(\theta)$ for the full galaxy sample, with the objects classified as stars removed. If a randomly distributed stellar sample is in fact the difference between these two samples, then we expect the correlation amplitude of the remaining galaxies to be increased by $1/(1 - f)^2$, where f is the stellar fraction of objects (e.g. Firth et al. 2002). The dashed line is a reproduction of the fiducial fit in the lower left panel, and the solid line is the predicted correlation function based on this relation. The latter produces a reasonably good fit to the measured galaxy correlation function. The expected increase in the clustering amplitude is readily apparent, and is highlighted by the difference between the samples in the sizes of the error bars on the log–log plot. In such plots the errors appear increasingly exaggerated for smaller values of ω. We have verified that removing an identical number of randomly
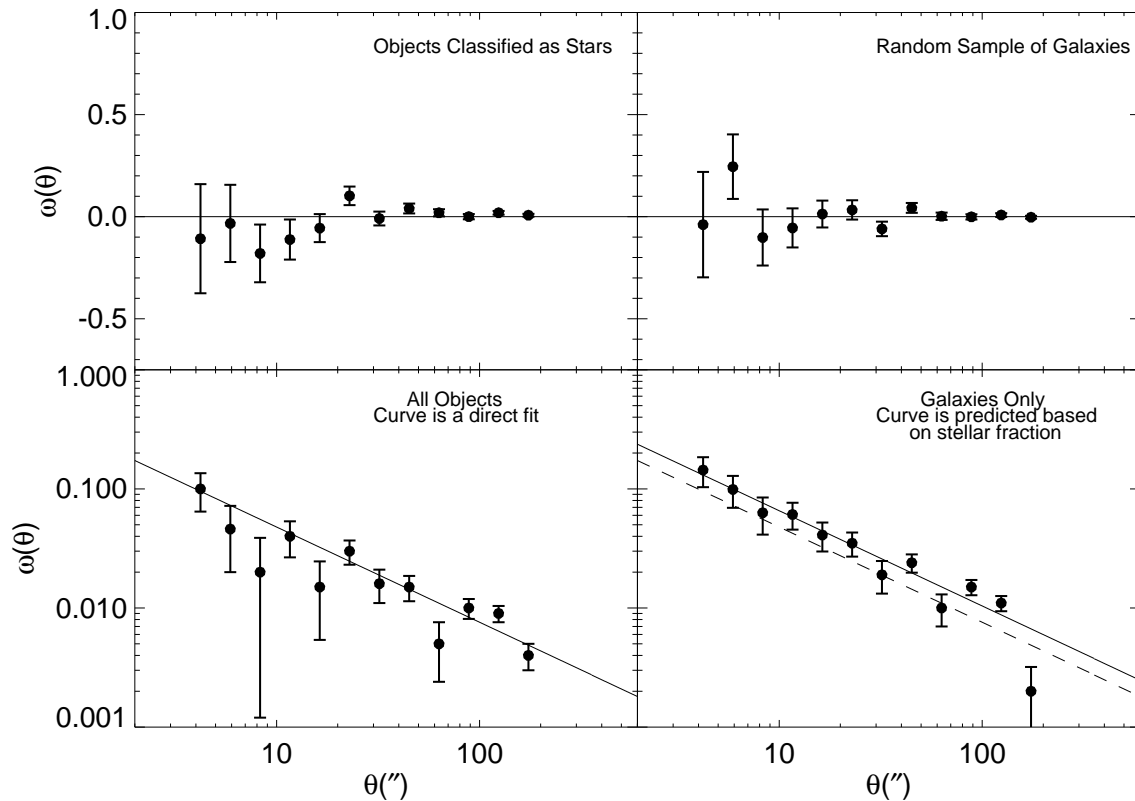
Figure 3.11 Demonstration of unclustered nature of stellar sample. Although the upper left plot shows the stellar component is consistent with no clustering, the number of objects is too small for a definitive measurement, as shown at upper right where $\omega(\theta)$ is computed for an identical number of randomly selected galaxies. Alternatively, the increase in clustering amplitude seen between the full sample (lower left) and star–removed galaxy sample (lower right) convincingly demonstrates the random nature of the stellar sample.

selected galaxies instead *lowers* the correlation function, as it should since the stellar fraction of the remaining sample is increased in this case. Hence we conclude that in fact our star/galaxy classifier has correctly removed a randomly distributed sample of stars from the full catalog.

Z–band Number Counts: Comparison with the SDSS

As discussed in the Section §3.3, a meaningful comparison of our Z–band number counts with the z' counts of the SDSS requires the removal of the stellar component because of the extreme brightness of the SDSS sample. We now present such a comparison in Figure 3.12. The panel on the left shows the raw number counts for the CFDF against the SDSS sample in which stars have been removed (for details see Yasuda et al. 2001). Clearly we have a non-negligible stellar component in our bright counts, mostly from the 22hr field. The panel on the right shows the CFDF–PRS Z_{AB} number counts for the galaxies only. Given the bluer SDSS z' filter, the agreement is excellent on $18.5 \le Z_{AB} \le 20$, beyond which the
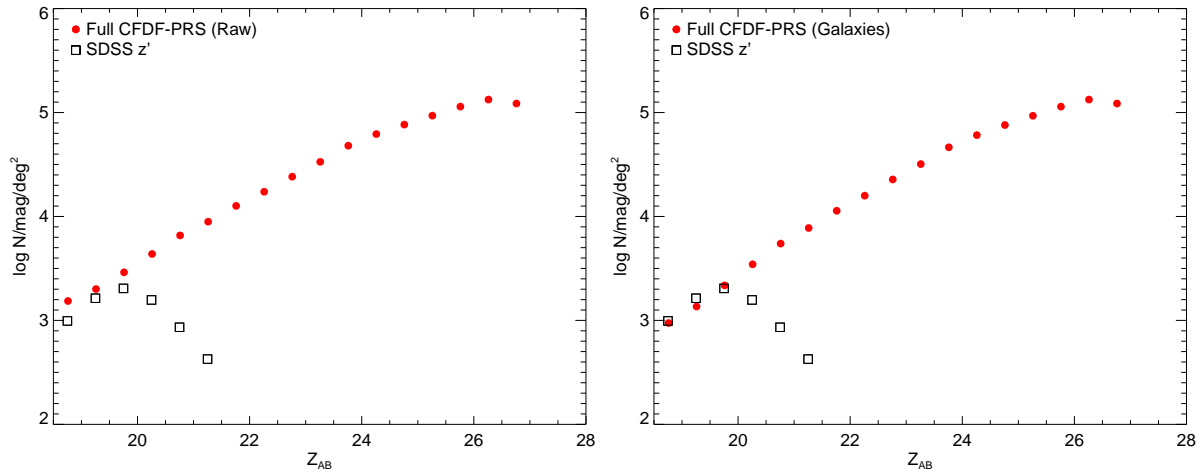
Figure 3.12 Z_{AB} number counts compared with the SDSS z'_{AB} counts. *Left panel:* Raw CFDF–PRS and SDSS counts; *Right panel:* CFDF–PRS counts for galaxies only, after removal of objects classified as stars, along with the SDSS counts.

SDSS becomes rapidly incomplete.

Direct Test: CFRS Spectroscopic Sample

Since we did not use the CFRS spectroscopic sample in any way in defining our classification algorithm, it is now available as an independent test of the algorithm. The CFRS spectroscopic sample in these fields contains 321 galaxies and 118 stars with $18.5 \leq I_{AB} \leq 22.5$, and allows us to explicitly test if our method, designed to rarely if ever misclassify galaxies, is performing reliably. We find that only 4 of the CFRS galaxies were misclassified as stars for an error rate of 1.2%, whereas 48 or 41% of the stars were misclassified as galaxies, or more precisely, were not subjected to classification at all. The disparity in these error rates indicates that we could perhaps have increased the fraction of objects subjected to classification in each magnitude bin. However as the CFRS is a relatively small sample and the two other tests described above are consistent with essentially perfect stellar classification, we prefer to remain conservative and leave the classified fraction as predicted by the Bahcall and Soneira (1980) model, noting that at worst we may only be removing 60% of the stars while retaining 99% of the galaxies.

Figure 3.4.5 shows the cumulative distribution function of objects as a function of the stellarity vote for the CFRS sample. Stars and galaxies are clearly strongly segregated, with less than 2% of galaxies receiving votes above 10^{-11} and over 60% of stars having votes above 0.001. An advantage of this method is that only a small percentage of objects at faint magnitudes — the expected stellar fraction — are subjected to classification. Therefore the fraction of misclassified galaxies is expected to remain constant or even drop down to the faintest magnitudes as the stellar to galaxy number counts ratio
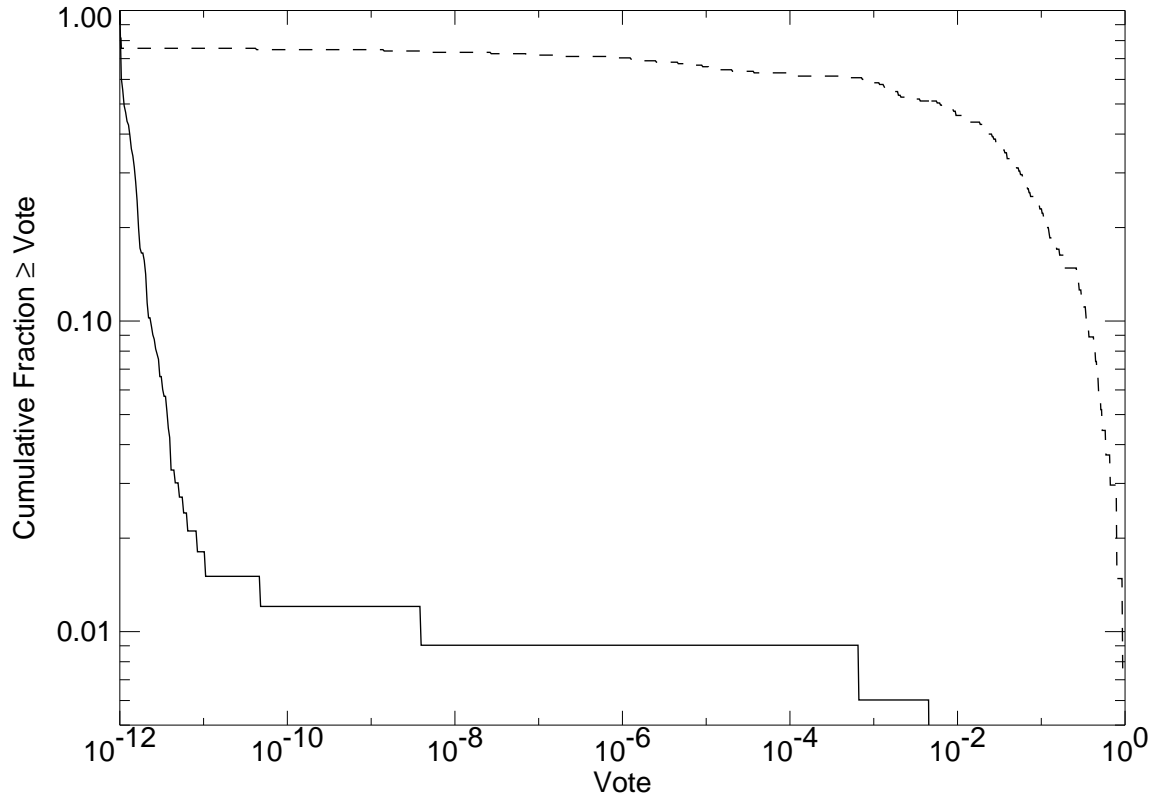
Figure 3.13 Cumulative distribution function of stellarity votes for CFRS stars (upper dashed curve) and galaxies (lower solid curve). Ideal stars and galaxies should have votes of unity and zero, respectively. The strong segregation of stars and galaxies is apparent, with less than 2% of galaxies receiving votes above 10^{-11} and over 60% of stars having votes above 0.001. The final classification depends on the votes of the objects in each magnitude bin. It is therefore possible for galaxies with anomalously high votes to nevertheless not be misclassified as stars.

becomes negligible.

Chapter 4

Photometric Redshifts in the

CFDF–PRS[1]

4.1 The Algorithm

In order to estimate photometric redshifts and calculate the redshift probability distributions needed for accurate statistical measurements of the galaxy distribution, an empirical template fitting algorithm was implemented. With our images convolved to a common seeing in each field, we compared $2.5''$ diameter aperture *UBVRIZ* fluxes to a set of empirical templates SEDs. We adopted the Coleman et al. (1980) empirical SEDs, supplemented by the Kinney et al. (1996) SB2 and SB3 starburst SEDs as the basis templates in our algorithm. This combination of templates has been shown to span the range of galaxy properties in the HDF from $0 < z < 6$ (Benítez 2000, Fernández-Soto et al. 2002). Fifteen interpolates of these basis spectra were used to improve the redshift resolution. Galaxy reddening is naturally incorporated into our empirical templates, as they are each composite spectra from numerous galaxies with varying levels of extinction. Our SEDs are statistically corrected for intergalactic hydrogen absorption as a function of redshift following Madau (1995), taking into account both Lyman series line blanketing at wavelengths below $\lambda_{\mathrm{obs}} < 1216\,(1+z)$ Å and continuum photoelectic absorption below the Lyman limit, $\lambda_{\mathrm{obs}} < 912\,(1+z)$ Å.

A maximum likelihood method (ML) was used to produce the redshift likelihood surface for each

object, as a function of redshift z and spectral type T:

$$\mathscr{L}(z,T) \propto \exp\left[-\chi^2(z,T)/2\right] \tag{4.1}$$

where

$$\chi^2(z,T) = \sum_{i}^{N_f} \frac{[f_i - AF_i(z,T)]^2}{\sigma_i^2}. \tag{4.2}$$

Here A is a simple scaling factor chosen to minimize χ^2 for each template, $F_i(z,T)$ is the flux of the empirical galaxy template T through the i–th filter at redshift z, f_i and σ_i are the object's fluxes and 1–σ flux errors in the i–th filter and the sum runs over the N_f filters. The overall normalization of the likelihood surface is arbitrary. The likelihood surface is projected to a simple function of redshift by maximizing with respect to T at each redshift (i.e. using the ML of the best–fit template SED at each z).

It is preferable to project the likelihood functions in this way rather than marginalize over all templates since the correct relative template density is unknown. As an extreme example, suppose we use only the 4 standard Coleman et al. (1980) templates (i.e. E, Sbc, Scd, Im) and add 100 interpolates between Sbc and Scd. In measuring the redshift of an elliptical galaxy our likelihood surface will contain some probability at each of these interpolated templates, albeit at a far lower level than the maximum likelihood at the correct redshift for the elliptical template. It is evident that integrating over all the templates produces a redshift likelihood function strongly dependent on the sampling of the template space. It can even lead to catastrophic failures when the integral of this low level probability surpasses the maximum likelihood of the z–T surface.

This code was tested extensively with public HDF data and using the hundreds of CFRS spectroscopic redshifts in our fields. The latter sample allowed a novel form of calibration of the method to significantly improve the redshift accuracy (see below). In the HDF, the simple ML redshifts matched the excellent results in the literature (Fernández-Soto et al. 2002, Benítez 2000), with redshift dispersions of $\sigma_z \sim 0.08\,(1+z)$ over the full redshift range $0 < z < 6$ and only one "catastrophic error" (for details see Fernández-Soto et al. 2002).

4.2   Calibration Using CFRS Spectroscopic Redshifts

The accuracy of photometric redshift estimation can be improved using a spectroscopic training set (e.g. Csabai et al. 2003) . Yee (1998) pointed out the danger in applying such a modified algorithm on galaxy populations with different properties (e.g. apparent magnitude, color, redshift) than those of the

calibrators. The danger is minimized in the template fitting algorithms (as compared with simple fitting functions), but not eliminated as illustrated by the recent SDSS (Csabai et al. 2003) photometric redshift results. In that study, the template SEDs, modified to better match the colors of the spectroscopic training set, were considerably less accurate for the higher redshift CNOC2 galaxies.

Despite the fact that the CFRS galaxies do in fact span nearly the full redshift range of interest for our filter set ($z \lesssim 1.3$), we have opted not to modify the template SEDs to better match the CFRS spectroscopic redshifts. The much deeper CFDF–PRS samples galaxies 10 times fainter without loss of sensitivity to objects with weak or absent emission lines. The selection functions between the calibrators and the main sample are therefore quite different.

We have instead improved the photometric calibration using the spectroscopic sample as a novel kind of calibrator. Using only CFRS galaxies with the most secure spectroscopic redshifts (confidence class 3 and 4), we have a training set of 321 galaxies between $0 \leq z \leq 1$ and $18.5 \leq I_{AB} \leq 22.5$ (where the bright limit is imposed by the saturation limit of the CFDF–PRS).

We examined the magnitude residuals of the best–fitting template at the correct (spectroscopic) redshift, as a function of the color of the galaxy. As an example, if all galaxies, regardless of redshift or spectral type, showed a residual, Δm, in some band, that would suggest that there was a zero point offset of Δm in that filter. If Δm was correlated with the color of the objects, that would indicate an error in the effective wavelength (the origin of which is inaccurate filter transmission or QE curves). In practice such color terms were negligible as expected, whereas small but significant zeropoint offsets were found in several filters. These offsets are caused, in part, by band–to–band seeing variations not fully removed when we convolve our images in each filter to the same seeing. Such residual seeing variations would manifest as zeropoint offsets. Almost all calculated offsets were less than 0.1 mag, the largest being 0.12 mag. An example is shown in Figure 4.1 for the R filter in the 03hr field.

This optimal calibration produces photometric redshifts with very similar error properties in all three CFDF–PRS fields, as shown in Figure 4.2. The redshift dispersion, in the common measure in which the error increases as $(1+z)$ is $\sigma_z/(1+z) = 0.042$ for galaxies within the clipped 3σ limits of the distribution (includes over 92% of the galaxies). The direct dispersion for this sample is $\sigma_z = 0.062$. Deferring a detailed discussion of the statistical properties of the photometric redshift method to Sections §4.4–§4.7, we define a catastrophic failure in the present context as occurring when $|z_{ph} - z_{sp}| \geq 1.0$. In this measure, the catastrophic fraction is 3.7% for the CFRS sample, or roughly half of the galaxies rejected from the above dispersion estimate.

It is important to stress that no bias was introduced to the CFDF–PRS through the use of the CFRS spectroscopy. The true redshifts were used to transform the CFRS galaxies present in the CFDF–PRS
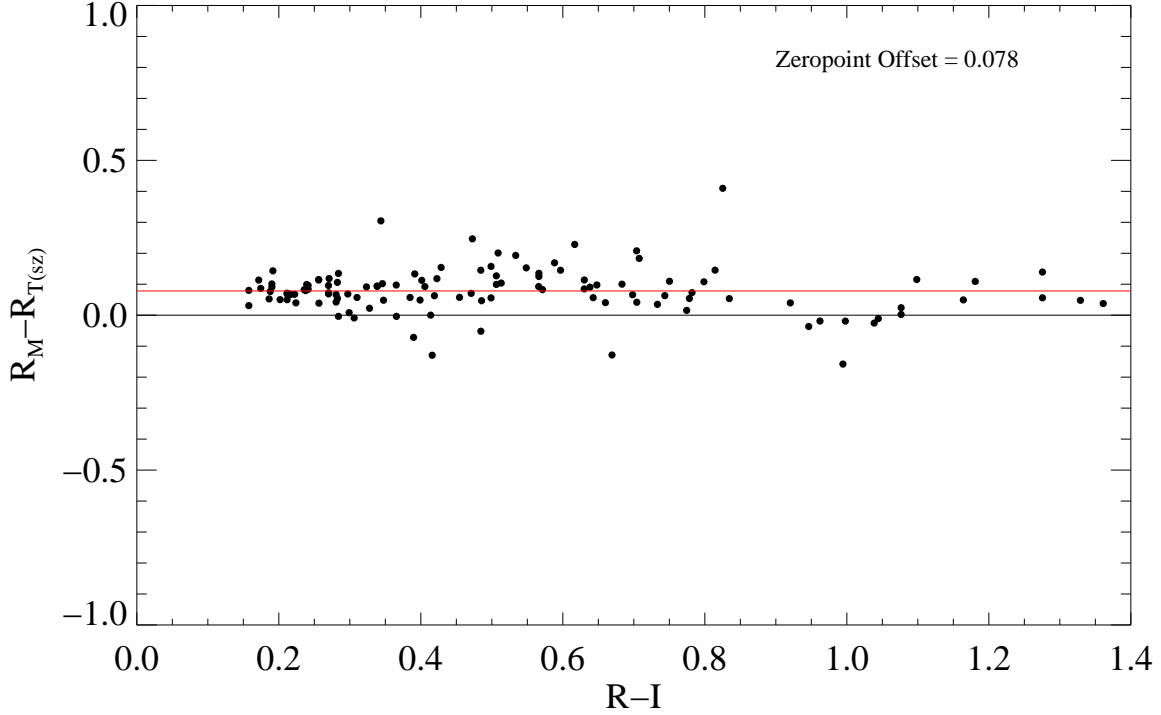
Figure 4.1 Residuals between the measured R magnitudes and the best–fitting template SEDs redshifted to the spectroscopic redshifts versus galaxy color. This technique essentially identifies the optimal photometric zero point and the effective wavelength in each broadband filter, using the CFRS galaxies as photometric standards. In this 03hr R band plot, the zeropoint offset is ~ 0.08 magnitudes.

into photometric standards, which were in turn used to tweak our zeropoints. Given the spectroscopic redshifts, the process is completely internal to the CFDF–PRS photometry, and results in optimal photometric redshifts for our depth and wavelength coverage.

4.3 Photometric Redshift Accuracy for $I_{AB} > 22.5$ Galaxies

In order to test the accuracy of photometric redshifts at magnitudes fainter than the CFRS data, we added a scaled version of each image in each field back to itself, with a positional offset larger than the full CFRS field. Care was taken to ensure that the noise properties of the resulting images were identical to those of the original images. Specifically, in each field and filter we multiplied the original image by a scale factor, f_1, translated this scaled image by $\sim 10'$, and added it back to the original image. We then divided this new image by $(1 + f_1^2)^{0.5}$ to restore the original image's noise properties. The scale factor, f_1, is chosen such that in the final image CFRS galaxies with $I_{AB} = 22.5$ are transformed into $I_{AB} = 24$
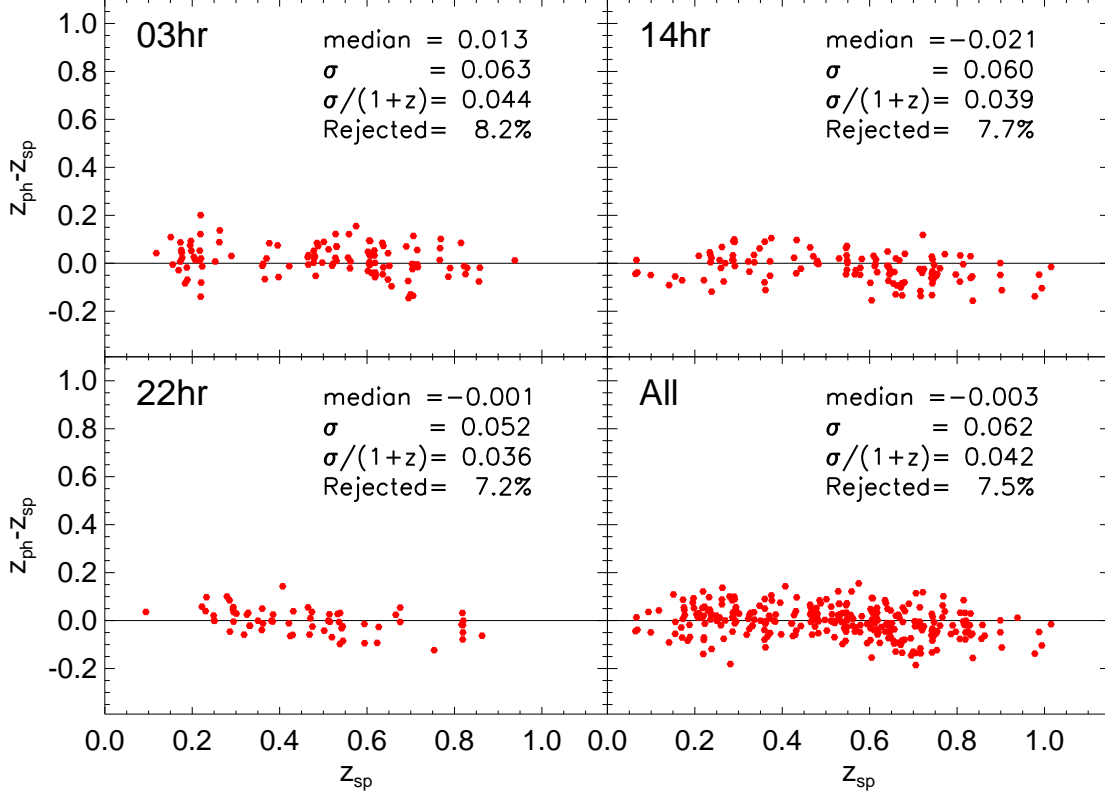
Figure 4.2 Residuals in photometric vs. spectroscopic redshift for the $\sim 92\%$ of $I_{AB} \leq 22.5$ CFRS galaxies that fall within the clipped 3σ limits of the distribution. The actual redshift dispersion for this sample is $\sigma \sim 0.06$. In the commonly used $\sigma/(1+z)$ measure the dispersion drops to ~ 0.04.

objects (i.e. a 1.5 magnitude change $\rightarrow f_1 \approx 0.2595$). See Appendix B for full details.

These fainter CFRS galaxies were photometered, and photometric redshifts were computed as above. The results, shown in Figure 4.3, demonstrate that while the increasing photometric error only modestly affects the redshift dispersion to $I_{AB} \sim 24$, the fraction of outliers increases to as much $\sim 15\%$, and the catastrophic fraction roughly doubles to 8%. Clearly just using the maximum likelihood values of the redshift, as we have done above, is problematic in statistical analyses of these faint galaxies.

4.4   Error Measures for Photometric Redshifts

There are two philosophically different ways of quantifying the errors in photometric redshift techniques, leading to the possibility of confusion in comparisons between surveys. Due to the difficulty of estimating meaningful statistical errors, the first photometric redshifts were for the most part computed without such errors (e.g. Hogg et al. 1998, Weynmann et al. 1999), and the accuracy of the method could only be ascertained in comparison with spectroscopic redshifts of the same galaxies. While such dispersions
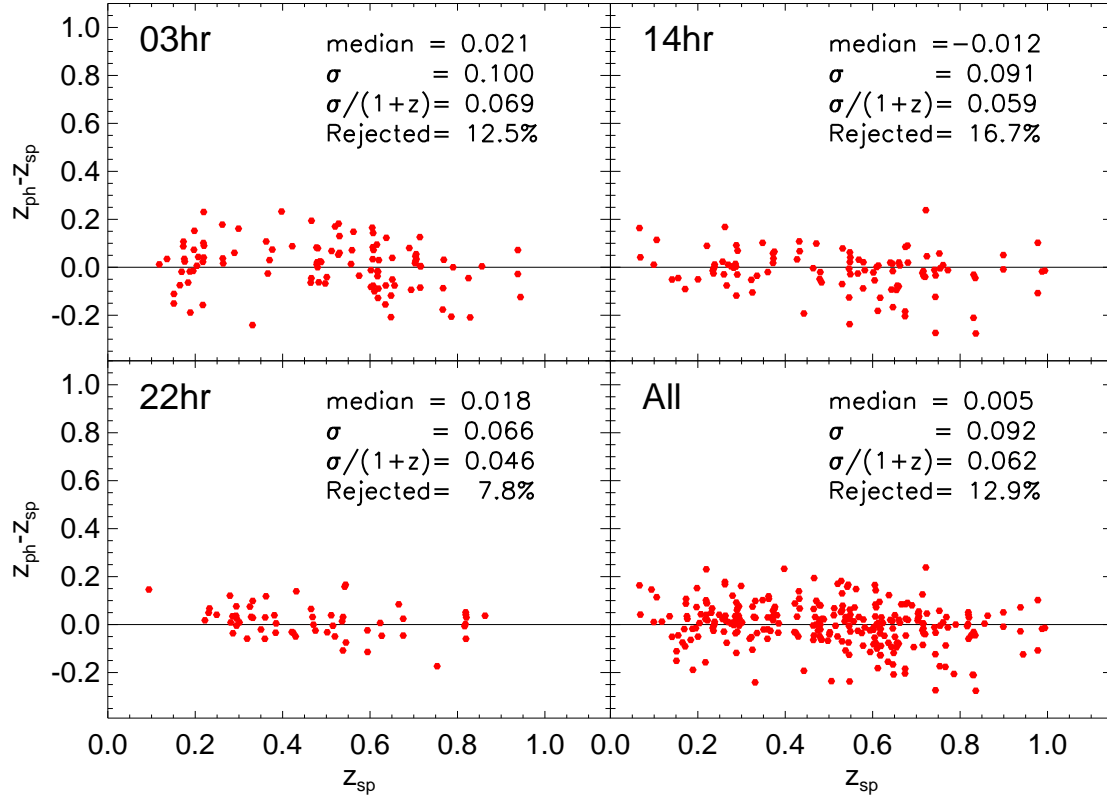
Figure 4.3 Residuals in photometric vs. spectroscopic redshift galaxies to $I_{AB} \leq 24.0$. The difference in imaging depths between the three CFDF–PRS fields is becoming apparent. In the 22hr field, the redshift dispersion and number of outliers is largely unchanged from the brighter sample in Figure 4.2. In contrast, the number of outliers has roughly doubled to 17% in the 14hr field. The redshift dispersions, in each field and overall, are still less than $\sigma \sim 0.1$ to $I_{AB} \sim 24.0$.

were typically of order $\sigma \lesssim 0.1$, a small fraction of objects had drastic redshift errors ($\Delta z \sim 2-3$) caused by either the aliasing of the 4000 Å and Lyman breaks or by the absence of both continuum breaks in the broad–band imaging. These cases represent true failures of the method and are qualitatively similar to a common error in spectroscopic redshift surveys, termed a "catastrophic" error by Yee et al. (1996), in which the single emission line in a faint galaxy spectrum is misidentified. This term has come to represent any large deviation of the photometric redshift from the correct spectroscopic redshift.

With the Fernández-Soto et al. (2002) demonstration that the likelihoods generated by template-fitting photometric redshift codes have a valid statistical significance, in which, for example, meaningful 68.3%, 95.4%, and 99.7% confidence intervals can be defined *without* reference to the spectroscopic redshift, a more traditional error measure became well–defined. As with any other physical measurement, a photometric redshift can thus be classified as agreeing with the correct spectroscopic redshift at the 1σ, 2σ, or 3σ level, where these standard deviations are understood to represent the above confidence

intervals despite the non–Gaussian, and often multi–moded nature of the redshift probability functions. Those few objects for which the photometric redshift differs at $> 3\sigma$ can be considered true "outliers" in the traditional sense, although the fraction of such objects is likely to exceed the 0.3% expected for a Gaussian distribution. This error measure is far more useful in general as it allows a meaningful estimate of the redshift accuracy for each and every galaxy in a photometric redshift survey. Rather than be limited to simple maximum likelihood redshifts, statistical measurements of the galaxy distribution in such surveys should in general use all the available redshift information by incorporating the complete likelihood functions.

However for many uses of photometric redshifts, such as placing galaxies in relatively narrow redshift bins, or simply splitting them into foreground and background samples about a given redshift, it turns out that the simple catastrophic error fraction is often the most desirable quantity. This is particularly true in situations where incorporating the full likelihood information is not practical or possible. Therefore in the next Section we characterize the catastrophic errors in the CFDF–PRS as a function of limiting magnitude, for use in estimating systematic errors in our science analyses in Sections §6.5 and §7.5, and as a guide for other ongoing and planned photometric redshift surveys. In Section §4.7 we return to the statistical error definition, and explicitly demonstrate the validity of the confidence intervals derived from our redshift likelihood functions.

4.5 Characterization of Catastrophic Errors

We use the procedure described in Section §4.3 to produce fainter versions of the CFRS spectroscopic sample with the goal of characterizing the dependence of catastrophic errors on the signal–to–noise in the photometry. Figure 4.4 plots the observed catastrophic failure fraction, again defined for simplicity as $|z_{\mathrm{ph}} - z_{\mathrm{sp}}| \equiv \Delta z_{\mathrm{cf}} \geq 1.0$ (filled symbols), vs. the various limiting magnitudes (top axis) to which we transformed the CFRS sample. As a reference for future photometric redshift surveys, we also plot the failure rate for catastrophic error definitions of $\Delta z_{\mathrm{cf}} \geq [0.5, 0.25]$ (open symbols).

The bottom axis shows how the catastrophic fraction depends on the corresponding signal–to–noise. The exposure times in the CFDF–PRS have been designed to produce roughly similar signal–to–noise levels in all filters for a typical galaxy. As such, the signal–to–noise axis, computed for the average I_{AB}–band depth, is nevertheless representative for all our filters.

Obviously the curve in Figure 4.4, an empirical fit to the data (fitted in the log–log space shown in the inset), is specific to the CFDF–PRS, and cannot be blindly applied to other surveys. It depends on the number and wavelength coverage of the filters, the relative filter–to–filter photometric depths, and
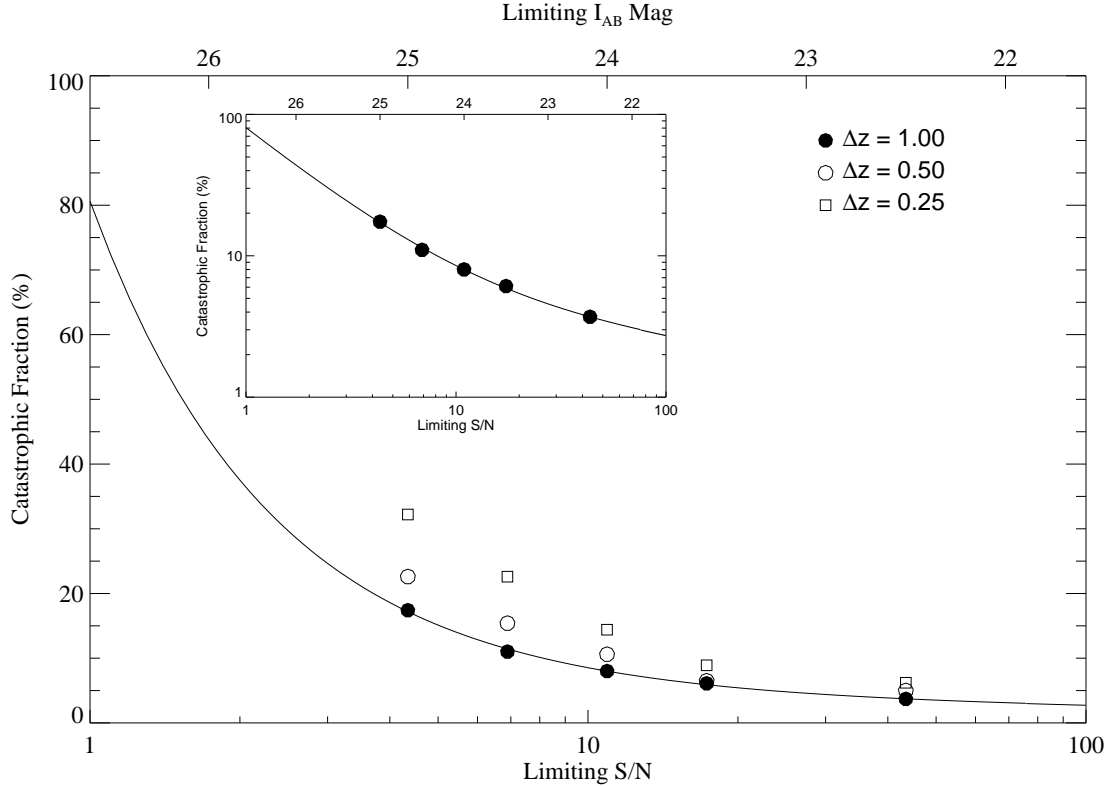
Figure 4.4 Catastrophic error fraction as a function of minimum signal–to–noise in the CFDF–PRS. The points are derived from the fainter versions of the CFRS spectroscopic sample as explained in Section §4.3. The inset shows the same plot in the log–log space in which the empirical curve was fitted.

the photometric redshift algorithm (particularly the template SEDs). Nevertheless, for similar surveys the results are likely generic, in the sense that as the S/N approaches unity, the method breaks down completely. At the other extreme, there is an asymptotic catastrophic error fraction level of around 1%–2% which it will be difficult to transcend with the empirical galaxy templates used in this work.

For high signal–to–noise studies, like the HDF and UDF, the inclusion of rare object templates (e.g. ULIRGS, EROS, AGN, etc...) to the traditional elliptical, spiral and starburst templates of the present study may allow virtual elimination of catastrophic errors. However, for wide–field studies with more modest S/N levels, the addition of such rare templates may actually increase the catastrophic fraction since the data is not of sufficient quality to differentiate amongst all the templates. A minimum template basis spanning the full color range, as in the present study, is likely optimal at modest (~ 10) signal–to–noise.

To the CFDF–PRS limit of $I_{AB} = 24$ there is little difference between the $\Delta z_{cf} \geq 1.0$ and $\Delta z_{cf} \geq 0.5$ catastrophic error fractions, whereas for $\Delta z_{cf} \geq 0.25$ the catastrophic fraction begins to rise as the error level is approaching the tail of the photometric redshift error distribution. For ensemble statistical

measurements like the redshift distribution, the relatively small catastrophic error fraction to $I_{AB} = 24$ does not significantly affect our results, as demonstrated in the Monte Carlo simulation described below. Nevertheless, we will utilize the empirical fit of Figure 4.4 to try to estimate the potential systematic errors introduced to our results by catastrophic errors (c.f. Sections §6.5, §7.5).

One caveat in using our method for estimating the occurrence of catastrophic errors with the $I_{AB} <$ 22.5 CFRS spectroscopic catalog of $z \leq 1.3$ galaxies is that high redshift galaxies near our faint magnitude limit are not explicitly included. Should they have spectral properties not spanned by our template set they could potentially introduce additional redshift degeneracies. We are reassured by photometric redshift studies of the HDF (e.g. Fernández–Soto et al. 2001), which we have successfully reproduced with our code, that demonstrate that our templates do in fact span the full range of galaxy properties to $z \sim 6$, with the blue starburst templates becoming prominent above $z \gtrsim 2$. Certainly to $I_{AB} < 24$ there is no indication of a population of galaxies with anomalous observed–frame optical SEDs. We explicitly test a subset of the faint, high redshift tail of the galaxy distribution in the next Section and find no discrepancy with the prediction of Figure 4.4.

4.6   Photometric Redshift Accuracy for $z \sim 3$ Lyman Break Galaxies

To test the photometric redshift algorithm at redshifts much higher than the CFRS, we have used the Steidel et al. (2003) spectroscopic sample of $z \sim 3$ Lyman Break galaxies (LBGs) present in our 14hr field (their "Groth strip" field). The Steidel et al. (2003) photometry is fainter than in the CFDF–PRS and so we impose a minimum S/N limit of 3 in order to remove objects dominated by noise. As will be explained in Section §5.3.2 this is well below the S/N limit of 10 we will adopt in the CFDF–PRS analysis.

Figure 4.5 shows the redshift residuals for the 104 spectroscopic LBGs for which we compute photometric redshifts. This sample, being extremely limited in redshift space, is instructive in exploring the occurrence of catastrophic redshift errors. The filled symbols are well measured redshifts, whereas the open symbols, representing $\sim 13\%$ of the sample, are catastrophic failures. Neglecting these, the photometric redshifts at $z \sim 3$ have a dispersion of $\sigma/(1+z) \sim 0.05$.

We investigated the source of the catastrophic failures in this faint galaxy sample and concluded it stems from the difference in the U filters between the two surveys. The Steidel et al. (1996) bluer U_n filter allows selection of robust LBG candidates at slightly lower redshifts than our U filter (in which

the Lyman continuum break is only centered at $z \sim 3.2$). The extremely faint $z \sim 2.8$ Steidel et al. (2003) LBGs, without a strong continuum break in any of our filters, suffer from a degeneracy with the $0 \lesssim z \lesssim 0.2$ starburst galaxy types. While approximately 20% of the faint $2.7 \leq z \leq 3.0$ LBGs are misclassified as lower redshift galaxies, only 2% of the $z > 3$ LBGs (and *none* at $z > 3.1$) suffer from this degeneracy. We will make use of these properties in Section §7.5.

Taken as a whole the LBG sample, at a limiting S/N of 3, has a lower failure rate than expected from Figure 4.4. This is not surprising since the Lyman Break selection criteria is designed specifically for broad–band photometric techniques. However the 20% failure rate for the $z \lesssim 3.0$ LBGs that *don't* contain a strong photometric redshift signal are consistent with the prediction from Figure 4.4.

It is important to note that, in addition to only using objects with $S/N \geq 10$, for the core results of this work we are restricting ourselves to a redshift range which always contains the 4000 Å break. Nevertheless, rare bright high redshift objects can and do scatter down into our sample as expected. We must address this systematic uncertainty in our science measurements.
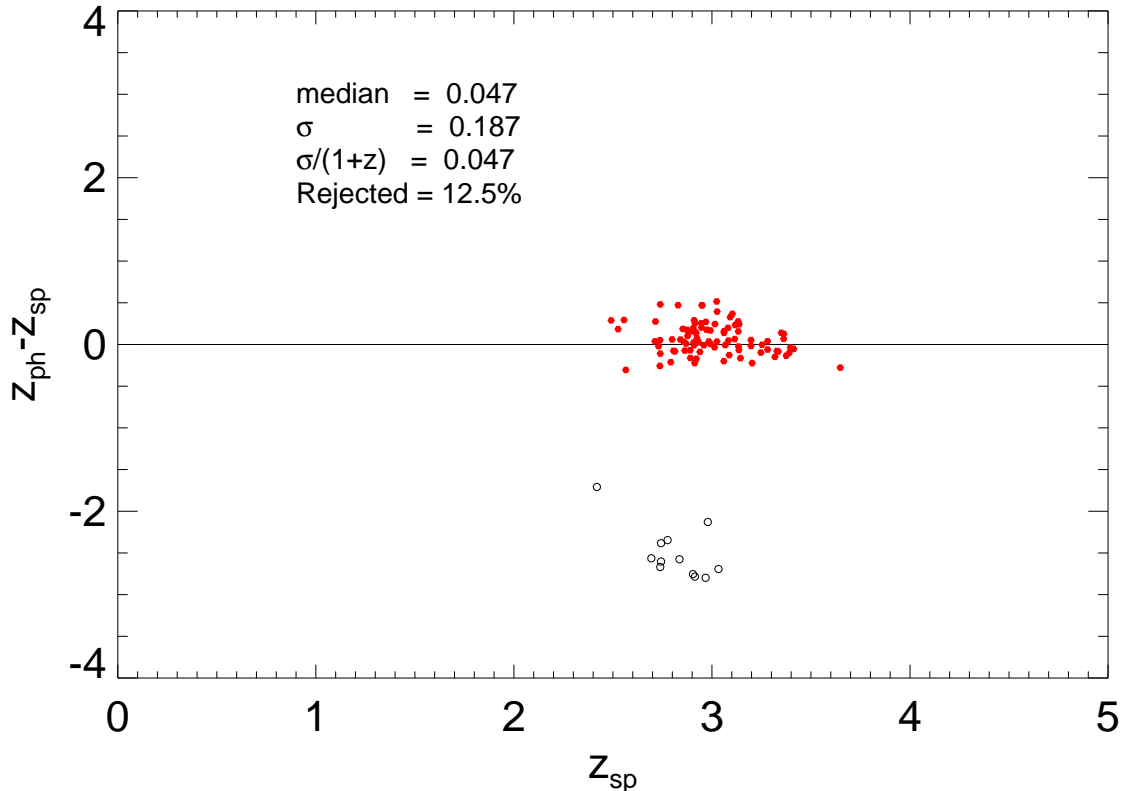
Figure 4.5 Redshift residuals vs. spectroscopic redshift for 104 Steidel et al. (2003) Lyman Break galaxies with $S/N \geq 3$ in the CFDF–PRS 14hr field. Excluding catastrophic errors (open symbols), the dispersion in redshift is $\sigma/(1+z) \sim 0.05$. The galaxies with catastrophic errors, roughly $\sim 13\%$ of the sample, are clustered below $z \sim 3$ where our filters do not straddle a strong continuum break.

4.7   Characterizing the Redshift Likelihood Functions Via Confidence Intervals

In Chapter 5 we will introduce a new method of calculating the galaxy redshift distribution, $N(z)$, in photometric redshift surveys using the full redshift likelihood function for each galaxy. In this Section we characterize the error properties of our likelihood functions using the CFRS spectroscopic sample. Following Fernández-Soto et al. (2002) we define the 1σ, 2σ, and 3σ confidence intervals as those redshift regions which enclose the top 68.3%, 95.4%, and 99.7% of the area in our normalized redshift likelihood functions.

We found that convolving our likelihood functions with a Gaussian with $\sigma = 0.04$ produced approximately normal confidence level statistics, as shown in Table 4.1, and has the beneficial effect of smoothing the likelihood functions. We note that the smoothing kernel is less than our redshift dispersion of ~ 0.06 measured with the CFRS spectroscopic sample. Examples of representative likelihood functions for $I_{AB} = [21,\ 22,\ 23,\ 24]$ galaxies are shown in Figure 4.6.
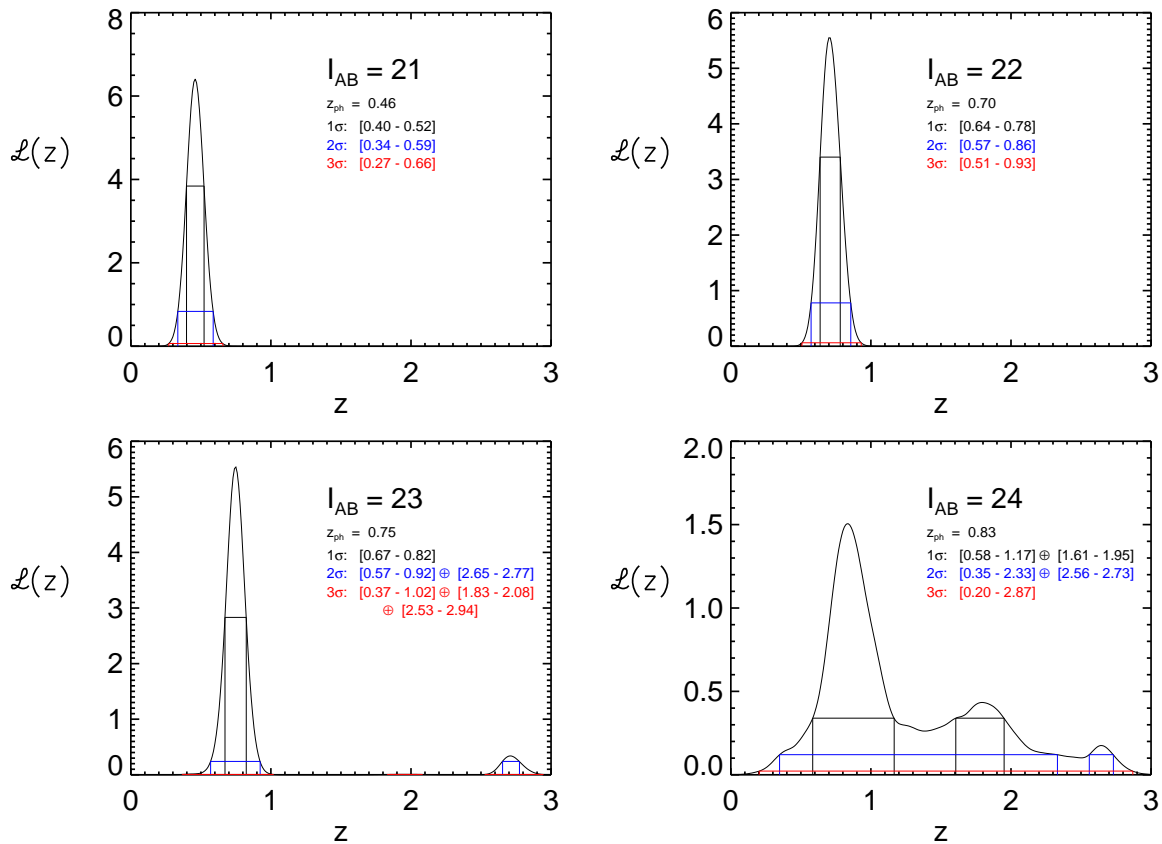
Figure 4.6 Typical likelihood functions with 1σ, 2σ, and 3σ confidence intervals for increasingly fainter galaxies. At the survey limit the likelihood functions become multiply–peaked, leading to disjoint, but nevertheless statistically valid confidence intervals.

Table 4.1.   Statistics of Confidence Intervals Derived from Redshift Likelihood Functions for CFRS

Spectroscopic Galaxies.

Confidence Interval	Observed Number	Expected Number
$\leq 1\sigma$	235/321	$219\ ^{+16}_{-15}$
$\leq 2\sigma$	306/321	$306\ ^{+19}_{-18}$
$\leq 3\sigma$	315/321	$320\ ^{+19}_{-18}$
$> 3\sigma$	6/321	$0.9\ ^{+2.2}_{-0.8}$

Brighter than $I_{\mathrm{AB}} \lesssim 23.5$ our likelihood functions are overwhelmingly single–peaked, approximately Gaussian probability distributions, with relatively little probability density in secondary peaks. At the survey limit, however, the secondary peaks become increasingly significant, often leading to multi– moded, disjoint confidence intervals even at the 1σ level. The confidence level statistics are nevertheless quite consistent with a Gaussian error distribution within the Poissonian errors, as shown in Table 4.1, although we place a slightly higher fraction of galaxies beyond the 3–σ error limit. The Poisson errors on the expected number of galaxies are computed using the Gehrels (1986) expressions valid for small numbers of events.

This exercise verifies the statistical validity of our redshift likelihood functions and of the analyses presented in Chapters 6 and 7 that incorporate them.

Chapter 5

Method: Constructing Accurate Photometric Redshift Distributions

Several groups have published redshift distributions based on photometric redshifts in the Hubble Deep Field (e.g. Gwyn and Hartwick 1996, Sawicki et al. 1997, Fontana et al. 1999). Typically the best–fit photometric redshift is taken as that which maximizes a likelihood function, optionally subjected to a prior in Bayesian analyses (e.g. Benítez 2000). In the limit of narrow, singly–peaked redshift likelihood functions, this approach is a sensible one. Comparisons with spectroscopic redshifts in the HDF have convincingly demonstrated the accuracy and reliability of the photometric redshift method (e.g. Fernández-Soto et al. 2002) under the joint conditions of high quality photometry over a substantial wavelength baseline.

An open question regarding the photometric redshift method is how the signal–to–noise in the photometry affects the resulting redshift distributions. At present, due to the difficulty of obtaining spectra for $AB(8140) > 25$ galaxies, 90% of HDF galaxies with spectroscopic redshifts have photometry with $S/N \geq 100$ (Fernández-Soto et al. 2002). The photometric redshift technique has not been adequately tested at the lower S/N levels more common in ground–based imaging surveys. The method presented below addresses this issue in the CFDF–PRS and in anticipation of the next generation of wide–field imaging surveys (such as the CFHT Legacy Survey).

Detailed Monte Carlo simulations (described below) demonstrate that simple maximum likelihood photometric redshift methods increasingly fail to reproduce the underlying redshift distribution at lower S/N ($\lesssim 20$). This Chapter describes a Bayesian method for recovering the underlying $N(z)$ at still more modest S/N levels using the ensemble redshift information present in the data.

5.1   Bayesian Photometric Redshift Distributions

As described in detail in Benítez (2000), Bayesian statistics provide a way to incorporate our knowledge about the galaxy distribution to improve the photometric redshift accuracy. This is accomplished through the use of priors on the simple likelihood functions, which by nature assume all redshifts are a priori equally likely. The prior converts the likelihood functions into true Bayesian redshift probability distributions which can be incorporated directly into cosmological studies in place of traditional spectroscopic redshifts (which, in general, can be thought of as approximately δ–function redshift probabilities). Specifically,

$$P(z, T) \propto P[z, T \,|\, N(z)\,] \times \mathscr{L}(z, T) \tag{5.1}$$

where $\mathscr{L}(z, T)$, the likelihood of measuring the observed colors for a galaxy of spectral type T at redshift z, is given in equation 4.1. In the Bayesian interpretation $P[z, T \,|\, N(z)\,]$ is a prior, in this case the probability of drawing a galaxy with redshift z and type T from a redshift distribution $N(z)$. This prior, applied to the likelihood function, incorporates the basic fact that all redshifts are not a priori equally likely. As the goal here is to measure a statistical property of the galaxy population, namely its redshift distribution, requiring this information a priori may appear somewhat circular. However, we have devised an iterative scheme to recover the underlying redshift distribution and tested it in detailed Monte Carlo simulations.

5.2   Direct summation of $N(z)$ and Iteration

Rather than adopting the simple maximum likelihood (ML) value of each galaxy redshift, we choose instead to directly sum up the normalized likelihood functions, $\mathscr{L}^n$, of each galaxy in the photometric sample. This would trivially produce the correct redshift distribution in the limit of spectroscopic (i.e. δ–function) input redshifts. For photometric redshifts in the high signal–to–noise regime this method yields approximately the same result as collapsing the $\mathscr{L}^n$ to the single maximum likelihood redshift since the $\mathscr{L}^n$ are typically single sharp Gaussians. At fainter magnitude limits, the likelihood functions become broader and often develop multiple peaks as degeneracies between distinct templates at different redshifts arise with the increasing photometric error. With simple ML redshifts the derived $N(z)$ is both too broad and has artificial peaks as significant numbers of galaxies are shifted between these degenerate redshifts. This is true as well of the first step of our iterative method:

$$N^0(z) = \sum_i \mathscr{L}_i^n(z) = \sum_i \frac{\mathscr{L}_i(z)}{\int_0^\infty \mathscr{L}_i(z)\,dz}. \tag{5.2}$$

This zeroth order redshift distribution, $N^0(z)$, is then used as the prior, $P[z, T | N(z)]$, in an iterative solution to equation 5.1. This prior uses the bulk information present in the galaxy colors to modify the raw likelihoods so as to minimize the degeneracies and, in effect, deconvolve the individual likelihood functions of the low S/N broadening effect. The resulting distribution serves as the first order prior, $N^1(z)$, and the procedure can be carried on to convergence, which, as shown in the following Section, is so rapid that additional steps are unnecessary.

Obviously the method breaks down at very low signal–to–noise. In the CFDF (and hence in the simulation described below) the sky background is brightest in the Z–band, limiting its depth compared with the other filters. This filter is doubly important as the red end of the wavelength baseline in the survey. At S/N $\lesssim 10$ the method increasingly fails to converge to the input redshift distribution, underlining the importance of accurate Monte Carlo simulations to fully characterize photometric redshift surveys, and in particular, to determine their effective magnitude limit.

5.3   Convergence Properties

This method makes the assumption that a single prior is applicable to galaxies of all brightnesses and spectral types in a given sample. Ideally, each subclass of galaxies should have its own unique prior to optimally weight the simple likelihood functions. Obviously the a priori redshift likelihoods of large bright elliptical galaxies and faint blue Lyman break galaxies are quite different. The use of a single statistical prior, in this case the iteratively estimated redshift distribution, to describe a complete magnitude limited sample is obviously a rough approximation. However, with sufficient signal–to–noise in the photometry we demonstrate in the next few sections that it works surprisingly well.

This should not be mistaken to imply that redshifts of individual galaxies are uniformly improved using this method. It is the complete statistical redshift distribution that is demonstrably improved compared with that obtained via the standard method of collapsing the redshift likelihood function of each galaxy to a single maximum likelihood redshift.

5.3.1   Formalism

Generalizing Equation 5.2 to include a single prior, $P(z)$, for a given sample

$$\mathcal{N}(z) = P(z) \sum_i \frac{\mathcal{L}_i(z)}{\int_0^\infty P(z)\,\mathcal{L}_i(z)\,dz}, \tag{5.3}$$

we see that the correct prior is the one for which $\mathcal{N}(z) = N(z)$ (i. e. we recover the correct underlying redshift distribution). This leads to the following integral equation for $P(z)$:

$$P(z) = N(z) \left(\sum_i \frac{\mathscr{L}_i(z)}{\int_0^\infty P(z)\,\mathscr{L}_i(z)\,dz} \right)^{-1}, \tag{5.4}$$

which can be solved by iteration. Note that the functional form of the ideal prior depends on the likelihood functions, as expected since at very low S/N (reflected in the likelihoods) the method should fail. Viewing the prior as expressing a change of coordinates to a space in which the galaxy distribution is flat, one might expect the prior to be similar to $N(z)$. Therefore, we can use simulations to determine the redshift and S/N regimes in which taking $P(z) = N(z)$ produces the correct answer (i.e. $\mathcal{N}(z) = N(z)$). It is straightforward to show that this requires

$$\eta \equiv \sum_i \frac{\mathscr{L}_i(z)}{\int_0^\infty N(z)\,\mathscr{L}_i(z)\,dz} = 1 \tag{5.5}$$

When this equation is satisfied, using $N(z)$ as the prior is strictly correct. Although in general $N(z)$ is not known a priori, assuming that $N^0(z)$ from Equation 5.2 is a reasonable approximation to $N(z)$, one might still expect that

$$\eta^0 \equiv \sum_i \frac{\mathscr{L}_i(z)}{\int_0^\infty N^0(z)\,\mathscr{L}_i(z)\,dz} \approx 1 \tag{5.6}$$

is a valid convergence criterion.

5.3.2   Convergence in Simulations

The convergence properties of the iterative method, studied in the Monte Carlo simulations described in the next Section, demonstrate its feasibility.

With sufficiently high signal–to–noise the iterative method converges after a single iteration. This is easily understood, as the likelihood functions are expected to be both narrow and overwhelmingly single–peaked. At very low S/N, the method ceases to converge and incorrect peaks in the iterative $N(z)$ priors do not damp away, but remain constant or even increase in amplitude due to a kind of feedback loop. This shows the necessity of understanding the noise properties of photometric redshift surveys using accurate Monte Carlo simulations.

In the CFDF–PRS we set a conservative I–band S/N minimum of 10, based on a direct calculation of the convergence criteria of Equations 5.5 and 5.6 (shown in Figure 5.1), as well as the results of the Monte Carlo simulations described below. This corresponds to a limiting magnitude of $I_{\mathrm{AB}} \sim 24$. The redshift range over which the method is reliable, apparent from Figure 5.1, is $0.2 \lesssim z \lesssim 1.3$, in very good agreement with the predictions for our filter set (Brodwin et al. 1999). In this redshift range and to
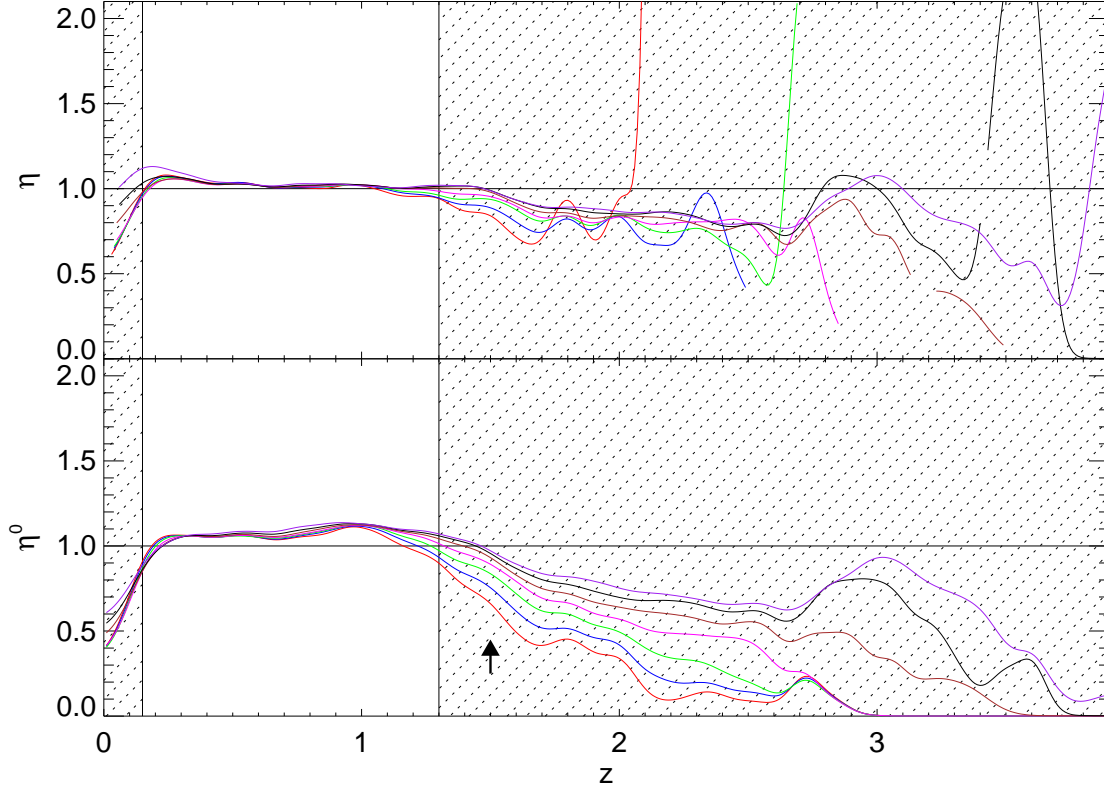
Figure 5.1 Convergence criteria η and η^0 of Equations 5.5 and 5.6, calculated in the Monte Carlo simulation of Section 5.4. The unshaded region between $0.2 < z < 1.3$ is identified as the most trustworthy for recovering the underlying redshift distributions for magnitude limited samples down to $I_{AB} \sim 24$. The curves represent samples down to limiting magnitudes of $I_{AB} \leq 22.5$ (directly above arrow), rising to $I_{AB} \leq 24$ in increments of 0.25 magnitudes. The curves in the top panel are undefined where $N(z) = 0$ for bright magnitude limits at high redshift. The smoothing effect of the photometric redshift errors prevents this occurrence in the lower panel.

this magnitude limit the iterative method outperforms the simple ML method at reproducing the input redshift distributions in our simulations.

5.4 Test of the Method: Monte Carlo Simulation

The iterative method described above was extensively tested in detailed Monte Carlo simulations. Briefly, model Universes were populated according to CNOC2 evolving luminosity functions (Lin et al. 1999) for early, intermediate and late spectral types, modified to produce a range of reasonable input redshift distributions to $z > 3$. These model galaxies were assigned colors using the empirical template set used in the CFDF photometric redshift code, ranging from the CWW Elliptical (Coleman et al. 1980) to the Kinney et al. (1996) SB2. Flux errors matching the *UBVRIZ* photometry in the CFDF fields were

applied to these galaxies, and photometric redshift likelihood functions were computed for galaxies in an area of 0.5 deg^2. A systematic error not accounted for in this simulation is the possible incompleteness of the adopted template SEDs with respect to the true range of galaxy properties. This was approximately accounted for following the method of Fernández-Soto et al. (2002) by convolving the computed redshift likelihood functions with a variable–width Gaussian.

$$\mathcal{L}^c(z) = \int_0^\infty dz' \, \mathcal{L}(z') \, G\left[z|z', \Sigma(1+z')\right] \tag{5.7}$$

where G is a normalized Gaussian (truncated at $z < 0$) of median z' and $\sigma = \Sigma(1+z')$. Σ was set to 0.05 based on a detailed comparison with CFRS spectroscopic redshifts, as described in Section §4.2 (in fact, this is $\sim 20\%$ larger than was found for the CFRS, but was adopted in a conservative vein).

5.4.1   Simulation Results

In the interest of clarity we briefly recall the various methodologies our simulation was designed to test. The basic technique for computing redshift distributions consists of making a simple histogram of the best–fitting photometric redshifts for each galaxy. This is identical to taking the redshift that maximizes the likelihood function in likelihood-based fitting algorithms. We therefore dub this the *Peak–ML* method. Our new method, essentially a two–step iterative process, uses the full redshift likelihood function for each galaxy in computing $N(z)$. We therefore label it the *Full–RLF* iterative method (sometimes referred to simply as the *RLF* method for brevity). Redshift distributions were computed using both the Peak–ML method and the Full–RLF iterative method, and compared to the input $N(z)$. While the final iteration of the Full–RLF method is superior down to $I_{AB} \leq 24.0$, the improvement is most pronounced for the $I_{AB} \leq 23.5$ sample, which we plot in Figures 5.2 and 5.3.

Figure 5.2 plots the redshift distributions obtained with the various methods. The filled and open circles represent the input (model) and Peak–ML redshift distributions, respectively. The dashed and solid lines show the Initial and Final iterations of the RLF method, respectively.

At first glance, all the methods appear to reproduce the input $N(z)$ quite well. However, upon closer examination, it is clear that the Initial RLF $N(z)$ is inferior to both the Peak–ML and the Final RLF distributions. On a qualitative level, we see that an incorrect secondary peak at $z \sim 1.8$ draws galaxies away from the main peak at $z \sim 0.7$. This problem is most acute for the Initial RLF method, but is nevertheless evident in the Peak–ML points. The Final RLF method appears to suffer less from the effect of this photometric redshift degeneracy.

In fact, the trends observed with the different methods can be easily understood. Objects with little redshift ambiguity (i.e. narrow, singly–peaked redshift likelihood functions) contribute to the different
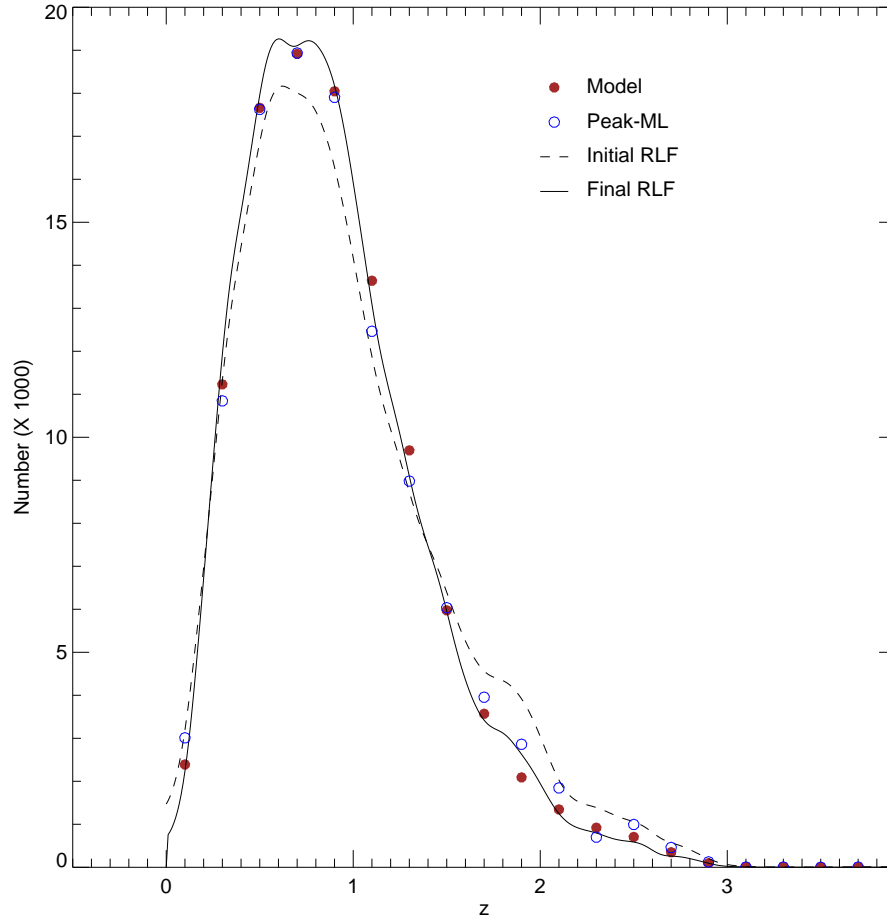
Figure 5.2 Results of Monte Carlo simulations testing Peak–ML (open circles), Initial RLF (dashed curve) and Final RLF (solid curve) methods for computing $N(z)$ in a photometric redshift survey. The filled circles show the input (model) $N(z)$. The Peak–ML and Final RLF methods both recover the underlying $N(z)$ quite faithfully, but the latter is in fact significantly better as discussed in the text and illustrated in Figure 5.3. Note how the aliased peak at $z \sim 1.8$ in the Initial RLF iteration is strongly suppressed in the Final RLF distribution, reproducing the model $N(z)$ better even than the Peak–ML method.

$N(z)$ measures in the same, correct way. On the other hand, those objects whose redshift likelihood functions show a strong degeneracy (i.e. at least two similar peaks at distinct, aliased redshifts) contribute to $N(z)$ in quite different ways in the above methods. In these cases the Peak–ML method usually selects the correct redshifts, although the catastrophic fraction increases with decreasing S/N. The main features of the input $N(z)$ are therefore fairly well reproduced, although small peaks from the catastrophic errors will arise at specific aliased redshifts. The Initial RLF method, as the direct sum of the likelihood functions, will always underpredict the main $N(z)$ peak as *all* the probability density of incorrect peaks at aliased redshifts is removed from it, leading to quite large peaks at the aliased redshifts. The Final RLF method, which uses the Initial RLF distribution as a prior, strongly suppresses these incorrect
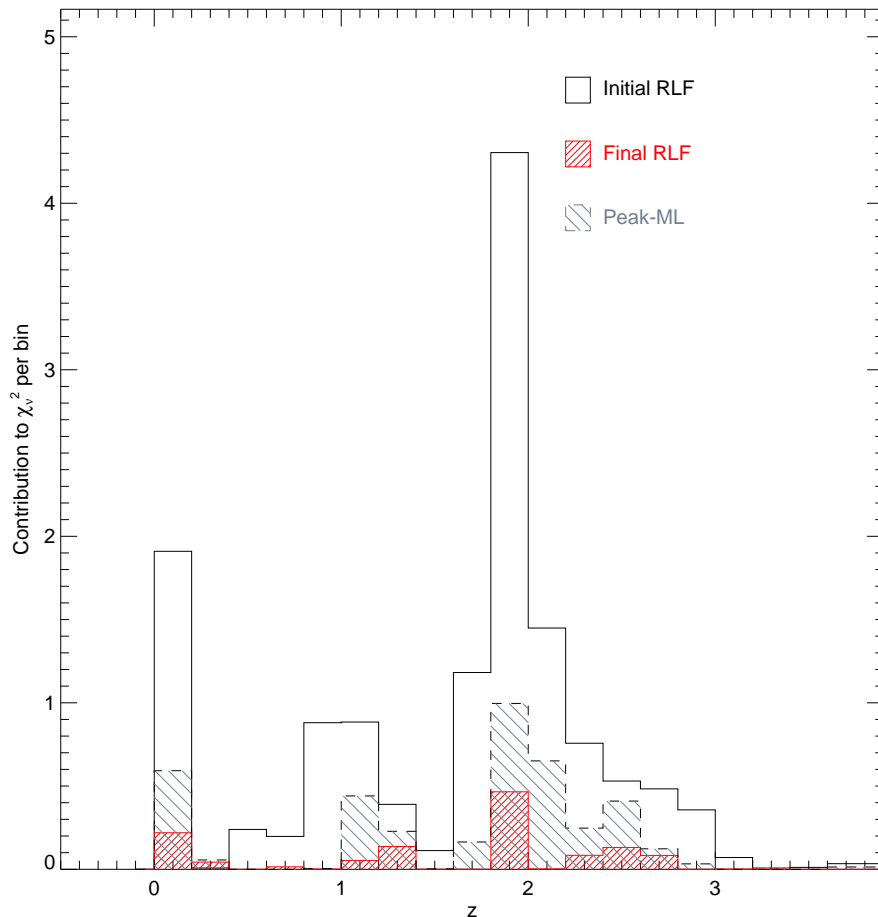
Figure 5.3 Contribution to χ^2_ν from each redshift bin for the Peak–ML (sparsely filled histogram), Initial RLF (empty histogram) and Final RLF (densely filled histogram) methods. Note the significant improvement over the Initial RLF method provided by both the Peak–ML and Final RLF distributions. The advantage of the Final RLF over the Peak–ML method is also apparent, as the differential χ^2_ν of the former is lower in each bin, often dramatically. The total χ^2_ν (i.e. integrating over redshift) for these samples is {Initial RLF, Peak–ML, Final RLF} = {14.5, 4.02, 1.25}.

peaks using the information contained in the bulk of the galaxy sample (which is, on the whole, correct), bringing most of the ambiguous redshifts into line. A quantitative analysis demonstrates the superiority of the Final RLF method, and shows that it represents a significant improvement over the Peak–ML method.

To quantitatively assess the different methods we compare the resulting $N(z)$ of each method to the input $N(z)$ using a χ^2 test. To make a fair comparison, we integrate the iterative method curves over each Peak–ML redshift bin to produce a binned version of the iterative method for the χ^2 tests. The Initial RLF redshift distribution has a reduced $\chi^2_\nu = 14.5$ when compared with the input $N(z)$. The Peak–ML method, unsurprisingly, is much better, with $\chi^2_\nu = 4.02$. It should be remembered that photometric redshift errors are not formally Gaussian. In fact in the low S/N regime, where multiple

peaks arise, the error distribution is patently non–Gaussian, rendering impossible a direct confidence interval interpretation of the absolute χ^2 values. However, regardless of the nature of the photometric error distribution, reductions in χ^2 should indicate relatively better fits. In the Final RLF method the distribution no longer suffers from the effects of the redshift aliasing. The curve runs through (or very near) all the input $N(z)$ data points, and the χ^2_ν drops to 1.25.

Figure 5.3 shows the individual contribution from each redshift bin to the total value of χ^2_ν for each method. The dramatic improvement from the Initial RLF (empty histogram) to Final RLF (densely filled histogram) is evident. The resulting $N(z)$ has smaller deviations from the input distribution in every bin compared with the Peak–ML redshift distribution (sparsely filled histogram).

It is interesting to note that in this simulation the iterative method accurately recovers the redshift distribution outside the "guaranteed–convergence" redshift range of $0.2 \lesssim z \lesssim 1.3$ discussed in Section §5.3.2. Various input redshift distributions and binnings have been investigated, with results consistent with those shown in Figures 5.2 and 5.3.

In addition to the χ^2 tests Kolmogorov–Smirnov (K–S) statistics were computed for all methods. The same pattern emerges, in which the Peak–ML method produces a redshift distribution more consistent with the input distribution than the Initial RLF method, but much less consistent than the Final RLF method. In this test the results are not impressive in either of the former two cases, with the somewhat better Peak–ML redshift distribution matching the input distribution at a probability of only 10^{-3}. This is perhaps not surprising given the relatively high χ^2 test result. On the other hand, the final iteration of the Full–RLF method has a K–S probability of 0.31 of matching the input distribution, which is the level of variation expected in a Poisson sampling of the underlying distribution.

Chapter 6

Photometric Redshift Distributions

in the CFDF–PRS

The iterative method was applied to the CFDF–PRS catalogue described in Chapter 2. The uniform magnitude selection is more representative of the general galaxy population than surveys that preselect their targets with color cuts (e. g. Coil et al. 2004), or have complicated spatial selection functions (e. g. Hogg et al. 2000). The $I_{\mathrm{AB}} \leq 24$ and $R_{\mathrm{AB}} \leq 24.5$ redshift distributions, presented in this Chapter, are quite complementary with current lensing studies (Maoli et al. 2001, Réfrégier et al. 2002, Van Waerbeke et al. 2001; 2002, Bacon et al. 2003, Hamana et al. 2003). At bright magnitudes our results can be compared directly with the CFRS redshift distributions (Crampton et al. 1995, hereafter CFRS5). Unless otherwise noted all distances in this Chapter are given in comoving Mpc assuming a WMAP (Spergel et al. 2003) cosmology $\{\Omega_M, \Omega_\Lambda\} = \{0.27, 0.73\}$ with Hubble parameter $h = 0.71$.

6.1 Comparison with the CFRS

The three CFDF–PRS fields contain 3 of the 5 small fields in which the CFRS survey was carried out. We can therefore compare the redshift distributions of each field individually, as well as the aggregate results for the two surveys to the CFRS limit of $I_{\mathrm{AB}} = 22.5$. It is important to stress that these surveys are completely independent. The imaging data was taken with different cameras and filters, and the photometric calibrations are entirely independent. The CFRS magnitudes are isophotal, whereas in the CFDF we use SExtractor (Bertin and Arnouts 1996) total magnitudes (MAG_AUTO).

Figure 6.1 compares the $18.5 \leq I_{\mathrm{AB}} \leq 22.5$ redshift distributions in each common field as well as for

the sum of the fields. The solid curve is the Final RLF redshift distribution, the open circles represent the Peak–ML method, and the histogram is the original CFRS redshift distribution. The agreement in all three fields is remarkable, though not at all tautological. To this depth the CFDF–PRS contains over 20 times the number of galaxies present in each CFRS field. Nevertheless the striking field to field differences in $N(z)$ discussed in the CFRS persist in the present much larger survey. As discussed in CFRS5 these differences are not statistically significant for the small number (~ 100) of galaxies in each field when the effect of clustering is taken into account.

Following the method of CFRS5, we estimate N_C, the number of excess galaxies associated with each galaxy (including itself), for the CFRS spectroscopic sample to be $N_C \sim 2$ (see Section C.1 in Appendix C for complete details). For a Poisson–distributed sample $N_C = 1$ (i.e. the fluctuations in number density depend only on the individual galaxies), whereas the presence of small–scale clustering produces $N_C > 1$. This is just a reflection of the fact that correlated galaxies effectively come in clumps of N_C galaxies. Reducing the number of independent galaxies in the CFRS by this factor, we find that the CFDF–PRS redshift distributions are entirely consistent with the original CFRS results, in each field and for the sum of the fields, despite the persistence of strong field–to–field differences (in particular between the 03hr and 22hr fields). It is perhaps surprising that the redshift distributions are not more homogeneous, given the half degree field sizes and a ~ 2000 (comoving) Mpc baseline to the median redshift of the CFRS.

To test whether the field–to–field variations *within* the much larger CFDF–PRS itself are indicative of non–homogeneity of the galaxy distribution, we scale the value of N_C found in the CFRS for the larger field size (integrating a $\theta^{-0.8}$ correlation function) and spatial sampling (simple proportionality) of the CFDF–PRS, to arrive at $N_C \sim 15$ (see Section C.2 for details). Reducing the number of independent galaxies by this factor, we find no convincing evidence of large scale anisotropies on the scales probed, beyond those attributable to small–scale galaxy correlations. However, those correlations do cause significant $N(z)$ variations on at least $30'$ scales (~ 30 comoving Mpc at $z = 1$).

The impressive agreement between the CFRS and the CFDF–PRS to $I_{\mathrm{AB}} \leq 22.5$ is a firm demonstration of the excellent control of systematic errors in the survey, as well as of the accuracy of the photometric redshift code and the iterative $N(z)$ algorithm. Indeed it was on the strength of this agreement, despite the completely independent systematic errors of the two surveys, that we came to fully trust our photometric redshift distributions with their dramatic field–to–field differences and double peaked nature.

6.2 CFDF–PRS $I_{AB} \leq 24$ Redshift Distribution

Pushing beyond the CFRS limit, we present in Figure 6.2 the redshift distribution to $I_{AB} \leq 24$ for the full CFDF–PRS. The curve is the final iteration of the Full–RLF method, and the Peak–ML distribution is represented by the points. As expected, the main difference between these methods in the $0.2 \leq z \leq 1.3$ convergence region (between the vertical dashed lines) is a relative paucity of objects in the Peak–ML method near the median redshift as these objects were scattered to one of the photometric redshift degeneracies at $z \sim 1.5$ and $z \sim 2.7$. The Full–RLF partially corrects this effect, though a small fraction of objects remain clustered at these redshifts.

For comparison we plot in the inset the expected $z \sim 3$ Lyman break galaxies to $I_{AB} \leq 24$ from Steidel et al. (1999), along with number of LBGs from Foucaud et al. (2003) to this depth, both scaled to a one degree field size. The Foucaud et al. (2003) study is a clustering analysis of LBG candidates photometrically–selected from the original CFDF UH8k imaging survey. As explained in Section §4.6, the Steidel et al. (1996) filter set selects slightly lower redshift LBGs than in the present survey, leading to the small $2.5 \lesssim z \lesssim 3.0$ peak of aliased redshifts. As we focus on the $0.2 \leq z \leq 1.3$ convergence region in this Chapter, we refer the reader to the Foucaud et al. (2003) work for a more detailed discussion of the low redshift interlopers in the Lyman Break sample in the CFDF. We simply note that the LBG densities for both the Steidel et al. (1999) and Foucaud et al. (2003) samples lie roughly between the densities of the Peak–ML and Full–RLF methods, offering a measure of proof that the present results are reasonable even at $z \gg 1.3$.

The distinct characteristics of each field, as well as the evolution from the brighter $18.5 \leq I_{AB} \leq 22.5$ sample are discussed below. We first discuss the theoretical expectations concerning field–to–field variance for our survey geometry.

6.3 Theoretical Expectations for the CFDF–PRS Redshift Distribution

There is a considerable literature on the misleading effects of pencil beam surveys in measuring the 3D density distribution. When Broadhurst et al. (1990) measured an apparent periodicity in the Universe on $128\ h^{-1}$ Mpc scales, Kaiser and Peacock (1991), in a calculation of the 1D power spectrum in realistic survey geometries, concluded that in fact the statistical significance of the Broadhurst et al. (1990) result was quite low. The physical reason is that in projecting the 3D power spectrum down to 1D, power on scales of the smallest survey dimension dominate the contribution to the large scale terms in the 1D

power spectrum. Put another way, the 3D power transverse to the skewer (i.e. redshift) dimension is aliased on the scale of the field width. In fact Kaiser and Peacock (1991) showed that in pencil beam surveys, the clumpiness of galaxies so biases the sampling of the density field on the largest scales that only fluctuations of order unity would be significant on those scales.

With these issues in mind we compare the CFDF–PRS and HDF surveys with regard to the effect of cosmic variance. Current weak lensing studies typically rely on the HDF redshift distributions beyond the CFRS limit of $I_{AB} = 22.5$. The present work represents a significant improvement over the HDF to $I_{AB} = 24$, in particular in minimizing the effect of cosmic variance.

The CFDF–PRS is about 10% the volume of the 2dF at the median redshifts of the respective surveys. The HDF, in comparison, is 0.1% of the 2dF volume. To $z = 1.3$ the CFDF survey fields are 35 Mpc (comoving) across, compared to 3 Mpc for the HDF. With clustering largely limited to scales $\lesssim 15$ Mpc, the effects of cosmic variance should be substantially lowered in the CFDF compared with the HDF. In fact the persistence of field–to–field variations to $I_{AB} = 24$ in the CFDF–PRS (presented in the next Section), while not indicative of large scale inhomogeneities in the Universe, are nevertheless significant for weak lensing studies. They are a strong confirmation that redshift distributions from HDF–sized fields are of extremely limited use, being totally dominated by cosmic variance (e.g. Somerville et al. 2003), and that even with much larger fields, averaging over multiple lines of sight is necessary. We minimally accomplish this with our three widely–separated fields, but more would be ideally required. Nevertheless, the CFDF–PRS redshift distributions represent a substantial improvement over the HDF in terms of area, volume and, of course, limiting the effect of cosmic variance.

6.4   Evolution of $N(z)$ with Survey Depth

Comparing Figures 6.1 and 6.2, we see several trends in the transition from the CFRS depth to the CFDF–PRS limit of $I_{AB} \sim 24$. As expected, the $z > 1$ sample grows as a fraction of the general population, from $\sim 9\%$ to $\sim 30\%$, while the median redshift increases from $z_{med} \sim 0.6$ to $z_{med} \sim 0.8$. Despite the smoothing effects of photometric redshift errors, discrete structures in redshift space are still clearly seen. We give a brief description of the evolution of these structures in each field with survey depth.

03hr Field (RA: 03:03:00   DEC: +00:09:00)

The 03hr field has considerable structure at $0.6 \lesssim z \lesssim 0.7$, including a probable cluster near the middle of the field. This is confirmed in the CFRS spectroscopic catalog which contains at least two

physical associations of galaxies, each with about 15 galaxies within $dz \leq 0.025$ of systemic redshifts of $z \sim 0.605$ and $z \sim 0.702$. Interestingly, the CFRS did not cover the probable cluster (it being outside their survey area), but its presence strongly influenced the large scale structure they observed in this field. In the CFDF–PRS these two redshift space structures influence the redshift distribution in this field down to $I_{AB} = 24$, resulting in a relative paucity of galaxies at $0.3 \lesssim z \lesssim 0.5$, compared with the other fields and with the combined redshift distribution.

In a complementary medium deep XMM survey, Waskett et al. (2003, in preparation) discuss the X–ray sources present in the 03hr and 14hr CFDF fields.

14hr Field (RA: 14:17:10   DEC: +52:24:43)

The 14hr field (Groth Strip) is one of the best studied extragalactic fields (e.g. Groth et al. 1994, Lilly et al. 1995a, Steidel et al. 2003). It is the most normal, in some sense, of our three fields. The picket–fence structure observed in the CFRS has been smoothed out by the photometric redshift errors, while the thirtyfold increase in area provided by the CFDF–PRS has reduced the cosmic variance, leaving a relatively smooth, single–peaked, roughly Gaussian redshift distribution for $z \leq 1.3$. This distribution does not change appreciably in shape to $I_{AB} = 24$, aside from steady increases in median redshift and number density. However, at $z \sim 1.8$ a second peak arises in $N(z)$ as we push to fainter magnitudes. Visual inspection of the galaxies involved indicates nothing unusual — they are entirely likely to be at the photometric redshift. However as this peak is outside our trusted redshift range of $0.2 \leq z \leq 1.3$ we defer a detailed study of it until wide–field infrared imaging or spectroscopic redshifts are available.

The DEEP2 (Davis et al. 2003) redshift survey is targeting this field with the aim of obtaining 5000 redshifts to $I_{AB} < 24.5$. As such, it will perform a valuable check on the results presented here.

22hr Field (RA: 22:17:48   DEC: +00:17:13)

The 22hr field is perhaps the most interesting of the three. There is a large overdensity at $z \sim 0.3$ observed in both the CFRS and the CFDF–PRS to the CFRS limit of $I_{AB} \leq 22.5$. Between $22.5 \leq I_{AB} \leq 24$ the situation changes dramatically, and a broad peak at $z \sim 0.8$ (the median redshift at this depth) emerges. The shape of $N(z)$ in this magnitude interval is quite similar to that in the 03hr field, albeit at slightly higher redshift. As the sample selection deepens from $18.5 \leq I_{AB} \leq 22.5$ to $18.5 \leq I_{AB} \leq 24$ the relative sizes of the $z \sim 0.3$ and $z \sim 0.8$ peaks completely reverse. In addition, there is evidence for a substantial galaxy overdensity at $z \sim 1$.

The VIRMOS–VLT deep spectroscopic survey (VVDS, Le Fèvre et al. 2003) will obtain tens of thousands of spectroscopic redshifts to $I_{AB} < 22.5$ over 3.6 square degrees in this field. Given the

relatively bright magnitude limit, it will be instructive to see whether this is sufficient area to obtain a redshift distribution unbiased by the $z \sim 0.3$ structure seen in our data, and whether it will be deep enough to confirm the existence of considerable structure at $z \sim 1$.

6.5   Median Redshifts in the CFDF–PRS

The extraction of cosmological parameters from weak lensing shear studies is, to good approximation, only sensitive to the median redshift of the galaxy population. While this is a fairly robust statistic, there are two sources of error which may bias the median in a photometric redshift survey such as the CFDF–PRS. The first, cosmic variance, applies equally well to traditional spectroscopic surveys. It is a sort of random error, in the sense that it can be minimized by observing many fields. With only 3 fields the error on the directly measured field–to–field standard deviation is $\sqrt{2/(n-1)} = 100\%$ (Pen et al. 2003), and as such is not particularly illuminating. Nevertheless it is expected to dominate the error budget.

The second source of error, catastrophic failures of the photometric redshift method caused by redshift aliasing in low S/N photometric data, is systematic in nature. The simulations of Section §5.4 indicate the redshift regime which is free of such aliasing ($0.2 \leq z \leq 1.3$), and we in fact use this convergence region in fitting our redshift distributions in Section §6.7. However, catastrophic errors do take place outside this convergence region, as is clear from Figure 4.5, and we would like to investigate the effect of these errors on the median of the full sample.

We make two estimates of the systematic error due to redshift aliasing. The first, and most conservative, adopts the worst–case scenario that *all* redshifts outside the convergence region are untrustworthy, which from Section §4.6 we know is not the case. We compute the median omitting all objects outside the $0 \leq z \leq 1.3$ convergence region, using two one–sided redshift cuts (i.e. $z \geq 0.2$ and $z \leq 1.3$) to estimate the asymmetric maximal systematic error possible in our survey. As an aside, this procedure formally computes only half the maximum theoretical error. To see this, note that applying the $z \leq 1.3$ redshift restriction is equivalent to distributing the omitted high–z galaxies exactly according to the distribution of the $z \leq 1.3$ sample. But that's precisely the same, in terms of the median, as placing half of the high–z galaxies at $z = 0$ (or even just substantially below the median). Therefore the maximum theoretical error, corresponding to placing *all* of the $z > 1.3$ galaxies below the median (i.e. corresponding to the case of 100% catastrophic errors outside our trusted redshift regime), is twice the error obtained from simply omitting them. However, given the impressive results for the $z > 3$ sample in Figure 4.5, and the $\sim 87\%$ overall success rate for the full LBG sample (which is significantly fainter than our survey limits),

the systematic error from our redshift cuts is certainly the maximum possible error in *our* survey. In fact for the reasons just mentioned, it is almost certainly a gross overestimate.

A more realistic estimate of the systematic error is motivated from the catastrophic fractions observed in the CFRS in Section §4.5 as a function of limiting magnitude. We shift the catastrophic fraction of galaxies, as measured in Figure 4.4, from $z \sim 0$ to $z \sim 3$ and vice versa and recompute the median of the resulting distribution in each case to determine the magnitude of the systematic error on the actual survey median. These two cases account for what is seen in both the CFRS and Steidel et al. (2003) LBG samples, where objects are shifted back and forth between $0 \lesssim z \lesssim 0.5$ and $2.5 \lesssim z \lesssim 3$. Since the galaxy flow goes both ways, the effect of this aliasing ought to cancel out somewhat in statistical measures like the median. In addition we recall that the Final RLF method effectively reduces the redshift aliasing in the measured $N(z)$, using the bulk redshift information of the galaxy sample. Nevertheless we conservatively adopt as our best–estimate systematic error the full contribution of each catastrophic fraction (i.e. from shifting galaxies from $z \sim 0$ to $z \sim 3$ and vice versa). The CFDF–PRS I_{AB} and R_{AB} median redshifts, along with all of the error estimates are listed in Tables 6.1 and 6.2, respectively.

We also provide in these Tables median redshifts in differential (half) magnitude bins. Given these results, simple apparent magnitudes cuts in future imaging surveys can be used as proxies for photometric redshift information in tomographic weak lensing studies.

The complete error on each median redshift consists of the random error (a quadrature sum of the bootstrap and field–to–field errors) as well as the best estimate of the asymmetric systematic errors. For the $18.5 \leq I_{\mathrm{AB}} \leq 23.5$ sample the median redshift is therefore $\langle z \rangle = 0.71 \pm 0.040$ (random) $^{+0.01}_{-0.06}$ (systematic), where we use angle brackets to denote the median. We include median redshifts for the $24.0 \leq I_{\mathrm{AB}} \leq 24.5$ and $24.5 \leq R_{\mathrm{AB}} \leq 25.0$ samples which are formally outside our trusted magnitude range for accurate photometric redshifts, as can be seen by the sudden rise in the systematic error for these samples. Nevertheless, as the median is a reasonably robust statistic and of significant value to weak lensing studies, we tentatively include these two medians for use until deeper photometric redshift surveys become available.

An important point to realize in interpreting Tables 6.1 and 6.2 is that the errors on the medians would persist in an ideal spectroscopic survey. The random error estimates are not specific to the photometric redshift method and would be unchanged for a similar spectroscopic sample. However, the spectroscopic redshift samples published to date do not approach the combination of field size, area and depth of the present survey, and have therefore been more affected by cosmic variance. The best–estimate systematic errors would remain non–zero for the faintest magnitude limits in a spectroscopic survey, as single line redshift identifications are inherently problematic and lead to catastrophic failures for as many as $\sim 10\%$

of the galaxies (e.g. see Fernández–Soto et al. 2001). An additional systematic uncertainty, unique to spectroscopic surveys and quite difficult to estimate, is how spectroscopic incompleteness, most severe for galaxies with weak or absent emission lines, affects the measured $N(z)$.

As is clear from the Table, the field–to–field variance dominates the error budget in all cumulative (and most differential) magnitude ranges, and as such, the accuracy of the median redshifts in the CFDF–PRS is no worse than we had undertaken a more costly spectroscopic survey. In fact, for the reasons mentioned above it may be superior.

6.6   Comparison to COMBO–17 and HDF Median Redshifts

In Figure 6.3 we compare our R–band median redshifts to those of the COMBO–17 (Brown et al. 2003) photometric redshift survey and the Cohen et al. (2000) spectroscopic survey of the HDF North. The median redshifts are plotted versus median R_{AB} magnitudes which we have tabulated alongside the various sample magnitude ranges in Table 6.2.

Although our bright limit of $R_{\mathrm{AB}} > 18.5$, coupled with the relatively larger effect of cosmic variance at bright magnitudes makes a direct comparison non–trivial at $R_{\mathrm{AB}} \lesssim 20.5$ our results agree fairly well with, and are in fact intermediate between, these two other surveys. At fainter magnitudes these effects are minimized and the comparison becomes more straightforward. The agreement with both the COMBO–17 and Cohen et al. (2000) surveys is excellent for all $R_{\mathrm{AB}} \gtrsim 21$ within the quoted errors, which for the CFDF–PRS consist of the quadrature sum of the Poisson and field–to–field error terms. To be clear, the Cohen et al. (2000) errors are actually the 1st and 3rd quartile limits of the spectroscopic redshift distribution in each magnitude bin. While we agree with the Cohen et al. (2000) median redshifts within these conservatively large error limits, our fields clearly show a lower median redshift at faint magnitudes, quite in line with the COMBO–17 results. In fact, given the strong agreement our results suggest that for ensemble statistical measurements of the galaxy population it is perhaps advantageous to employ only ~ 6 broad–band filters (with spectral coverage from U through Z bands) and image more deeply rather than adopt a brighter medium band approach with ~ 15 filters. While the photometric redshift error on individual galaxies is likely lower with the medium band survey strategy, broad–band photometric redshift surveys like the CFDF–PRS probe deeper down the luminosity function with little penalty on statistical measurements.

Table 6.1. I_{AB} Median Redshifts in the CFDF–PRS

Mag Range	$\langle I_{AB} \rangle$	$\langle z \rangle$	Random Errors		Potential Systematic Effects due to Redshift Aliasing			
			$1-\sigma$ Bootstrap	$1-\sigma$ Field–to–Field	Δ_{best} $(z=3 \to 0)$	Δ_{best} $(z=0 \to 3)$	Δ_{max} $(z \leq 1.3)$	Δ_{max} $(z \geq 0.2)$
$18.5 \leq I_{AB} \leq 20.5$	19.88	0.38	0.006	0.035	-0.00	0.00	-0.01	0.02
$18.5 \leq I_{AB} \leq 21.0$	20.36	0.43	0.006	0.065	-0.00	0.01	-0.01	0.03
$18.5 \leq I_{AB} \leq 21.5$	20.79	0.49	0.007	0.075	-0.00	0.01	-0.02	0.02
$18.5 \leq I_{AB} \leq 22.0$	21.23	0.54	0.006	0.070	-0.00	0.01	-0.01	0.02
$18.5 \leq I_{AB} \leq 22.5$	21.68	0.59	0.004	0.055	-0.00	0.01	-0.02	0.02
$18.5 \leq I_{AB} \leq 23.0$	22.11	0.64	0.004	0.031	-0.00	0.01	-0.03	0.02
$18.5 \leq I_{AB} \leq 23.5$	22.59	0.71	0.005	0.040	-0.01	0.01	-0.06	0.01
$18.5 \leq I_{AB} \leq 24.0$	23.11	0.77	0.005	0.049	-0.01	0.02	-0.09	0.02
$18.5 \leq I_{AB} \leq 19.0$	18.76	0.30	0.010	0.023	-0.00	0.01	-0.01	0.03
$19.0 \leq I_{AB} \leq 19.5$	19.27	0.32	0.008	0.010	-0.00	0.00	-0.01	0.02
$19.5 \leq I_{AB} \leq 20.0$	19.79	0.39	0.011	0.023	-0.00	0.01	-0.01	0.02
$20.0 \leq I_{AB} \leq 20.5$	20.28	0.43	0.011	0.085	-0.00	0.01	-0.01	0.03
$20.5 \leq I_{AB} \leq 21.0$	20.79	0.52	0.010	0.072	-0.00	0.00	-0.01	0.02
$21.0 \leq I_{AB} \leq 21.5$	21.28	0.58	0.007	0.050	-0.00	0.01	-0.01	0.01
$21.5 \leq I_{AB} \leq 22.0$	21.78	0.63	0.007	0.040	-0.00	0.01	-0.02	0.01
$22.0 \leq I_{AB} \leq 22.5$	22.27	0.71	0.006	0.036	-0.01	0.00	-0.03	0.01
$22.5 \leq I_{AB} \leq 23.0$	22.77	0.78	0.007	0.031	-0.00	0.01	-0.06	0.02
$23.0 \leq I_{AB} \leq 23.5$	23.27	0.89	0.007	0.031	-0.01	0.01	-0.11	0.02
$23.5 \leq I_{AB} \leq 24.0$	23.78	1.03	0.008	0.061	-0.04	0.02	-0.23	0.03
$24.0 \leq I_{AB} \leq 24.5$[1]	24.27	1.26	0.010	0.083	-0.13	0.04	-0.47	0.06

[1]This is formally outside the range trusted for accurate photometric redshifts (see text).

Note. — The best estimates of the upper and lower systematic errors (Δ_{best}) are computed using the catastrophic fraction as a function of magnitude from Figure 4.4. Errors of ± 0.00 are smaller than the photometric redshift resolution of 0.01.

6.7 Representations of the CFDF–PRS Redshift Distributions

In this Section we present our redshift distributions binned in magnitude and redshift, as well as in parametrized form in various magnitude ranges. It should be well noted that none of the main qualitative results of this Chapter change if simple maximum likelihood redshift (Peak–ML) values are used in place of the Final RLF described in Chapter 5. Although we have demonstrated that the iterated method produces optimal results, the slight differences in quantitative results are negligible compared to the field–to–field variance.

6.7.1 Binned Redshift Distributions

In Tables 6.3 and 6.4 we present the measured CFDF–PRS redshift distributions, digitized so as to present trustworthy information over all redshifts. Specifically, we present the Final RLF $N(z)$ in redshift bins of $\Delta z = 0.1$ for $z < 1.3$ and much more broadly ($\Delta z = 1.0$) at high redshift where the photometric redshifts are not as accurate. Our distributions are presented in half–magnitude bins, which should enable other workers to construct redshift distributions for any sample in the range $18.5 \leq I_{AB} \leq 24$, with the obvious caveat that bright samples containing small numbers of objects have relatively larger uncertainties than deeper samples.

As an example, in Figure 6.4 we plot the binned distributions (filled symbols) for the CFRS depth of $18.5 \leq I_{AB} \leq 22.5$ and the full CFDF–PRS depth of $18.5 \leq I_{AB} \leq 24$ along with the full distributions (thin solid curves). The binned distributions accurately represent the data at all redshifts, although they are highly smoothed at $z > 1.25$. As such our distributions should be used in this form for precision (e. g. cosmic shear) measurements. For convenience we also provide parametrized fits to our distributions in the next Section.

6.7.2 Parametrizations of $N(z)$

Analytic fits of the form (Pen et al. 2003, Van Waerbeke et al. 2001)

$$N(z) = N_0 \frac{\beta}{z_0 \, \Gamma\left(\frac{1+\alpha}{\beta}\right)} \left(\frac{z}{z_0}\right)^{\alpha} \exp\left[-\left(\frac{z}{z_0}\right)^{\beta}\right] \tag{6.1}$$

were applied to our I_{AB} and R_{AB} redshift distributions in various magnitude ranges and the results are listed in Tables 6.5 and 6.6, respectively. We limit our fits to the redshift region $0.375 \leq z \leq 1.3$, i. e. we exclude the $z \sim 0.3$ overdensity and fit the main single peak in each magnitude range.

Our fitting technique consists of minimizing the Kolmogorov–Smirnov distance D between the cumulative distribution functions of the model and Final RLF method redshift distributions over the allowed redshift range. The full three parameter fits $[z_0, \alpha, \beta]$ have α values very close to the commonly used

Table 6.3.   Binned I_{AB} CFDF–PRS Redshift Distributions

		$\langle I_{AB} \rangle_{\Delta m = 0.5}$										
$z_l - z_h$	z	18.75	19.25	19.75	20.25	20.75	21.25	21.75	22.25	22.75	23.25	23.75
$0.05 - 0.15$	0.10	157	161	140	266	313	284	343	419	636	928	1703
$0.15 - 0.25$	0.20	320	390	362	533	726	750	956	1163	1395	1648	2594
$0.25 - 0.35$	0.30	638	905	869	1098	1316	1485	1702	2112	2080	2375	3058
$0.35 - 0.45$	0.40	281	547	921	1179	1404	1557	2007	2147	2207	2608	3255
$0.45 - 0.55$	0.50	79	181	638	1042	1718	1885	2787	2657	2961	3224	4384
$0.55 - 0.65$	0.60	48	78	387	968	2024	2665	3551	3735	4136	4544	5453
$0.65 - 0.75$	0.70	27	29	153	401	1229	2142	3355	4519	5260	6073	6573
$0.75 - 0.85$	0.80	10	10	44	162	562	1419	2743	4264	5526	7029	7506
$0.85 - 0.95$	0.90	3	6	20	75	238	771	1617	2967	4436	6511	7402
$0.95 - 1.05$	1.00	1	3	9	22	66	224	659	1506	2728	4899	6616
$1.05 - 1.15$	1.10	1	2	4	7	19	62	237	670	1448	2999	4870
$1.15 - 1.25$	1.20	0	1	3	5	10	32	125	377	990	2119	3764
$1.25 - 2.25$	1.75	0	1	2	2	5	16	62	199	512	1183	2373
$1.75 - 2.75$	2.25	6	4	5	8	8	11	40	85	204	507	1188
$2.25 - 3.25$	2.75	18	7	9	15	21	19	47	70	132	292	645
$2.75 - 3.75$	3.25	14	3	5	8	13	10	16	24	48	116	289
$3.25 - 4.25$	3.75	1	0	0	1	0	2	0	0	3	10	51
$3.75 - 4.75$	4.25	0	0	0	0	0	3	0	0	1	6	25

Note. — The redshift distributions are presented in constant 0.5 magnitude bins between $18.5 \leq I_{AB} \leq 24$, whereas the $\Delta z = 0.1$ bin size in redshift is expanded to overlapping $\Delta z = 1.0$ bins at $z > 1.25$. In each redshift bin the number of galaxies in the $\Delta m = 0.5$ magnitude range is computed as $N = \int_{z_l}^{z_h} N(z, m_l \leq I_{AB} \leq m_h) \, dz / \int_{z_l}^{z_h} dz$, where $m_l = \langle I_{AB} \rangle - 0.25$, $m_h = \langle I_{AB} \rangle + 0.25$, and the number densities, N, represent the CFDF–PRS survey area of 0.4514 deg^2.

Table 6.4.   Binned R_{AB} CFDF–PRS Redshift Distributions

$z_l - z_h$	z	$\langle R_{\mathrm{AB}} \rangle_{\Delta m = 0.5}$											
		18.75	19.25	19.75	20.25	20.75	21.25	21.75	22.25	22.75	23.25	23.75	24.25
$0.05 - 0.15$	0.10	128	150	183	168	318	279	306	408	429	743	1051	1956
$0.15 - 0.25$	0.20	230	303	432	443	642	782	794	1171	1125	1499	1722	2780
$0.25 - 0.35$	0.30	488	706	850	1017	1243	1553	1648	2088	2004	2279	2475	3240
$0.35 - 0.45$	0.40	340	410	605	929	1244	1658	1913	2239	2224	2571	2790	3410
$0.45 - 0.55$	0.50	92	144	222	630	1016	1802	2240	3031	3096	3109	3326	4204
$0.55 - 0.65$	0.60	43	93	114	302	650	1587	2755	3632	4382	4292	4591	5037
$0.65 - 0.75$	0.70	11	32	40	63	211	558	1615	2618	4373	5370	5893	6135
$0.75 - 0.85$	0.80	2	8	9	13	43	97	502	1339	2882	4900	6216	7061
$0.85 - 0.95$	0.90	1	3	3	3	14	22	133	575	1624	3232	5092	6597
$0.95 - 1.05$	1.00	0	2	1	2	8	5	40	208	698	1764	3377	5318
$1.05 - 1.15$	1.10	0	1	0	2	4	1	17	80	312	874	2077	3737
$1.15 - 1.25$	1.20	0	1	0	2	2	1	9	41	162	537	1496	2955
$1.25 - 2.25$	1.75	0	0	1	1	1	1	9	27	101	384	1031	2154
$1.75 - 2.75$	2.25	7	3	6	7	8	8	19	41	84	229	565	1240
$2.25 - 3.25$	2.75	20	8	10	13	20	16	27	45	68	139	297	696
$2.75 - 3.75$	3.25	14	7	5	7	12	9	12	15	27	44	126	341
$3.25 - 4.25$	3.75	1	1	0	1	0	0	1	1	2	2	23	77
$3.75 - 4.75$	4.25	0	0	0	0	0	0	2	1	0	0	3	15

Note. — All quantities are as in defined in Table 6.3, with the addition of the distribution for the $24.0 < R_{\mathrm{AB}} < 24.5$ bin in the final column.

Table 6.5.   Parametrized Fits of I_{AB} CFDF–PRS Redshift Distributions

Mag Range	$z \lesssim 1.2$						$z \gtrsim 1.2$		
	N_0		z_0		β		A_T	z_T	γ
$18.5 \leq I_{AB} \leq 24.0$	20785	(133)	0.790	(0.008)	2.788	(0.059)	11443	1.786	2.037
$19.0 \leq I_{AB} \leq 24.0$	20735	(141)	0.793	(0.009)	2.805	(0.067)	11472	1.783	2.039
$19.5 \leq I_{AB} \leq 24.0$	20625	(143)	0.800	(0.008)	2.852	(0.058)	11503	1.780	2.037
$20.0 \leq I_{AB} \leq 24.0$	20310	(135)	0.818	(0.009)	2.969	(0.074)	11557	1.776	2.033
$20.5 \leq I_{AB} \leq 24.0$	19800	(126)	0.840	(0.008)	3.123	(0.073)	11609	1.773	2.032
$21.0 \leq I_{AB} \leq 24.0$	18861	(141)	0.872	(0.007)	3.341	(0.074)	11695	1.770	2.031
$21.5 \leq I_{AB} \leq 24.0$	17569	(128)	0.902	(0.007)	3.529	(0.093)	11635	1.782	2.053
$22.0 \leq I_{AB} \leq 24.0$	15573	(120)	0.945	(0.008)	3.817	(0.121)	11672	1.776	2.043
$22.5 \leq I_{AB} \leq 24.0$	13046	(111)	0.978	(0.009)	3.904	(0.135)	11131	1.788	2.045
$23.0 \leq I_{AB} \leq 24.0$	9829	(90)	1.015	(0.008)	3.992	(0.122)	9383	1.837	2.074
$18.5 \leq I_{AB} \leq 21.5$	3216	(169)	0.609	(0.010)	3.200	(0.096)	44	3.717	93.92
$18.5 \leq I_{AB} \leq 22.0$	5205	(165)	0.644	(0.008)	3.175	(0.075)	109	3.460	14.55
$18.5 \leq I_{AB} \leq 22.5$	7759	(186)	0.683	(0.009)	3.119	(0.068)	658	2.084	2.327
$18.5 \leq I_{AB} \leq 23.0$	10979	(168)	0.720	(0.008)	3.048	(0.067)	2422	1.716	1.994
$18.5 \leq I_{AB} \leq 23.5$	15293	(157)	0.760	(0.008)	2.941	(0.066)	5889	1.699	2.013
$18.5 \leq I_{AB} \leq 24.0$	20785	(133)	0.790	(0.008)	2.788	(0.059)	11443	1.786	2.037

Note. — The fits are for the CFDF–PRS survey area of 0.4514 deg^2. At $z \lesssim 1.2$ the best–fitting parameters of Equation 6.1 are listed, along with bootstrap–resampled errors. At $z \gtrsim 1.2$, the parameters of fits of the form of Equation 6.2 are tabulated. We conservatively estimate the error in the high redshift tail to be 50%.

value of 2.0, expected on geometric arguments for a flat average luminosity function. Without significantly compromising the accuracy of the fits, we therefore reduce the dimensionality of the analysis by setting $\alpha \equiv 2.0$. The 1–σ single parameter errors in z_0 and β, listed in the Tables, are estimated via 100 bootstrap resamplings (with repetitions) of the CFDF–PRS catalog, and subsequent recalculation of the redshift distributions using the Full–RLF method. The separately determined absolute number densities, N_0, along with bootstrap resampled errors are also listed in the Tables.

We found Equation 6.1 to be a sensible model for $N(z)$ up to the CFRS depth ($I_{AB} \sim 22.5$), but at fainter magnitudes it fails to simultaneously model the main $z \lesssim 1$ peak and the increasing high redshift tail (at $I_{AB} \lesssim 24$ the fraction of $z > 1$ galaxies is approximately 30%). We therefore limit its application

Table 6.6.   Parametrized Fits of $R_{\rm AB}$ CFDF–PRS Redshift Distributions

Mag Range	$z \lesssim 1.2$						$z \gtrsim 1.2$		
	N_0		z_0		β		A_T	z_T	γ
$18.5 \leq R_{\rm AB} \leq 24.0$	13446	(133)	0.662	(0.012)	2.601	(0.081)	2380	2.433	3.083
$19.0 \leq R_{\rm AB} \leq 24.0$	13379	(121)	0.667	(0.011)	2.629	(0.073)	2415	2.407	3.034
$19.5 \leq R_{\rm AB} \leq 24.0$	13288	(113)	0.673	(0.010)	2.659	(0.065)	2425	2.399	3.025
$20.0 \leq R_{\rm AB} \leq 24.0$	13151	(113)	0.681	(0.012)	2.710	(0.081)	2447	2.384	2.999
$20.5 \leq R_{\rm AB} \leq 24.0$	12859	(110)	0.701	(0.010)	2.837	(0.077)	2471	2.367	2.969
$21.0 \leq R_{\rm AB} \leq 24.0$	12429	(122)	0.725	(0.010)	2.993	(0.087)	2507	2.343	2.927
$21.5 \leq R_{\rm AB} \leq 24.0$	11659	(100)	0.761	(0.009)	3.232	(0.091)	2549	2.325	2.895
$22.0 \leq R_{\rm AB} \leq 24.0$	10532	(113)	0.796	(0.010)	3.434	(0.115)	2591	2.302	2.881
$22.5 \leq R_{\rm AB} \leq 24.0$	8896	(96)	0.848	(0.008)	3.812	(0.122)	2624	2.266	2.839
$23.0 \leq R_{\rm AB} \leq 24.0$	6661	(78)	0.894	(0.010)	4.036	(0.153)	2532	2.228	2.770
$18.5 \leq R_{\rm AB} \leq 22.0$	2992	(170)	0.538	(0.011)	3.140	(0.111)	28	3.716	76.46
$18.5 \leq R_{\rm AB} \leq 22.5$	4607	(150)	0.567	(0.010)	3.116	(0.084)	70	3.670	45.30
$18.5 \leq R_{\rm AB} \leq 23.0$	6800	(150)	0.602	(0.011)	3.007	(0.083)	186	3.432	13.82
$18.5 \leq R_{\rm AB} \leq 23.5$	9632	(145)	0.634	(0.013)	2.825	(0.098)	612	2.982	5.643
$18.5 \leq R_{\rm AB} \leq 24.0$	13446	(133)	0.662	(0.012)	2.601	(0.081)	2380	2.433	3.083
$18.5 \leq R_{\rm AB} \leq 24.5$	18656	(146)	0.665	(0.012)	2.309	(0.060)	5930	2.337	2.778

Note. — All quantities are defined as in Table 6.5. For the $R_{\rm AB}$ sample we also provide a fit for the $18.5 \leq R_{\rm AB} \leq 24.5$ magnitude range.

to the $z \lesssim 1.2$ regime and fit the $z \gtrsim 1.2$ tail of the distribution with a decaying exponential,

$$N(z) = A_T \exp\left[-\left(\frac{z}{z_T} \right)^\gamma \right]. \tag{6.2}$$

Note that this equation is not fitted to the the Final RLF $N(z)$ but rather to the binned distributions calculated from Tables 6.3 and 6.4. The transition between Equations 6.1 and 6.2 is always very close to $z \approx 1.2$, but to produce a continuous parametrization should in general be taken to be the redshift at which the two parametrizations intersect.

For the high redshift tail the dominant errors are likely systematic in nature, coming from the photometric redshift algorithm operating in a redshift and magnitude regime where the convergence properties are highly uncertain. Without a large, deep spectroscopic comparison sample at $1 < z < 3$ it is difficult to assess these errors in a meaningful way. In the present work we conservatively assign a maximum uncertainty of 50% to the fit in the $z \gtrsim 1.3$ regime. Examples of the fits are shown in Figure 6.4 for the $18.5 \leq I_{\rm AB} \leq 22.5$ and $18.5 \leq I_{\rm AB} \leq 24$ samples. The solid, thick blue curve is the best

fitting parametrization of the form of Equation 6.1 within the $0.375 \leq z \leq 1.3$ fitting region, although it is very likely correct at $z < 0.375$ (dotted curve) due to the constraint at $z = 0$. At $z \gtrsim 1.2$ the best–fit parametrization of the form of Equation 6.2 is represented by the long–dashed red curve. Taken together the full redshift range is well parametrized by these functions.

6.8   Future Measurements of $N(z)$

In light of the preceding discussion, it is evident that in the redshift regimes in which multicolor imaging surveys have appropriate wavelength coverage and depth, the errors in photometric redshifts (conservatively $\Delta z \sim 0.1$) are not the limiting factor in an accurate determination of $N(z)$. In addition, we have verified that the systematic errors inherent in the method are secondary to cosmic variance in the overall error budget.

The effect of cosmic variance similarly dominates the error budget of current and planned non–local spectroscopic surveys, at a level consistent with the present survey. This is due to the large contiguous field requirement of clustering analyses, among the primary goals in such surveys, which precludes the targeting of sufficient numbers of independent fields. An "optimal" spectroscopic survey strategy, of little use for studies of galaxy correlations, would contain many ($N \sim 50 - 100$) deep, sparsely sampled fields to reduce the cosmic variance to the level of the systematic errors.

We believe this analysis clearly shows that multicolor photometric redshift surveys are equally capable of producing accurate measurements of $N(z)$, with three important advantages. The first is the lack of spectroscopic incompleteness, and hence no bias against objects with low star formation rates. Second, in an "optimal" survey with N fields, each multi–color imaging field, acquired at the same observational cost as a deep spectroscopic pointing, can have a field size of order $1° \times 1°$ with modern mosaic CCDs (e.g. Megacam). In addition to generating catalogues of $\sim 10^5$ galaxies to $I_{AB} \sim 25$, this large field size produces a smaller cosmic variance *per field* as compared with a similar spectroscopic pointing. Finally, on a practical note, it is feasible from a cost perspective to obtain deep, multicolor imaging of a large contiguous area of sky several degrees on a side. Such a strategy allows many scientific analyses to be performed on a common data set, from 3–D clustering (using photometric redshifts) to weak lensing shear measurements, while producing a large number of effectively independent fields for the $N(z)$ measurement. Subfields separated by $\gtrsim 1° - 2°$ ($\gtrsim 50 - 100$ Mpc at $z = 0.75$) are virtually uncorrelated (in the sense that the correlation function vanishes) and hence for an $N \times N$ deg^2 box tiled with $1° \times 1°$ pointings, roughly $N^2/3$ to $N^2/2$ pointings can be considered effectively independent.

The Wide Synoptic component of the ongoing CFHT Legacy Survey (CFHTLS) has such a survey

geometry. Their filter set (wide $u*$ plus SDSS $g'r'i'z'$) will allow reliable photometric redshifts in a range similar to that in the present study, i. e. $z \lesssim 1.3$. It consists of three fields, one $8° \times 9°$ and two $7° \times 7°$, allowing ~ 100 quasi–independent samples of the galaxy distribution. In addition, these fields provide width to depth ratios of order $\sim 15\%$, improving on the CFDF–PRS by roughly the same factor that we improve on the HDF studies, and allowing a reliable measurement of power on ~ 500 Mpc scales at $z \sim 1$. As such it will make the definitive measurement of $N(z)$ for $z \lesssim 1.3$ to AB ~ 24.

Extending the CFHTLS $N(z)$ measurement to $z > 1.3$ will require wide field infrared imaging, either from the ground with large field mosaic cameras (with degree field sizes), or from space where the absence of an overwhelming sky background allows efficient mapping with relatively small detectors (e.g. SIRTF).
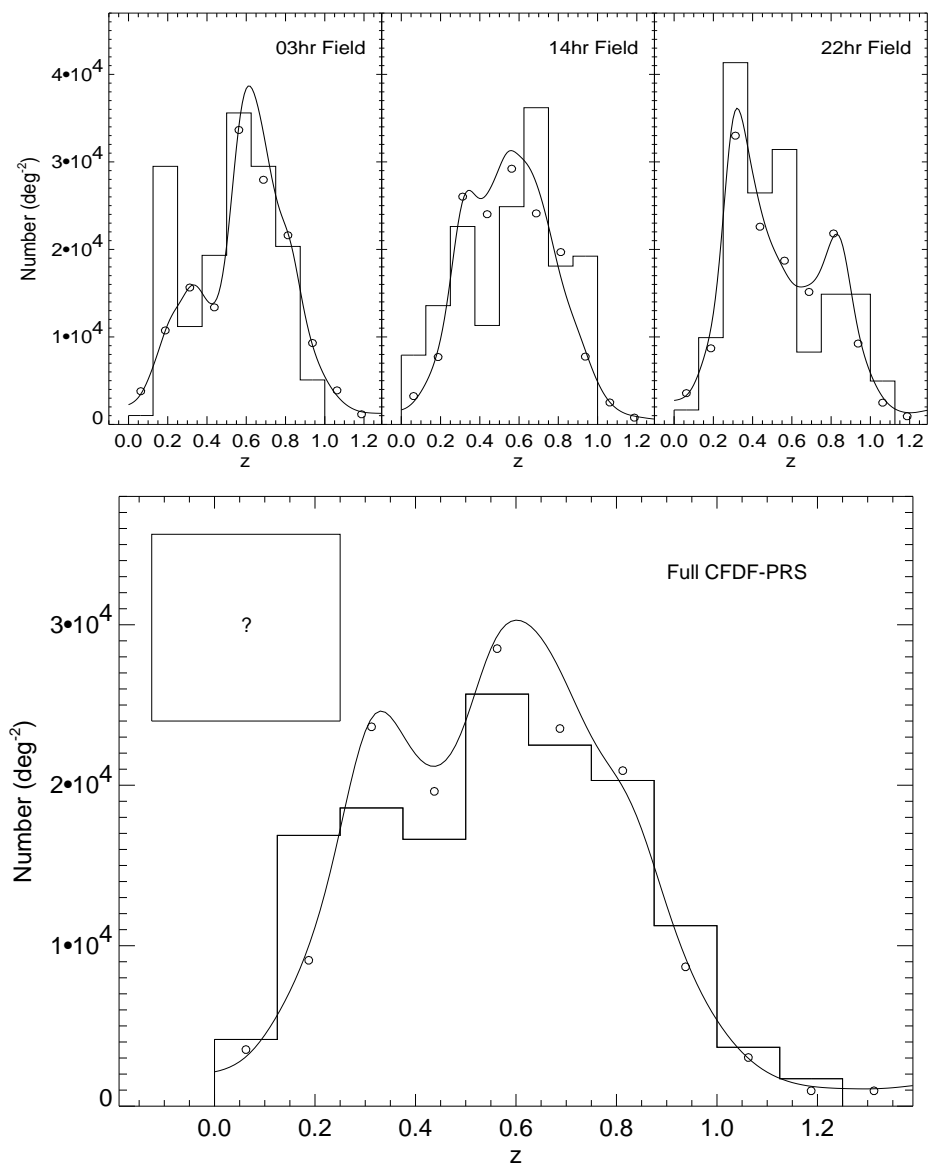
Figure 6.1 CFDF–PRS and CFRS redshift distributions over the common magnitude range $18.5 \leq I_{AB} \leq 22.5$. The curves are the Full–RLF final iteration, the points represent the Peak–ML distributions, and the histograms are from the CFRS. In the individual fields the CFRS number densities are scaled to the CFDF values, whereas in the combined fields we plot the CFRS distribution using their original normalization. The fraction of unidentified CFRS objects is represented by the box to the left of the peak. Stars have been removed from both samples.
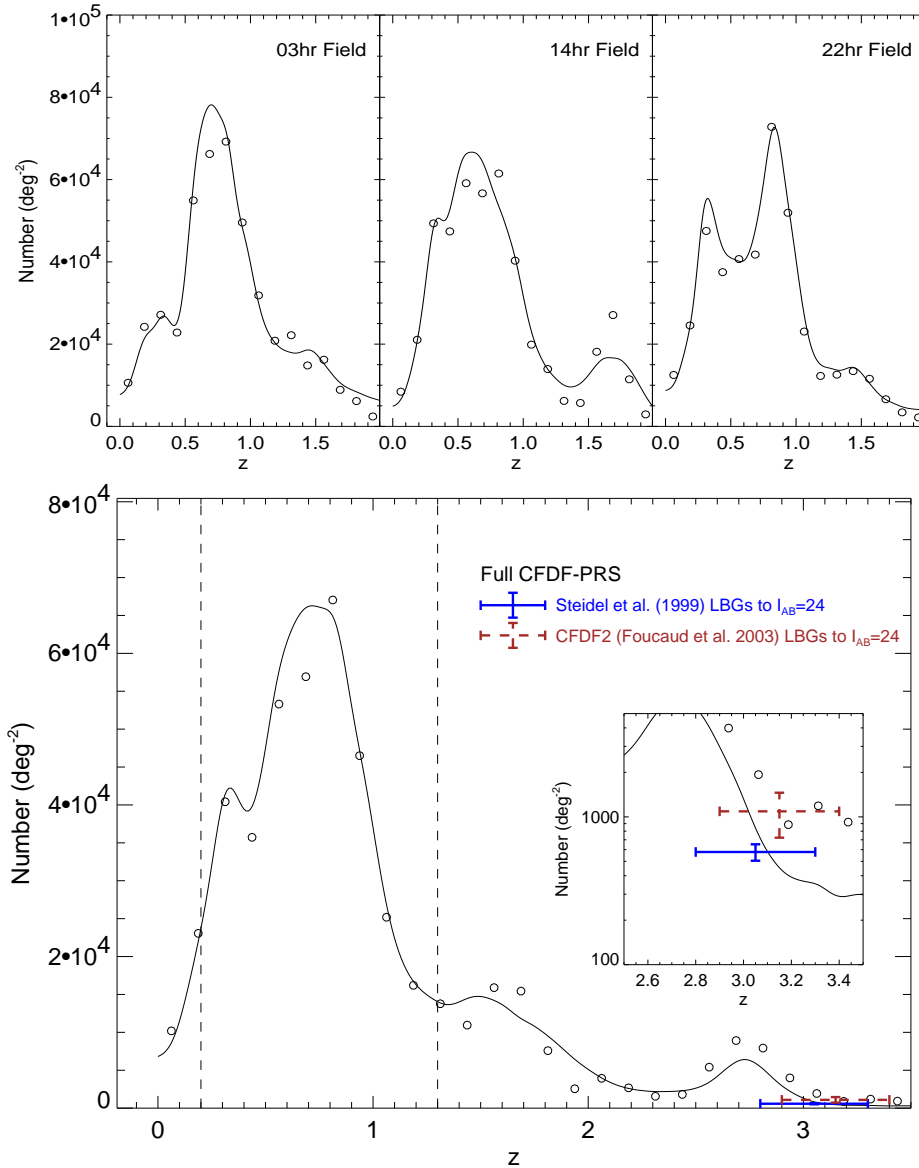
Figure 6.2 CFDF–PRS redshift distribution over magnitude range $18.5 \leq I_{AB} \leq 24.0$. The solid curve and empty circles represent the Final RLF and Peak–ML redshift distributions, respectively. Also plotted are the Steidel et al. (1999) and Foucaud et al. (2003) LBG counts (dashed error bar) integrated to $I_{AB} = 24$ for comparison. The horizontal error bars represent the redshift sensitivity ranges of the respective LBG samples, whereas the vertical error bars show the 1–σ errors in the integrated counts.
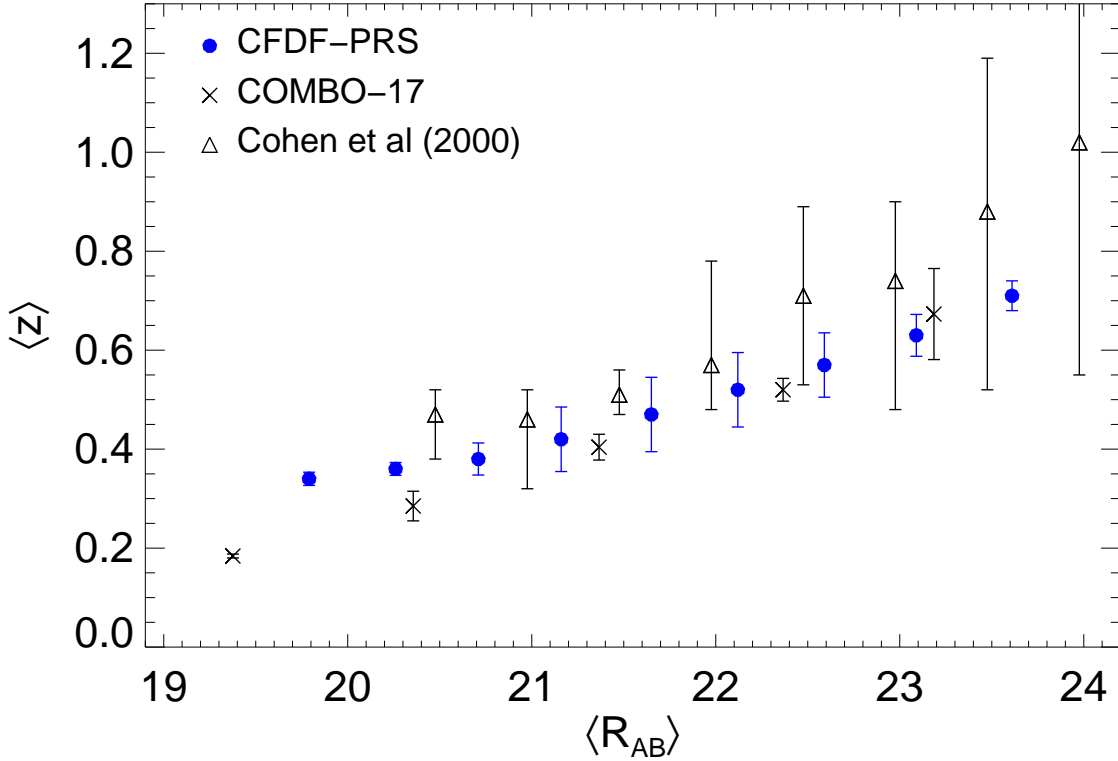
Figure 6.3 Median redshift vs. median R_{AB} magnitude in the CFDF–PRS (filled symbols). We have also plotted the results for the COMBO–17 survey (Brown et al. 2003) and the HDF North spectroscopic redshift survey of Cohen et al. (2000), both adjusted to AB magnitudes.
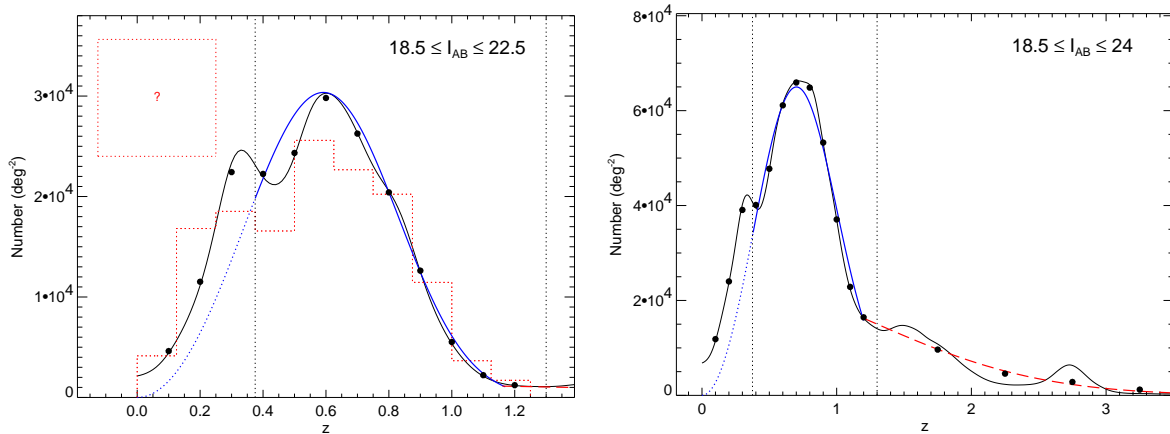
Figure 6.4 Binned distributions (solid symbols) and best–fit parametrizations plotted along with the $18.5 \leq I_{AB} \leq 22.5$ and $18.5 \leq I_{AB} \leq 24$ RLF redshift distributions (thin solid curves), scaled to 1 square degree. The solid, thick blue curve shows the best fitting parametrization of the main peak (Equation 6.1) at $z \lesssim 1.2$ (represented as a dotted curve outside the fitting range, i. e. at $z < 0.375$). At $z \gtrsim 1.2$ the red long–dashed curve is the best fitting model of the high redshift tail (Equation 6.2). The CFRS histogram is included for reference as the (dotted) histogram, with the number of unidentified CFRS objects once again represented by the box to the left of the peak.

Chapter 7

Application of Photometric
Redshifts: Clustering Evolution

Having fully developed the photometric redshift method in the preceding Chapters, we employ them in the present Chapter to make a measurement of the redshift evolution of the galaxy correlation function. Traditionally the domain of spectroscopic redshift surveys, we demonstrate that this important topic can be equally addressed using photometric redshifts. We conclude that the next generation of wide–field, deep imaging surveys covering hundreds of square degrees should employ similar methods to fully extract the science from their surveys.

7.1   Introduction

In our quest to understand the evolution of large scale structure in the Universe, much research has gone into characterizing the clustering properties of the galaxy population. While the physical quantity of interest is the power spectrum of density fluctuations, its Fourier transform, the two–point correlation function, has proved to be one of the most useful of galaxy properties due to both the ease with which it can be measured and its direct connection to theories of structure formation.

Defined implicitly by the equation

$$\delta P = \bar{n}^2 \, \delta V_1 \delta V_2 [1 + \xi(r_{12})], \qquad (7.1)$$

where $\bar{n} \equiv \langle N \rangle / V$ is the mean density of the galaxy population, the correlation function, $\xi(r_{12})$, is the probability in *excess* of random (assuming a uniform Poisson point process) of jointly finding two galaxies in two volume shells, δV_1 and δV_2 at a separation r_{12}. Equation 7.1 can be recast in terms of

the conditional probability of finding a galaxy in a volume shell δV_2, given that there is a galaxy in δV_1 at a separation r_{12}

$$\delta P(2|1) = \bar{n}\,\delta V_2[1 + \xi(r_{12})]. \tag{7.2}$$

This can be generalized such that for any random galaxy in the sample, the probability of finding another galaxy at a separation r can be written as

$$\delta P = \bar{n}\,\delta V[1 + \xi(r)]. \tag{7.3}$$

The correlation function is well–parametrized as a simple power–law, $\xi(r) = (r/r_0)^{-\gamma}$, over a large range of separations (at least $0.05 \lesssim r(h^{-1}\ \mathrm{Mpc}) \lesssim 10$).

Traditionally, spectroscopic redshift surveys were required to measure the redshift evolution of the galaxy correlation function, whereas imaging surveys, absent redshift information, were limited to measurements of the angular correlation function (ACF). On the plane of the sky the angular analogue of Equation 7.3 is

$$\delta P = \bar{n}\,\delta\Omega[1 + \omega(\theta)]. \tag{7.4}$$

where the angular correlation function, $\omega(\theta)$, is equally well parametrized as a power law

$$\omega(\theta) = A_\omega \theta^{-\delta}. \tag{7.5}$$

Limber (1954) demonstrated how the ACF can be deprojected to yield a measurement of the real–space correlation length, $r_0(z)$, over the redshift range spanned by the 2–D image. The relativistic version of the Limber equation

$$\omega(\theta) = \frac{H_0 H_\gamma}{c}\,\theta^{1-\gamma}\,\frac{\int_0^\infty N^2(z)\,r_0^\gamma(z)\,[x(z)]^{1-\gamma}\,E(z)\,F(z)\,dz}{[\int_0^\infty N(z)\,dz]^2} \tag{7.6}$$

is derived in Appendix D for the spatially flat cosmologies we consider in this work, for which the curvature correction, $F(z)$, has a value of unity. Here $H_\gamma = \Gamma[1/2]\,\Gamma[(\gamma-1)/2]/\Gamma[\gamma/2]$ ($H_\gamma \approx 3.68$ for $\gamma = 1.8$), $N(z)$ is the redshift distribution of the galaxies in the sample, $x(z)$ is the cosmology–dependent comoving radial distance

$$x(z) = \frac{c}{H_0}\int_0^z \frac{dz}{E(z)}, \tag{7.7}$$

and $E(z)$ is proportional to the time derivative of the logarithm of the scale factor (e.g. Peebles 1993, Hogg 1999)

$$\frac{\dot{a}}{a} = H_0\,E(z) = H_0\sqrt{\Omega_M(1+z)^3 + \Omega_k(1+z)^2 + \Omega_\Lambda}, \tag{7.8}$$

where $\Omega_M + \Omega_k + \Omega_\Lambda = 1$. From Equations 7.5 and 7.6 we see that the slope of the ACF is one power less than that of the full 3–D correlation function, and we can associate $\delta = \gamma - 1$.

The photometric redshift technique allows us to adopt an intermediate approach. We divide the full galaxy sample into redshift bins and measure the ACF in each bin. Using the redshift distributions measured in Chapter 6, we can accurately deproject our ACFs to determine the redshift evolution of the real–space comoving correlation length. Taking r_0^γ to be approximately constant across a redshift bin $z_1 \leq z < z_2$ and parametrizing $\omega(\theta) = A_\omega \theta^{1-\gamma}$ we obtain

$$r_0^\gamma(z_{\text{eff}}) = A_\omega \left[\frac{H_0 H_\gamma}{c} \frac{\int_{z_1}^{z_2} N^2(z) \, [x(z)]^{1-\gamma} \, E(z) \, dz}{[\int_{z_1}^{z_2} N(z) \, dz]^2} \right]^{-1} \tag{7.9}$$

where

$$z_{\text{eff}} = \frac{\int_{z_1}^{z_2} z \, N^2(z) \, [x(z)]^{1-\gamma} \, E(z) \, dz}{\int_{z_1}^{z_2} N^2(z) \, [x(z)]^{1-\gamma} \, E(z) \, dz}. \tag{7.10}$$

7.2 Monte Carlo Integration

An analytic integration of Equation 7.4 over the survey area is not feasible due to the complicated masking of our fields. Instead we use established Monte Carlo techniques to estimate the ACF in our three survey fields. The method involves generating a large catalogue of points drawn from the same selection function as the data, except randomly distributed in space, counting the number of neighbours (in both the data and random catalogues) as a function of separation from a given galaxy, and then repeating and summing over all galaxies.

The simplest estimator (Davis and Peebles 1983),

$$\omega = \frac{N_r}{N_d} \frac{DD}{DR} - 1, \tag{7.11}$$

while adequate in the strong clustering regime ($\omega \gg 1$) is not particularly accurate in the $\omega < 1$ regime typical of galaxy correlations. Here DD and DR are the sum of ordered data–data and data–random pairs at each angular separation, and N_d and N_r are the total number of data and random galaxies, respectively.

Two more robust estimators are due to Landy and Szalay (1993)

$$\omega = \frac{N_r^2 DD - 2 N_r N_d DR + N_d^2 RR}{N_d^2 RR}, \tag{7.12}$$

and Hamilton (1993)

$$\omega = \frac{DD \times RR}{DR \times DR} - 1, \tag{7.13}$$

where the latter estimator is self–normalizing. Tests of these two estimators have shown they produce essentially identical results for all samples at all scales. These estimators include an auto–correlation of the random catalog (the RR term), and hence are much more computationally expensive.

In order to render the calculation feasible a sorted linked list algorithm was developed. This method takes advantage of the fact that an overwhelming number of pairs in the N^2 correlation process are at separations far larger than those to which the ACF can be usefully measured, and there is therefore no point in computing them. The input masked galaxy and random catalogs are first divided into a grid of 38×38 cells, where this grid size was chosen as a compromise between decreasing cell occupation number and increasing linked list overhead. Each galaxy is then correlated with all galaxies in its own cell, and in adjacent cells out to a maximum angular separation iteratively chosen to be between 1/3 and 1/2 of the field size, depending on the amplitude of the ACF. Beyond this scale both the Poisson errors and the integral constraint, described below, act to prevent a useful measurement of the ACF. The code was extensively tested and, while 3–5 times faster, we have verified that it produces results identical to the direct N^2 calculation for all separations up to the chosen cutoff scale.

7.3   Object Weights

In correlation analyses of spectroscopic redshift surveys it is necessary to apply weights to the pair counts in the Monte Carlo integration to account for the complicated selection function arising from slit or fiber collisions. Deep imaging surveys do not share this complication, having a uniform selection in all unmasked areas, at least on scales larger than roughly twice the seeing. Photometric completeness, crucially important in luminosity function measurements, is not required for accurate correlation measurements provided any incompleteness is uniform across the field. Regardless, each of our fields is essentially fully complete to $I_{\mathrm{AB}} = 24$ (c.f. Section §3.3).

There is, however, a weighting issue unique to photometric redshifts that we must account for. As described in detail in the preceding Chapters, the maximum likelihood (ML) photometric redshift values do not contain all the redshift information present in the data. The full redshift likelihood function (RLF), a probability function in redshift space, provides the most complete redshift information for each galaxy. This extra information must be incorporated into the clustering analysis in order to correctly incorporate the photometric redshift errors, which are, of course, substantially larger than in spectroscopic surveys.

An illustration of this is given in Figure 7.1, which plots the redshift likelihood functions of two galaxies with ML redshifts inside a redshift range $0.2 \leq z \leq 0.5$. A significant fraction of the redshift likelihood is outside this region for the galaxy at $z \sim 0.45$. Our clustering measurement should take into account the fact that the lower redshift galaxy is *more* likely to actually be in this range. Simply treating them equally will tend to artificially lower the clustering amplitude through projection effects
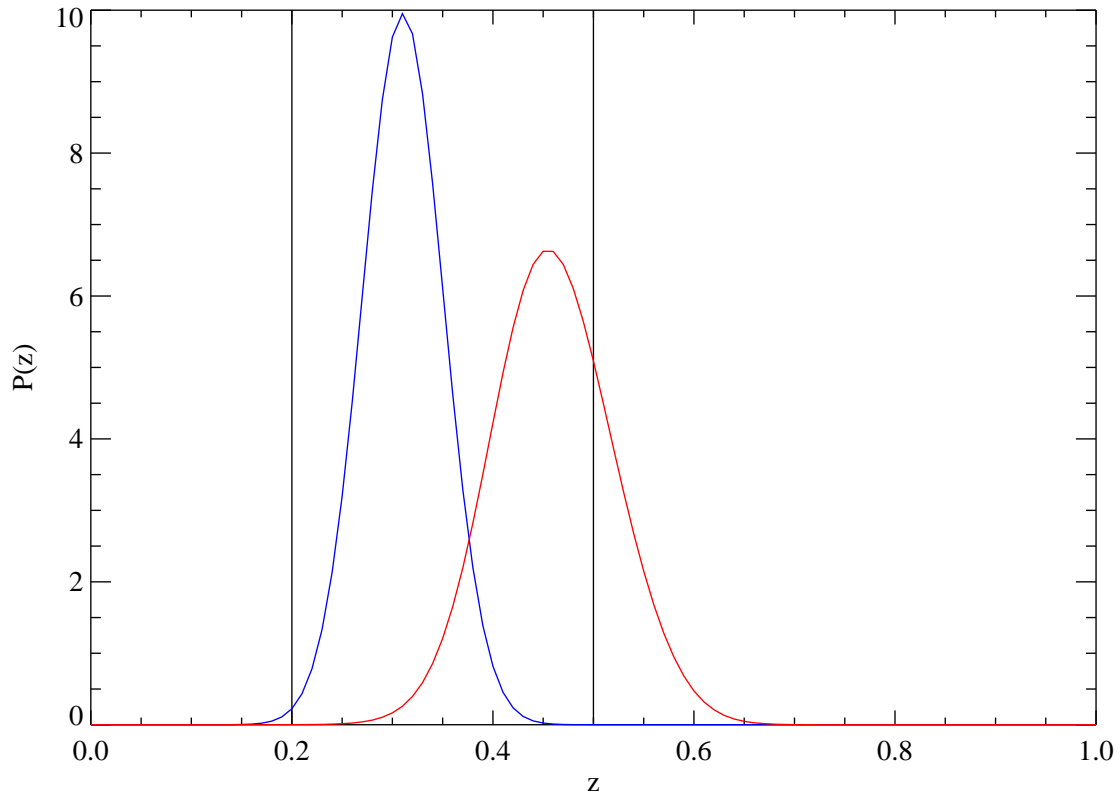
Figure 7.1 Redshift likelihood functions of two galaxies with maximum likelihood redshifts in the $0.2 \leq z \leq 0.5$ redshift bin. This graph demonstrates the need to weight the galaxies using redshift information from the likelihood functions.

due to the addition of uncorrelated galaxies. From the simple ML perspective, this can be understood as the scattering of both lower and higher redshift galaxies into our sample at a rate determined by the error distribution. From the RLF perspective we see that an equal weighting scheme ignores the differences in probability, as determined though integration of the RLF, of the galaxies being correctly included. Even the $z \sim 0.31$ galaxy has some low–level probability below the low redshift cutoff. Ideally the complete redshift likelihood function should be utilized to weight the galaxies appropriately.

In their study of clustering in the HDF, Magliocchetti and Maddox (1999) modelled the photometric redshift errors with a simple Gaussian error distribution. In order to account for the redshift uncertainty, they convolved this error distribution with each redshift interval in their analysis, in effect broadening the redshift interval, and hence boosting the correlation lengths derived from the Limber deprojection. While the assumption of a Gaussian error distribution is reasonable for most high S/N galaxies (e.g. see Section §4.7), it clearly is not for the multiply–peaked likelihood functions common for fainter galaxies. In addition, the assumption of a *single* error distribution for all galaxies is demonstrably incorrect, as some galaxies have extremely narrow, pseudo delta–function error distributions, whereas others have

extremely broad RLFs.

While there are many ways of including the full RLF information, we choose to employ an extremely simple approach which nevertheless uses all the available information for each galaxy. Associating the area under the redshift likelihood functions directly with probability, an assumption we tested and justified in Section §4.7, we can assign weights to each galaxy based on the fraction of its RLF that is enclosed by the limits of each redshift interval. For example, the weights for the two galaxies in Figure 7.1 are 0.997 and 0.752.

Rather than a simple sum of ordered pairs, the DD, DR, and RR pair counts are then

$$DD = \sum_{i=1}^{N_d} \sum_{j=1}^{N_d} (1 - \delta_{ij})\, w_{d,i}\, w_{d,j} \qquad (7.14)$$

$$DR = \sum_{i=1}^{N_d} \sum_{j=1}^{N_r} w_{d,i}\, w_{r,j} \qquad (7.15)$$

$$RR = \sum_{i=1}^{N_r} \sum_{j=1}^{N_r} (1 - \delta_{ij})\, w_{r,i}\, w_{r,j} \qquad (7.16)$$

where w_d are the data weights as calculated above and $w_r = 1$ are the random weights. The ACF estimators, Equations 7.11 and 7.12, are then normalized not by the number (N_d) of galaxies in the sample, but rather by the sum of the DD weights, N_d^w:

$$N_d \rightarrow N_d^w = \sum_{i=1}^{N_d} w_{d,i}. \qquad (7.17)$$

Of course, the weighting for the random galaxies is unchanged

$$N_r \rightarrow N_r^w = \sum_{i=1}^{N_r} w_{r,i} = N_r. \qquad (7.18)$$

7.4   Integral Constraint

Integrating the angular version of Equation 7.1 over all space

$$\langle N \rangle^2 = (\bar{n}\Omega)^2 + \bar{n}^2 \int \int \omega(\theta)\, d\Omega_1 d\Omega_2 \qquad (7.19)$$

produces an important constraint on $\omega(\theta)$. Since $\bar{n} \equiv \langle N \rangle / \Omega$ the integral over the correlation function must vanish. This equation demonstrates the origin of the *integral constraint*. This constraint plays an important role in the practical estimation of the correlation function in all surveys smaller in extent than ($\sim$ twice) the full range of galaxy correlations, which, in local surveys, has been measured out to $\sim 1° - 2°$ scales (Connolly et al. 2002). The CFDF–PRS fields, while very large, are nevertheless smaller than this, leading to an overestimate of the mean density (as there is excess probability due to clustering

over separations as large as our fields). We must therefore account for the integral constraint in our estimation of the ACF.

We define the integral constraint (IC) correction, C, as

$$C \equiv \frac{1}{\Omega^2} \int \int \omega(\theta) \, d\Omega_1 d\Omega_2, \tag{7.20}$$

and calculate this quantity in each of our three fields subject to our spatial selection function (including complete field masking) using a Monte Carlo integration, assuming that $\omega(\theta) = A_\omega \theta^{-\delta}$ and $\delta = 0.8$. This latter choice was taken for two reasons. We show below that at small separations, where the IC correction is negligible, our raw ACF measurements have a slope quite consistent with $\delta = 0.8$, the fiducial slope that has been found by most other surveys. In order to facilitate the comparison of our final correlation lengths with the literature we will fit our ACF amplitudes using a fixed $\delta = 0.8$ slope. We find that $C = \{4.37A_\omega, 4.43A_\omega, 5.33A_\omega\}$ for our {03hr, 14hr, 22hr} fields.

We then fit the equation

$$\omega(\theta) = A_\omega \theta^{-\delta} - C \tag{7.21}$$

to our measured correlations to determine the amplitude, A_ω, at $\theta = 1°$. Note that this equation, with the integral constraint correction, automatically satisfies Equation 7.19.

The constant IC correction is completely negligible at small scales, becoming more important on scales of order $\sim 10\%$ of the field size. While we rigorously calculate and employ the IC correction, we nevertheless limit its influence on the final amplitudes by restricting our fitting range to $(0.0015° \leq \theta \leq 0.03°)$ or $(5'' \lesssim \theta \lesssim 100'')$.

7.4.1 Justification for Fixing $\delta = 0.8$

Although the strong covariance between the amplitude and slope evident from Equation 7.21 allows for a satisfactory formal fit for a range of slopes, it is obviously best if the adopted slope is very close to the best–fit value. In Figure 7.2 we fit this equation for both amplitude *and* slope in the angular correlation function measured for galaxies in the $0.2 \leq z \leq 1.2$ redshift range, resulting in a best–fit slope of $\delta_{IC} = 0.73 \pm 0.06$. Alternatively, fitting a simple power law produced a best fit slope of $\delta = 0.83 \pm 0.03$. These results justify our choice of a fixed $\delta = 0.8$ slope in this analysis.

7.5 Division of the Sample into Redshift Bins

We divide our sample into three redshift regimes, based primarily upon the reliability of the photometric redshifts. Conceptually these regimes are unique in terms of the combination of redshift accuracy and
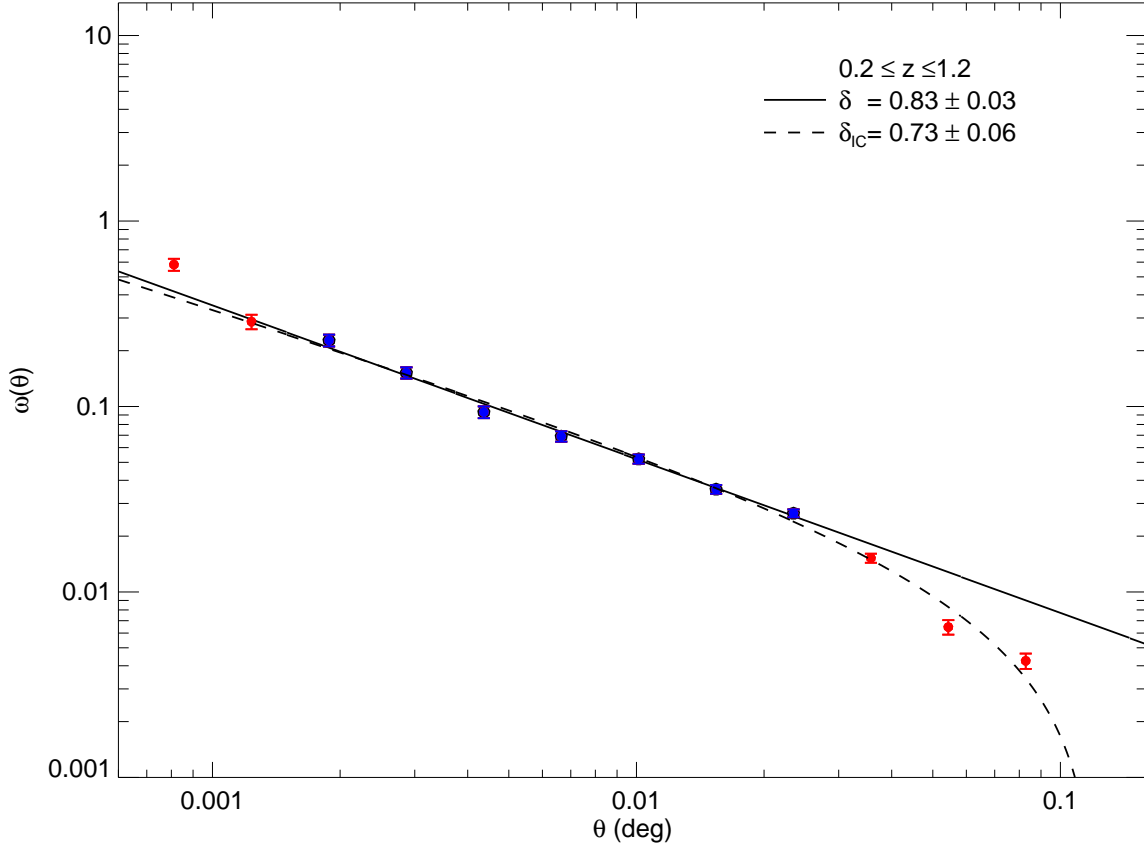
Figure 7.2 Slope of angular correlation function over $0.2 \leq z \leq 1.2$. The long–dashed line is the best fit form of Equation 7.21 which includes the effect of the integral constraint; the solid line is a simple power law fit. Both have best–fit slopes substantially in agreement with $\delta = 0.8$. The blue points show the range of separations included in the fits.

galaxy density, and we describe them each in turn.

In the $0.2 \leq z \leq 1.2$ regime, where we have fully tested the reliability of the photometric redshift method and characterized its error properties, we calculate the ACF in relatively narrow redshift bins. These bins were chosen to have a minimum width of roughly twice the mean redshift dispersion, which was $\sigma_z \simeq 0.06 \,(1 + z)$ to $I_{\mathrm{AB}} = 24$, while keeping the number of galaxies per bin roughly constant (~ 5000).

At $z > 3$ the only significant difference is the vastly smaller number of objects included to $I_{\mathrm{AB}} \leq 24$. The redshift accuracy follows (or surpasses) the relation established at low redshift, as the Lyman continuum break has entered the U–band, providing a strong redshift indicator analogous to the 4000 Å break at $z \leq 1.3$. Due to the low number density we impose a single relatively wide redshift bin in this regime ($2.9 \leq z \leq 3.9$). Despite this, the sample is only $\sim 10\%$ the size of that in each low–z bin. In order to maintain a broadly consistent measurement accuracy at each redshift, we take advantage of our

extremely deep, high quality CFH12k supplementary imaging in the 03hr and 22hr fields to push beyond the $I_{\mathrm{AB}} = 24$ limit and measure correlations in this redshift range for ~ 1800 $I_{\mathrm{AB}} \leq 25$ galaxies in these two fields. We are in effect lowering the random Poisson noise at a risk of increasing the systematic error in the form of catastrophic redshift errors. As discussed in Section §4.6, the strong redshift signal inherent in $z > 3$ galaxies largely mitigates the increasing photometric errors with survey depth, allowing robust redshift estimation even at S/N levels of ~ 3. Further, limiting the redshift range to $z \geq 2.9$ removes the only redshift region plagued with serious degeneracies. Even to $I_{\mathrm{AB}} \leq 25$ our sample is brighter and at higher S/N than the Steidel et al. (2003) sample we studied in Section §4.6, which, for $z \geq 2.9$ galaxies, had a catastrophic failure rate of just 7%. This is in line with the error fraction at low redshift (recall Figure 4.4). A more serious issue with extending the sample beyond $I_{\mathrm{AB}} = 24$ is that differential incompleteness between the fields may arise. We therefore do not compute combined correlations (i.e. running the pair count sums over both fields) for our $I_{\mathrm{AB}} \leq 25$ sample, limiting ourselves instead to a simple weighted average of the results in the two fields.

The final redshift range, bracketed by the above two redshift regimes, is precisely where our photometric redshift algorithm fares poorest. Our filter set provides very little redshift discrimination between $1.3 \lesssim z \lesssim 2.9$ due to the lack of a prominent spectral break. Paradoxically, we can exploit this fact to allow an accurate measurement of the correlation function in this important redshift range. While our *UBVRIZ* filter set does not allow us to differentiate between hypothetical galaxies at $z = 1.6$ and $z = 2.3$, we are, however, certain that neither one is at $0.2 \lesssim z \lesssim 1.3$ *nor* $z \gtrsim 2.9$. If they were, a strong, easily detectable continuum break would betray the fact. We can therefore conclude that while our redshift resolution *within* the $1.3 \lesssim z \lesssim 2.9$ regime is quite poor, adopting a single redshift bin spanning this entire range allows us to effectively group all of these galaxies together and isolate them from the other two redshift regimes. In practice we limit the redshift bin to $1.3 \leq z \leq 2.7$ to minimize exposure to the redshift degeneracy between faint $z \sim 0$ and $z \approx 2.8$ galaxies discussed above. Due to the rapidly decreasing redshift distribution at $z \geq 1.3$ the effective redshift, z_{eff}, of our correlation measurements is strongly weighted to lower redshifts. Although the midpoint of the redshift bin is $z = 2$, the effective redshift is $z_{\mathrm{eff}} = 1.69$. This sample selection produces ~ 4700 galaxies to $I_{\mathrm{AB}} \leq 24$, providing an excellent intermediate redshift counterpart to our $z \lesssim 1$ sample.

We point out that we may may missing as much as $\sim 10\%$ of the variance in each redshift bin due to the effect of catastrophic errors in our redshift estimation. We expect less than $\sim 8\%$ of galaxies to be assigned incorrect redshifts, which has the effect of diluting the true correlation signal. However since the galaxies are not randomly distributed like stars, the effect is probably less severe than the $1/(1-f)^2$ dilution effect for stellar contamination, which certainly sets an upper limit. The effect is more likely

$\sim 1/(1-f)$, where f is the catastrophic fraction.

7.6   Results

In each field the ACF was computed using the above pair weighting scheme, with the errors taken to be Poissonian in the weakly clustered regime, $d\omega = (1+\omega)/\sqrt{DD}$. We used 500,000 randoms to ensure that the sampling error coming from the Monte Carlo integration was negligible. The measured correlation functions were then averaged together, weighted by the effective number of pairs in each field, with the error bars calculated from the field to field variance in $\omega(\theta)$. The results are plotted in Figure 7.3. The
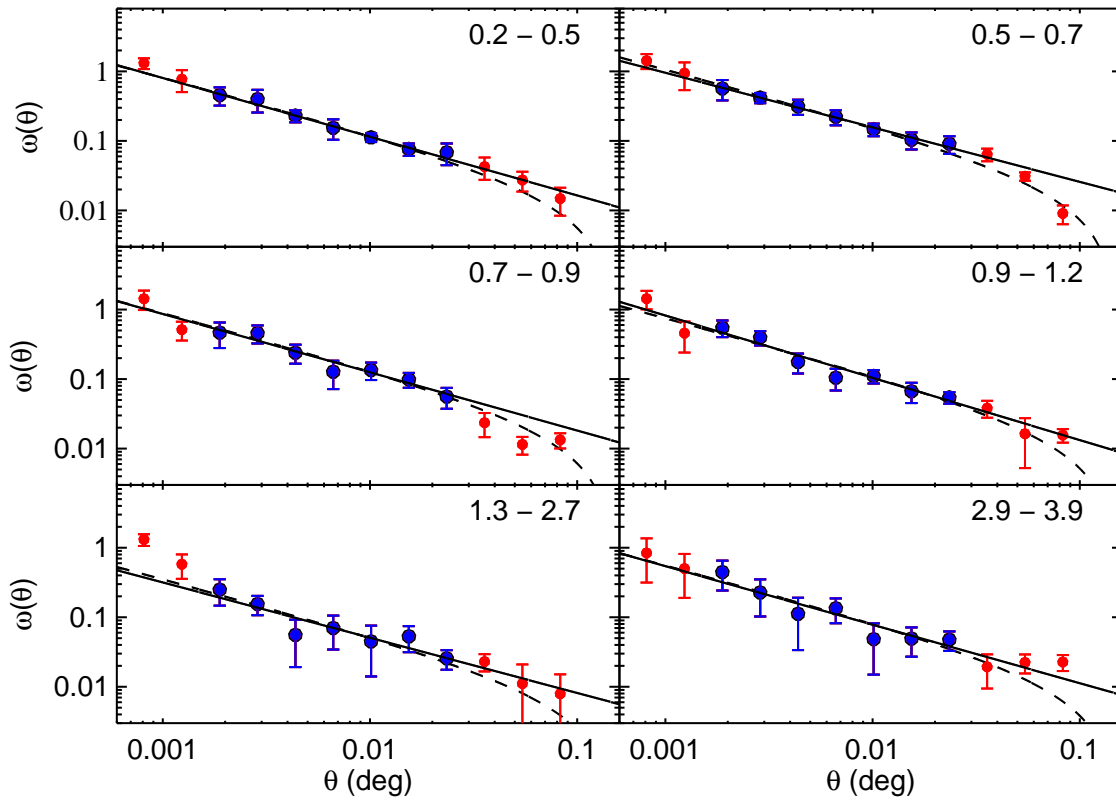
Figure 7.3 Angular correlation function in redshift bins from $0 \lesssim z \lesssim 4$ using the Landy & Szalay estimator. Once again the solid line is a direct power law fit, but this time the long–dashed line is a fit of Equation 7.21 with the slope fixed at $\delta = 0.8$. In our analysis we adopt the amplitudes derived from the latter. The blue points show the range of separations included in the fits.

solid straight line in each panel is a direct power law fit (both amplitude and slope) to the data between $0.0015° \leq \theta \leq 0.03°$, neglecting the integral constraint. The dashed curve is the best–fit function of the form of Equation 7.21, over the same angular interval, with the slope fixed to $\delta = 0.8$. Clearly the $\delta = 0.8$ slope provides an excellent description of the data. In this analysis we adopt the amplitudes

derived from the latter fit including the integral constraint, although we note that our fitting range (denoted by the blue points in the Figure) effectively removes its influence on the result.
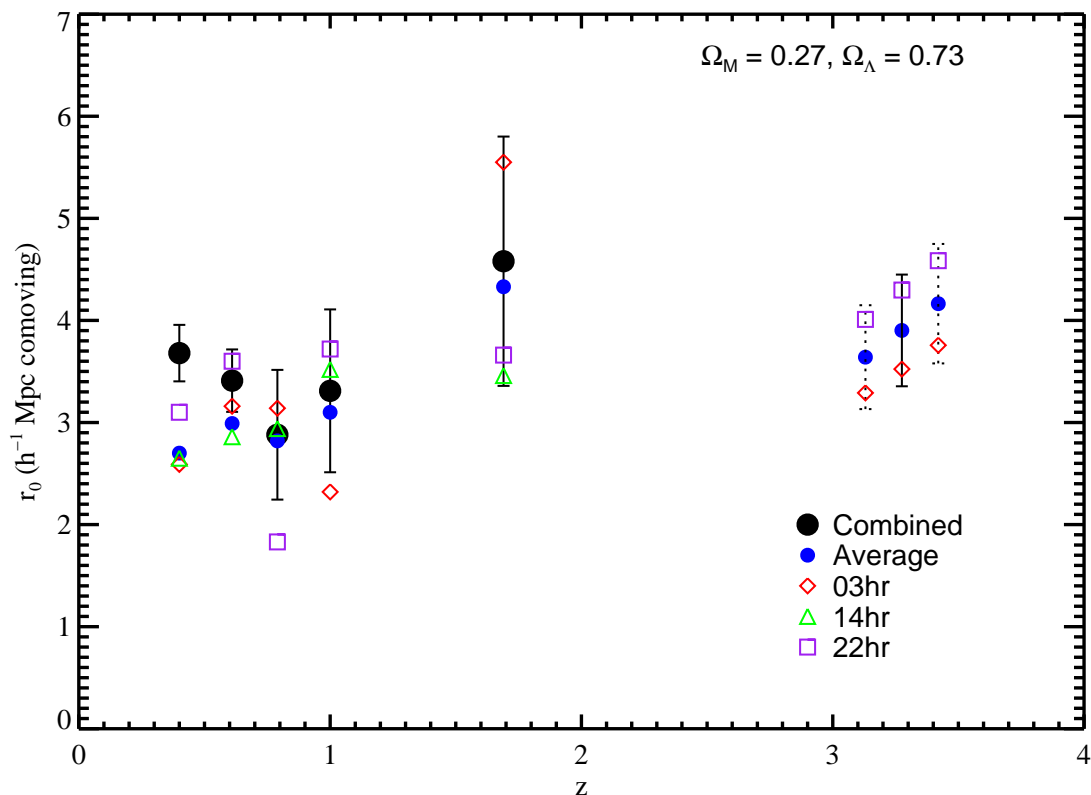
Figure 7.4 Redshift evolution of correlation amplitudes in the CFDF–PRS. The 03hr, 14hr, and 22hr fields are represented by the diamonds, triangles, and squares, respectively. The weighted average is denoted by the small filled circles, and the combined amplitude over all fields is represented by the large filled circles. The error bars are derived from the field to field variance. The two points with the dotted error bars represent different choices of $N(z)$ at $z \sim 3$ as described in the text. The $z = 3.28$ point with the solid error bar is the average of these.

We derive correlation lengths in each redshift regime using Equation 7.9 for our chosen cosmology ($\Omega_M = 0.27, \Omega_\Lambda = 0.73$), and plot the results in Figure 7.4. In addition to the correlation amplitudes in each field (diamond, triangle, and square symbols for the 03hr, 14hr, and 22hr fields), we plot both the average (small filled circles) and the combined amplitudes (large filled circles). The former are weighted by the number of pairs in each field, whereas the latter are computed by extending the pair count sums over all fields. This method takes into account the clustering on scales much larger than the field size through its effect on the mean galaxy density, and in general produces clustering amplitudes larger than in the individual fields. As is clear from Figure 6.2 the density of objects at each redshift varies substantially from field to field, and where the variation is largest (e.g. at $z \sim 0.3$) the combined approach correctly produces the largest amplitudes. The error bars are derived from the field to field

variation about the weighted average value, but placed on the best–estimate combined amplitude.

We have adopted the $N(z)$ parametrization for the $18.5 \leq I_{\mathrm{AB}} \leq 24$ sample derived from the same data and given in Table 6.5. While this is optimal for the five $z < 2$ redshift bins, it is not strictly correct at $z \sim 3$ where our sample extends to $I_{\mathrm{AB}} = 25$. We therefore compute r_0 in the final bin using two different redshift distributions, plotted with dotted error bars in Figure 7.4, which should produce correlation amplitudes that bracket the correct value. We use our measured $N(z)$ as above, although it likely weights the low redshift end of the bin too heavily, as the correct $N(z)$ for the fainter $I_{\mathrm{AB}} = 25$ sample probably falls off less steeply. On the other extreme, we adopt a simple top hat distribution, which certainly weights the higher redshift galaxies too strongly. The effective redshifts, calculated using Equation 7.10, are quite different for these two distributions, though the derived amplitudes themselves only vary by about 15%. We tentatively adopt the simple average of these estimates, plotted with the solid error bar in Figure 7.4, as the best–estimate clustering amplitude at $z \sim 3$. We have not computed a combined amplitude as the completeness to $I_{\mathrm{AB}} = 25$ is not 100% and will likely be different from field to field. Our measurement should therefore be formally considered a lower limit to the clustering amplitude at $z \sim 3$, at least in comparison to our results at lower redshifts. However, the large linear extent of each field at $z \sim 3$ ($\sim 40\, h^{-1}$ Mpc), coupled with the extreme depth of the sample ($I_{\mathrm{AB}} \leq 25$) should somewhat minimize the field to field mean density differences, at least compared to the brighter sample at lower redshift. Therefore, we expect that the combined result would likely not be significantly higher than the weighted average. Table 7.1 lists the calculated correlation lengths for various background cosmologies.

7.7   Comparison with the CFRS

Before we compare our results to other, independent surveys, we make a comparison with previous clustering results measured in the very same fields that form the subject of this study. Le Fèvre et al. (1996) measured the real–space clustering of galaxies to $z \sim 1$ in five fields, three common to this work, in the original CFRS survey. At the time $\Lambda \neq 0$ cosmologies were not in vogue and so we must convert the CFRS results to the present concordance cosmology before comparison.

An intuitive way to do this is to project the real–space correlation function down to a cosmology–independent angular function using Equation 7.6 with the original CFRS cosmology, and then to depro-

Table 7.1.   Redshift Evolution of Correlations

Δz	z_{eff}	N_{gal}	$N(z)^1$	$A_\omega{}^2$ $(\times 10^{-3})$	$r_0{}^3$(a) $(h^{-1}\ \mathrm{Mpc})$	r_0 (b) $(h^{-1}\ \mathrm{Mpc})$	r_0 (c) $(h^{-1}\ \mathrm{Mpc})$
$0.2 - 0.5$	0.40	4801	N_{24}	5.71 ± 0.17	3.68 ± 0.28	3.81 ± 0.28	3.63 ± 0.28
$0.5 - 0.7$	0.61	5039	N_{24}	5.41 ± 0.19	3.41 ± 0.31	3.59 ± 0.32	3.35 ± 0.30
$0.7 - 0.9$	0.79	5500	N_{24}	3.70 ± 0.20	2.88 ± 0.64	3.06 ± 0.67	2.81 ± 0.62
$0.9 - 1.2$	1.00	4185	N_{24}	3.40 ± 0.29	3.31 ± 0.80	3.56 ± 0.86	3.22 ± 0.78
$1.3 - 2.7$	1.69	4727	N_{24}	1.57 ± 0.15	4.58 ± 1.22	5.04 ± 1.35	4.42 ± 1.18
$2.9 - 3.9$	3.28	1803	$\langle N_{24},\ \text{top hat}\rangle$	2.24 ± 0.40	3.90 ± 0.55	4.39 ± 0.62	3.74 ± 0.53
$2.9 - 3.9$	3.13	1803	N_{24}	2.24 ± 0.40	3.64 ± 0.51	4.09 ± 0.57	3.49 ± 0.49
$2.9 - 3.9$	3.42	1803	top hat	2.24 ± 0.40	4.16 ± 0.59	4.69 ± 0.66	3.99 ± 0.57

[1]Redshift distribution used for deprojection: N_{24} is the $18.5 \leq I_{\mathrm{AB}} \leq 24$ distribution measured in Chapter 6. The final amplitude at $z_{\mathrm{eff}} = 3.28$ was computed using the mean of amplitudes calculated using the N_{24} and top hat redshift distributions, listed below the rule.

[2]A_ω is the amplitude at $\theta = 1°$ and has been fitted with a fixed $\delta = 0.8$ slope.

[3]The correlation lengths, r_0, are computed in three Λ–flat cosmologies: (a) $\Omega_M = 0.27, \Omega_\Lambda = 0.73$, (b) $\Omega_M = 0.20, \Omega_\Lambda = 0.80$, and (c) $\Omega_M = 0.30, \Omega_\Lambda = 0.70$.

Note. — The $z_{\mathrm{eff}} \sim 3$ entries list the weighted average of the 03hr and 22hr fields, whereas at lower redshift we list the correlations combined over all three CFDF–PRS fields.

ject it using the current cosmology. The new correlation length can then be written as

$$r_{0\Lambda} = r_{0(\Lambda=0)} \left[\frac{\int_{z1}^{z2} N^2(z)[x_{(\Lambda=0)}(z)]^{1-\gamma} E_{(\Lambda=0)}(z)dz}{\int_{z1}^{z2} N^2(z)[x_\Lambda(z)]^{1-\gamma} E_\Lambda(z)dz} \right]^{1/\gamma}. \tag{7.22}$$

Note that the CFRS cosmology, $\{\Omega_m = 1, \Omega_\Lambda = 0\}$, is also spatially flat and so the curvature factor, $F(z)$, from Equation 7.6 remains unity. To make this transformation accurately we require the CFRS redshift distribution to $I_{\mathrm{AB}} \leq 22.5$, which we measured in Chapter 6 and parametrized in Table 6.5. Before using Equation 7.22 we transform the original CFRS correlation lengths to comoving units normalized to $\gamma = 1.8$.

As Figure 7.5 shows, the measured CFRS correlations are somewhat smaller than our combined amplitudes, although not as dramatically as sometimes reported in studies that do not transform the CFRS results to a modern cosmology. Nevertheless the difference at $z \sim 0.6$, a regime in which both surveys have excellent sensitivity, may seem odd considering the fields are largely the same and therefore cosmic variance, at least to first order, is not to blame for the discrepancy. There are various possible causes for lower clustering amplitudes in the CFRS, among them small number statistics (there were only 100–200 galaxies in each redshift bin) and the complicated spatial selection function. The latter, imposed
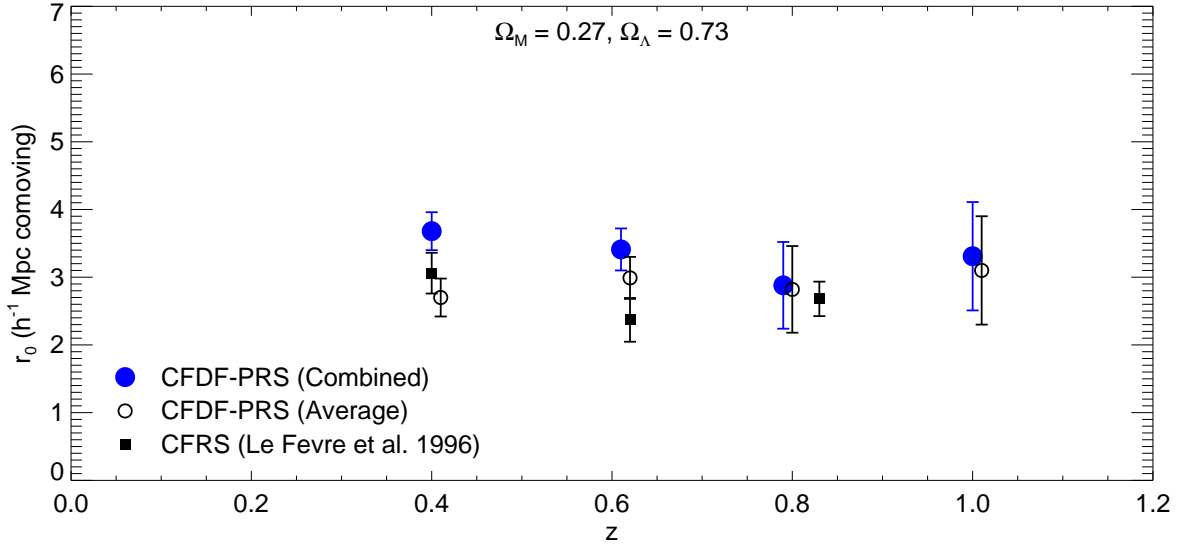
Figure 7.5 Comparison with the Canada–France Redshift Survey (Le Fèvre et al. 1996). Converted to our concordance cosmology, the correlation lengths in the CFRS (filled squares) are slightly smaller than the combined CFDF–PRS measurements (large filled circles), but in good agreement with the average amplitudes in our fields, plotted here as small open circles offset by $\Delta z = 0.01$ for clarity.

by the constraints of the survey design which was optimized for multi–object spectroscopic efficiency, led to a catalogue of objects located in several $10' \times 1'$ strips. The narrower field dimension could perhaps have led to a loss of sensitivity to some fraction of close pairs within one correlation length. This spatial selection also complicated the generation of the random galaxy sample in their Monte Carlo integration. They opted to place their random galaxies at the same (α, δ) positions occupied by the real galaxies and assign a redshift chosen at random from the measured spectroscopic sample. This method, while having the virtue of providing exactly the same selection function as the data, biased their correlation estimates to the low side since the random galaxies, having the same angular distribution as the real galaxies, were themselves correlated. The effect was small compared with 3-D $w_p(r_p)$ clustering of the galaxy sample, and was expected to decrease the apparent slope of the correlation function by only 0.03. While they ignored this small effect, which effectively boosts their correlation signal by 1%–2%, we have included it for this comparison.

On the other hand, the CFRS did not measure correlations combined over all fields as we have. If we instead compare our average amplitudes, denoted by the smaller open circles in the Figure, the surveys are in complete agreement as expected. This is quite impressive considering that, as the pioneering high redshift survey, the CFRS is dwarfed by modern surveys, including the present one, in both field and sample size.

7.8   Comparison with Other Photometric Redshift Surveys

Presently the only practical way to measure correlations over as broad a range of redshift as in the present work is to use photometric redshifts. The only published surveys that do so are the HDF studies of Magliocchetti and Maddox (1999) and Arnouts et al. (1999; 2002), which were more proof of concept papers rather than actual measurements. This rather strong statement is justified as follows. The HDF field size at $z = 1$ corresponds to a comoving scale of only $\sim 1.7\,h^{-1}$ Mpc, rising to $\sim 3.3\,h^{-1}$ Mpc at $z = 3$, making it difficult to measure correlations on scales larger than this. In addition the minuscule number of galaxies in each redshift bin ($\sim 50 - 200$), coupled with the fact that these studies were done on a single field, make clear that the error bars in the Magliocchetti and Maddox (1999) paper, ranging from 55% – 100% (or more) of the final correlation lengths, are probably appropriate. Had they been spectroscopic in nature, the field and sample size limitations of these surveys may not have precluded their scientific usefulness, but in large redshift bins the projection effects which reduce the correlation function by one power produce small–scale clustering signals of order 0.1 as opposed to 100. There is therefore little point in a detailed quantitative comparison with these surveys.

The above caveats regarding field and sample size aside, there is nothing wrong with the method employed in these surveys. The only photometric redshift survey published to date studying the general galaxy population that has serviceable signal to noise is the CADIS survey (Phleps and Meisenheimer 2003). This survey uses 13 medium–band and 3 broad band filters to achieve a photometric redshift accuracy of $\sigma = 0.02$ for 3600 galaxies to $I \leq 23$ and $z \lesssim 1$. Given their smaller redshift errors, they opted to measure the 3–dimensional correlation function, $w_p(r_p)$, as opposed to $\omega(\theta)$, which requires integration of the two dimensional real–space correlation function along the line of sight in order to remove redshift–space distortions caused by peculiar velocities. In the CADIS survey, the photometric errors, large by spectroscopic standards, force the extension of this integral to separations of $\Delta z = 0.05$ to ensure the inclusion of all correlated galaxies. Figure 7.6 plots the CADIS results alongside our own.

Clearly the two survey surveys are in excellent agreement at $z \sim 0.4$. However, beyond this redshift the CADIS survey observes a rapid decline in the clustering strength that we do not reproduce. Although we are formally in agreement with all their measurements, the character of the clustering evolution is clearly quite different between the two surveys. We turn now to comparisons with the current best correlation estimates from the largest spectroscopic surveys.
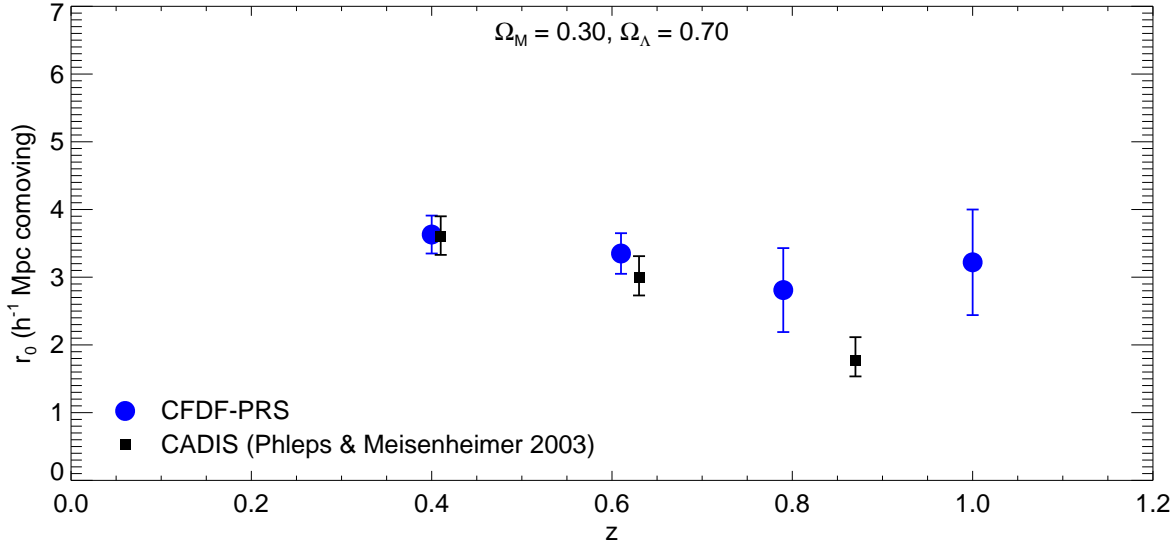
Figure 7.6 Comparison with the CADIS (Phleps and Meisenheimer 2003) photometric redshift survey. The clustering measurements are largely in agreement between the surveys, however the CADIS survey detects a sharp decline in clustering with redshift that we do not observe.

7.9 Comparison with Other Spectroscopic Redshift Surveys

Large spectroscopic surveys can be designed to target specific redshift ranges (e.g Steidel et al. 1996, Carlberg et al. 2000, Coil et al. 2004), but the survey strategies are so dependent on redshift and magnitude that it is impractical or impossible to carry out a single spectroscopic survey over the range $0 \lesssim z \lesssim 3$.

Our clustering results based on photometric redshifts are of sufficient quality over this full redshift range so as to require comparison with several large spectroscopic surveys, each operating in their targeted redshift regime. We begin at low redshift where we compare with the CNOC2 redshift survey (Carlberg et al. 2000), as shown in Figure 7.7, using their world model $\{\Omega_M = 0.20, \Omega_\Lambda = 0.80\}$.

7.9.1 Clustering at $z \sim 0.5$

The CNOC2 survey is quite similar to our own in many ways. It is selected in the red, has redshifts for ~ 6000 galaxies to $z \sim 0.5$, and has survey field sizes quite similar to our own ($\sim 0.5°$). Both surveys measure correlation function slopes in excellent agreement with $(\delta, \gamma) = (0.8, 1.8)$. We have therefore based our analysis loosely on theirs to allow for a meaningful comparison. Specifically, we measure combined correlations over all fields, and estimate errors from field to field variance, using methods quite similar to theirs. The results in fact show excellent agreement between the two surveys in the $0.4 \lesssim z \lesssim 0.6$ overlap region.
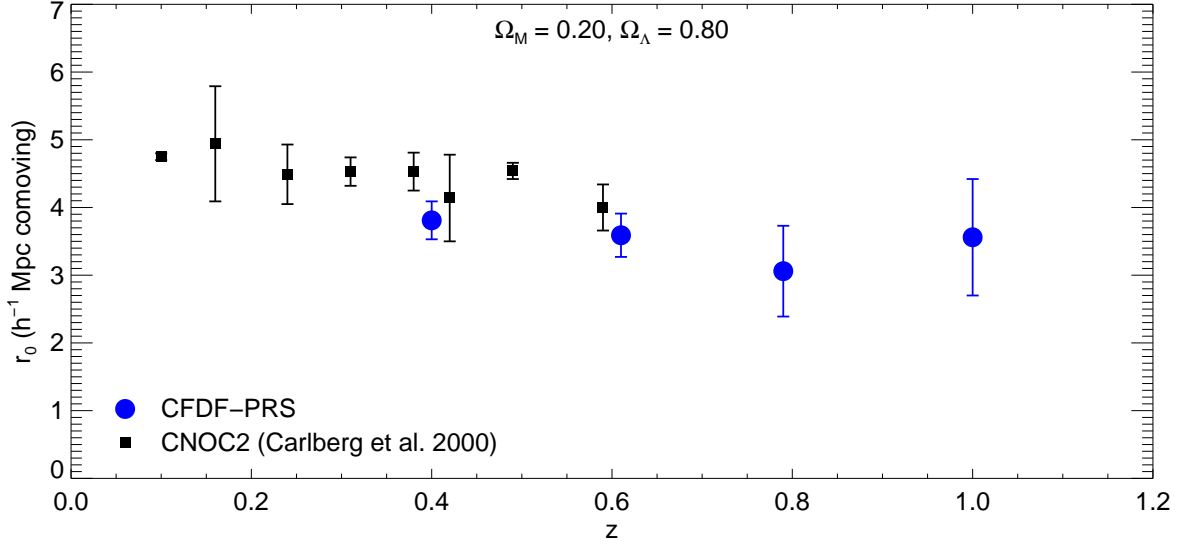
Figure 7.7 Comparison with the CNOC2 (Carlberg et al. 2000) redshift survey. The evolution of r_0 with redshift agrees very well with the CNOC2 in the $0.4 \lesssim z \lesssim 0.6$ overlap region. We have adopted the CNOC2 world model for this comparison.

The fact that our correlations appear slightly systematically low compared with the CNOC2 is not only understandable but expected. Despite the similarities, the CNOC2 clustering sample differs from our own in several important ways, all of which tend to increase the galaxy correlations in their survey relative to ours. It is a volume–limited sample, as opposed to our own flux–limited survey, with an absolute magnitude limit of $M_R \leq 20$. It therefore omits the fainter $\sim 60\%$ of the galaxies in the CNOC2 $R_C \leq 21.5$ catalogue, already much brighter than our own $I_{AB} \leq 24$ limit, whose inclusion would tend to lower the measured clustering amplitudes. Additionally, the galaxy magnitudes are evolution–corrected using the CNOC2 luminosity functions (Lin et al. 1999), which minimizes the number of intrinsically fainter galaxies that are included at higher redshifts. Several recent studies including the CNOC2 itself have convincingly demonstrated the luminosity dependence of the correlation function (e.g. Norberg et al. 2001; 2002a, Shepherd et al. 2001, Foucaud et al. 2003, Budavári et al. 2003), in particular for L^* or brighter galaxies, and so we would predict at least a modest offset between the correlation amplitudes measured in the two surveys.

Given these differences, it is remarkable that the agreement is as impressive as it is. The similarity in the size of the error bars is not surprising, however, as they are estimated uniformly in both surveys from field to field variations, in similar sized fields and with large numbers of galaxies (although our sample is roughly four times larger in the overlap region).

7.9.2   Clustering at $z \sim 1$

We now turn to the $z \sim 1$ regime in which it has been quite difficult to make reliable spectroscopic clustering measurements due to the depth required. The ongoing DEEP2 survey (Davis et al. 2003) is a next–generation spectroscopic survey that uses simple colour criteria to preselect $z \sim 1$ objects and observes them spectroscopically using the new DEIMOS spectrograph on Keck II. Although the complex colour selection somewhat complicates a direct comparison with our own survey, the magnitude limit of the galaxies included in the colour cuts ($R_{AB} \leq 24.1$) is similar to the present work. Galaxy correlation lengths have been measured by Coil et al. (2004) in preliminary DEEP2 data for 2219 galaxies between $0.7 \leq z \leq 1.35$ which is roughly 20% of our sample size in this range. A comparison with our results is plotted in Figure 7.8.
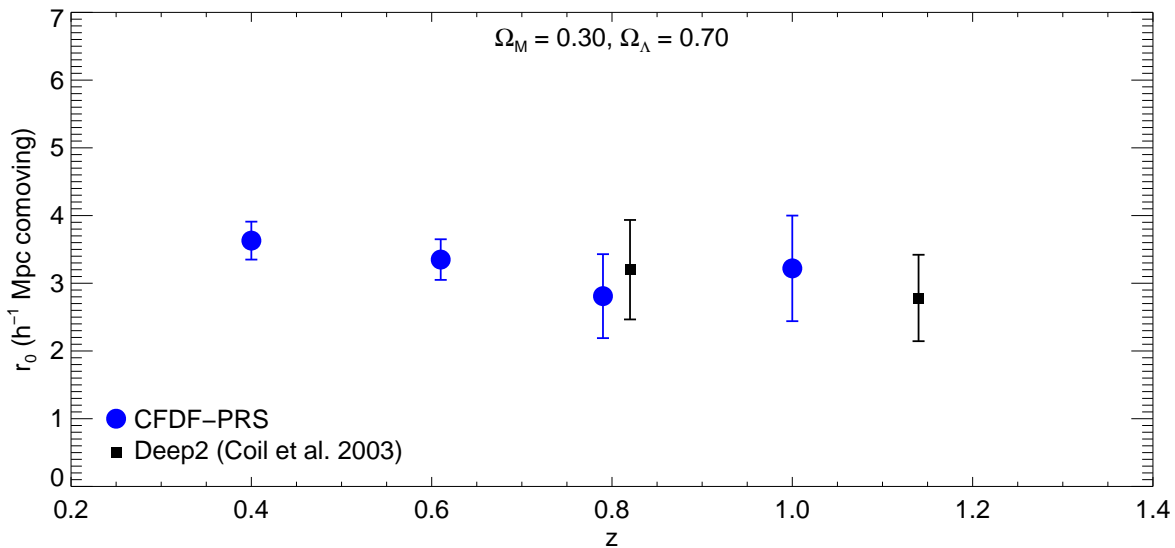
Figure 7.8 Comparison with the DEEP2 (Coil et al. 2004) redshift survey. We have normalized their correlation lengths to $\gamma = 1.8$. Measurements of r_o are completely consistent between the surveys, despite the differences in sample selection. We have adopted the DEEP2 world model for this comparison.

Once again we find excellent agreement between our results and the state–of–the–art spectroscopic measurement. The DEEP2 survey measured slightly shallower slopes ($\gamma \sim 1.65$) than in the CFDF–PRS. This is to be expected since both their colour preselection and their spectroscopic selection function tend to preferentially choose later type galaxies, which as discussed in more detail in Section §7.9.4 below, leads to a shallower slope. In order to make a fair comparison of the clustering amplitudes we normalize their correlation lengths to match our $\gamma = 1.8$ slope.

It is interesting to note that the measurement accuracy, in terms of the quoted fractional error, is almost identical between these surveys, although the DEEP2 team assesses their errors on the basis of

mock catalogues as opposed to field–to–field variance. They are forced to do so as their preliminary measurement is made on a single field, of dimensions quite similar to our own fields ($0.5° \times 0.7°$). This provides a measure of proof that our errors, calculated from the variance of only three fields, do in fact account fairly well for the theoretically expected level of cosmic variance.

7.9.3 Clustering at $z \sim 1.7$

There are no published clustering measurements from a spectroscopic survey at $1.5 \lesssim z \lesssim 2.0$ due to the oft–lamented difficulty in obtaining spectroscopic redshifts in the $1.3 \lesssim z \lesssim 2.3$ "redshift desert". Two different spectroscopic approaches have been proposed to remedy the situation — extension of standard techniques into the near–IR to follow the [O II] 3727Å emission line to higher redshifts, and the development of the nod–and–shuffle technique (Glazebrook and Bland-Hawthorn 2001) which produces far more accurate sky subtractions and allows for detection of weaker rest–UV spectral lines in the observed–frame optical. Both techniques have the potential to remedy the current gap in our knowledge of galaxy evolution, but clustering results, in particular, will be slow in coming. Neither technique is easy to implement for large–scale surveys and current efforts (e.g. Glazebrook et al. 2003) are limited to small fields, the bane of clustering measurements.

On the other hand, this redshift regime is in principle extremely well–suited to a photometric redshift survey, albeit one with near–IR imaging. The addition of moderately deep K–band imaging allows for accurate photometric redshift measurements at all redshifts $0 \leq z \leq 6+$ as predicted in simulations (e.g. Brodwin et al. 1999) and demonstrated in the HDF (e.g. Benítez 2000). While we do not have IR imaging over the whole CFDF–PRS, and therefore cannot subdivide galaxies into, say, $1.3 \leq z \leq 2$ and $2 \leq z \leq 2.7$ redshift bins, we *can* take advantage of a generic property of our *UBVRIZ* filter set, as explained above, to accurately lump *all* $1.3 \leq z \leq 2.7$ galaxies together into a single redshift bin. We can use this broad intermediate redshift sample to make an accurate measurement of the mean clustering properties of galaxies in this redshift range, weighted by the redshift distribution.

The result, depicted graphically in Figure 7.4, shows the measurement in each field, the weighted average of the 3 fields, and the amplitude obtained for the combined survey. The large error bar comes from the stronger correlation seen in the 03hr field ($r_0 \sim 5.5\,h^{-1}$ Mpc) than in the other two fields ($r_0 \sim 3.5\,h^{-1}$ Mpc). The discussion in this subsection assumes a WMAP (Spergel et al. 2003) $\{\Omega_M = 0.27,\ \Omega_\Lambda = 0.73\}$ cosmology. We have examined this field in detail and can find no systematic error to account for the large amplitude. It is true, however, that an unrecognized systematic error will tend to boost correlations, and as such, we are hesitant about drawing any sweeping conclusions about

the clustering strength at $z = 1.7$, short of what is given in the Figure. Omitting the 03hr field would obviously lower the mean correlation amplitude at $z = 1.7$, but would also dramatically shrink the error bar, to perhaps an unreasonably small size. As we have no reason to discard the measurement in the 03hr field, we choose to keep it and draw our conclusions from the full data set. We set a relatively firm lower limit of $r_0 \sim 3.4 \, h^{-1}$ Mpc on the clustering amplitude at $z = 1.7$, and our results are consistent with values in the range $3.4 \, h^{-1}$ Mpc $\lesssim r_0 \lesssim 5.8 \, h^{-1}$ Mpc.

7.9.4   Clustering at $z \sim 3$

There are several measurements of clustering at $z \sim 3$, all of which take advantage of the Lyman continuum break to define their samples. By construction these samples are composed exclusively of Lyman break galaxies (LBGs), which possess a large flux decrement between the observed–frame U and B filters. This decrement, imposed on the galaxy continuum by HI absorption in the IGM along the line of sight, is indicative of their great redshift. In a sense the current survey is no different, since the onset of the Lyman break in our filters defines the beginning of the redshift range where we regain our redshift resolution.

The two classes of measurements in the literature are for spectroscopically confirmed LBGs and for photometric LBG candidates isolated through the use of colour–colour plots pioneered by Steidel et al. (1996). In Foucaud et al. (2003) we made a measurement of galaxy clustering at $z \sim 3$ using the latter technique, although for a brighter sample than in the present survey. There is a subtle but very significant difference between selecting galaxies using colour criteria and computing full–blown photometric redshifts. The former technique was designed not only to find galaxies with negligible U–band flux, but also to select those that are relatively bright in the B–band, indicative of rapidly star–forming galaxies. The idea was to select those $z \sim 3$ galaxies which were expected to have strong UV emission lines to allow for successful spectroscopic confirmation. In contrast, photometric redshifts are equally sensitive to all types of galaxies down to a given apparent magnitude limit. In addition, since they use the full multi–wavelength information for every galaxy, they are less susceptible than simple colours cuts to contamination by low–redshift interlopers. We compare our correlation measurement of $18.5 \leq z \leq 25$ galaxies at $z \sim 3$ to a cross–section of results from the literature in Figure 7.9.

The filled square is the Adelberger et al. (2003) clustering measurement based on a large sample (~ 700) of $\mathscr{R} \leq 25.5$ spectroscopically confirmed LBGs. This study only reports the statistical measurement error. The slope for this LBG catalogue was found to be $\gamma \simeq 1.55$. In the Figure we have normalized the value of r_0 to a $\gamma \simeq 1.8$ slope to allow for a fair comparison of the correlation amplitude.
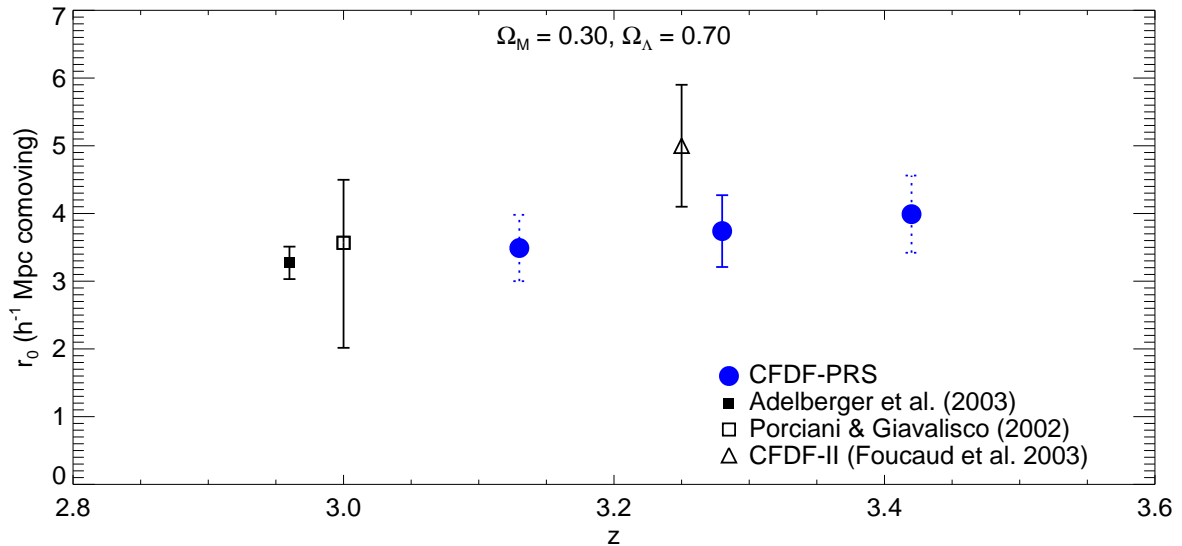
Figure 7.9 Comparison with Lyman break galaxy samples at $z \sim 3$. The solid square is the Adelberger et al. (2003) measurement from the spectroscopic Lyman break galaxy sample of Steidel et al. (2003). The open square and triangle are measurements from the photometrically selected candidate LBG samples of Porciani and Giavalisco (2002) and Foucaud et al. (2003), respectively.

We find an excellent agreement with the Adelberger et al. (2003) measurement, despite its small error bars.

As an aside, it is interesting to note that the Adelberger et al. (2003) correlation length derived with the $\gamma \simeq 1.55$ slope, $r_0 = 3.96 \pm 0.29 \, h^{-1}$ Mpc, is itself in good agreement with our results within the errors. The physical quantity of interest however is $\xi(r = 1 \, h^{-1} \text{ Mpc}) = r_0^\gamma$, and therefore we restrict our quantitative comparisons to correlation lengths (sometimes sloppily called amplitudes) normalized to a common slope, $\gamma = 1.8$.

The open symbols are limber–deprojected correlation lengths resulting from angular clustering measurements of photometric LBG candidates. The square represents the Porciani and Giavalisco (2002) $\mathcal{R} \leq 25.5$ sample of ~ 1000 LBG candidates, whereas the triangle shows the result of the Foucaud et al. (2003) analysis of a $23.5 \leq I_{AB} \leq 24.5$ sample of LBG candidates in the original CFDF UH8k imaging survey. This deepest sample from that study has a luminosity selection closest to the present work, although it is still somewhat brighter.

The Porciani and Giavalisco (2002) study, which employed the *identical* selection criteria (i.e. same filters, depths, colour cuts) used in the spectroscopic target selection of Adelberger et al. (2003), also measured a shallow (though rather uncertain) slope of $\delta = 0.50^{+0.25}_{-0.50}$, adding to the evidence of a shallower slope for pure LBG samples. This is consistent with observations in the local Universe (Budavári et al. 2003) and out to $z \sim 0.5$ (Shepherd et al. 2001) that blue (red) galaxies have shallow (steep) slopes,

and that it is the particular mix of early and late type galaxies that determines the mean slope of the correlation function of the galaxy population. Our simple magnitude–limited sample at $z \sim 3$ is expected to be more representative of the general galaxy population than the LBG samples, and as Figure 7.3 shows we see no evidence for a shallowing of our fiducial $\delta = 0.8$ slope in this redshift bin.

Our correlation amplitude, measured using ~ 1800 galaxies, is in excellent agreement with the Adelberger et al. (2003) and Porciani and Giavalisco (2002) results, which are based on samples that have almost identical brightness limits as our own in the $z \sim 3$ bin. In the 2dF survey Norberg et al. (2002a) conclude that it is the intrinsic luminosity of a sample of galaxies, rather than the specific mix of spectral types included in that sample, which determines the strength of the clustering. It is therefore not surprising that, while the slopes in the deep LBG studies are shallower than in our simpler magnitude limited sample, the correlation amplitudes match up quite well. The brighter Foucaud et al. (2003) sample found a higher correlation length, as expected, although still consistent with the current measurement within the errors.

7.10   Theoretical Implications

As the purpose of this Chapter was to demonstrate the applicability of photometric redshifts to measurements of clustering evolution, we consider it beyond the scope of the present work to conduct a rigorous theoretical interpretation of the results in the preceding Sections. One unambiguous result, though unsurprising, is that the simple ϵ–models of clustering evolution do not hold over the full redshift range sampled here.

The ϵ–models were introduced by Groth and Peebles (1977) as a simple parametrization of the evolution of galaxy correlations which have a direct physical interpretation for special cases of ϵ. They postulate that the correlation function, measured in terms of proper separation, evolves as

$$\xi(r, z) = \left(\frac{r}{r_{00}} \right)^{-\gamma} (1 + z)^{-(3+\epsilon)}, \tag{7.23}$$

where r_{00} is the correlation length at $z = 0$. This can be expressed in terms of the (evolving) comoving correlation length,

$$r_0(z) = r_{00}(1 + z)^{-(3+\epsilon-\gamma)/\gamma}, \tag{7.24}$$

which we can compare to the present measurements. Indeed an important strength of the CFDF–PRS is its ability to test relations like this over such a large range in redshifts. However, as with other deep surveys, both photometric and spectroscopic, we cannot directly make an accurate measurement of the local clustering length, r_{00}, although we could simultaneously fit for r_{00} and ϵ using Equation 7.24.

The CNOC2, faced with a similar problem, used the identically selected local LCRS survey (Shectman et al. 1996) to add low redshift leverage in their fit. For our modest purposes we choose to simply scale the CNOC2–derived value of r_{00} by the ratio of the average of our correlation lengths to theirs in the overlap region, which amounts to decreasing their r_{00} by 9%. Since we attribute the variation between the surveys to sample selection effects, in particular brightness differences and the volume–limited nature of the CNOC2, we view this as a first order approach to normalizing two otherwise quite complementary surveys. We plot in Figure 7.10 the standard ϵ–models using this choice of $r_{00} = 4.41\,h^{-1}$ Mpc.
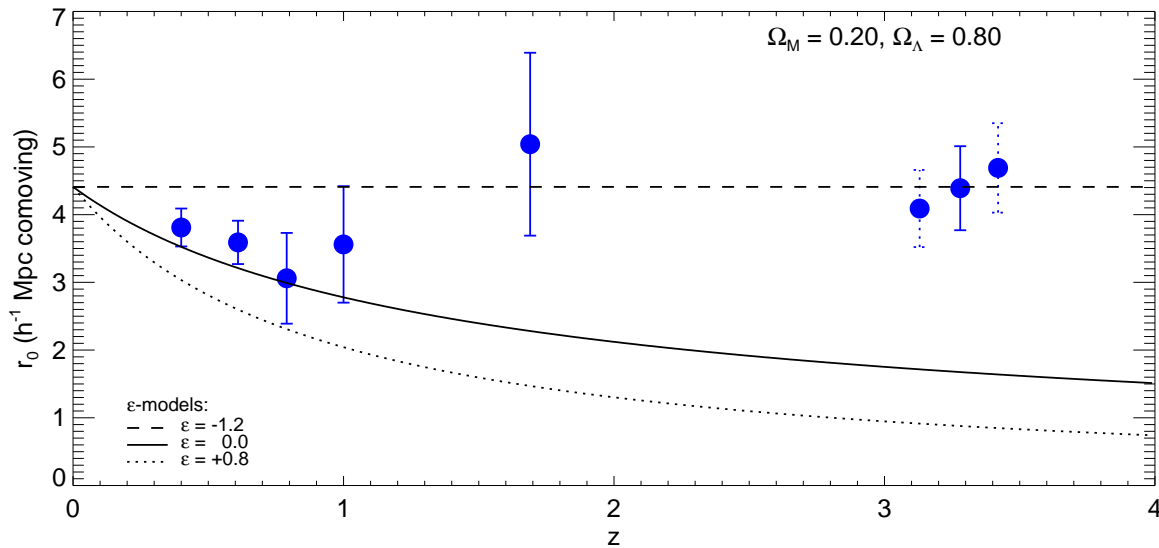
Figure 7.10 ϵ–models vs. CFDF–PRS correlation measurements. No single ϵ–model represents the data over the full redshift range studied in this project.

The $\epsilon = -1.2$ model indicative of a clustering fixed in comoving coordinates is ruled out at low redshift, although only by $\sim 2 - 3\sigma$. It is true that an $\epsilon = -1.2$ model with a very low local correlation length, say, $r_{00} \sim 3.8\,h^{-1}$ Mpc in the cosmology labeled in the Figure, could describe our observed correlation evolution at all redshifts, however there is considerable evidence that the local correlation length is significantly larger than this (e.g. Loveday et al. 1995, Norberg et al. 2002a, Budavári et al. 2003).

The $\epsilon = 0$ model, representing clustering fixed in physical coordinates, fares much better at $z \leq 1$, but fails miserably at $z \sim 3$, as do all models of structure formation that exclude the effect of bias. Our confirmation of strong clustering at $z \sim 3$ is fairly watertight evidence in favour of a biasing scheme of the sort originated by Kaiser (1984) and developed by others (e.g. Bardeen et al. 1986, Mo and White 1996, Jing 1998). This theory holds that galaxies residing in more massive dark matter halos, as preferentially expected at $z \sim 3$ in a magnitude limited survey, have larger correlation amplitudes than

their less–massive (and hence less luminous) counterparts which fall below the detection threshold. The effect is mass–dependent and is related to the underlying dark matter density through a bias parameter, b, defined implicitly by

$$\xi_{\mathrm{gal}} = b^2 \, \xi_{\mathrm{DM}}, \tag{7.25}$$

and which is closely connected to the concept of the peak height of density fluctuations above the background during the gravitational collapse and growth of structure.

With this in mind, an extremely interesting result of this study is the high clustering amplitude seen at $z \sim 1.7$. As mentioned above we have confirmed this result is not spurious by visually inspecting the galaxies in this sample. At issue is that recent semi–analytic models of ab–initio galaxy formation (e.g. Baugh et al. 1999, Kauffmann et al. 1999) predict a minimum of r_0 at $1.5 \leq z \leq 2$, whereas our data, even disregarding the more clustered 03hr field, strongly rules that out. The Kauffmann et al. (1999) study, based on a combination of N–body simulations and semi–analytic galaxy modelling, does point out that the strong "dip" observed in simulations at $1.5 \leq z \leq 2$ is minimized in samples selected in redder bands like our own. With that caveat in mind, we now discuss possible effects which could influence our amplitudes to the high side. We will omit another discussion of the influence of cosmic variance, having dwelt on it in at length in Sections §6.3 and §6.8. We limit ourselves to the observation that it is amply demonstrated by the field to field differences in this redshift bin.

The most obvious factor that may bias our correlation amplitudes upwards is the width of the redshift bin — we are including galaxies from $1.3 \leq z \leq 2.7$. Certainly at the high redshift end of the bin the galaxies are expected to be very strongly clustered, as we see at $z \sim 3$. In fact, there is only about 300 Myr between $z = 2.7$ and $z = 3$ and so we expect relatively little clustering evolution over that time period. Indeed, our clustering amplitude matches that measured at $z \sim 3$ within the errors, and is indistinguishable from it if the 03hr field is neglected. On the other hand, while the $z = 2.7$ galaxies may be more strongly clustered there are relatively very few of them in our wide bin to $I_{\mathrm{AB}} \leq 24$.

Another important concern is the validity of our logic surrounding the use of this redshift bin. While it is true for bright galaxies that the lack of a strong continuum break should correctly place them in this redshift region, what about the fainter galaxies? Certainly a break is only apparent when an accurate continuum measurement can be made. It is possible that faint galaxies are leaking into our bin from higher or lower redshifts, both regimes where the clustering is supposed to be stronger. We tested this in a simple way, by recalculating the correlation function in this interval for $I \leq 23.5$ and $I_{\mathrm{AB}} \leq 23$ galaxies. These brighter samples have limiting S/N levels of 18 and 29 averaged over our three fields (slightly higher in the 03hr field), and yet we see the same clustering strength in all three fields as we

do for the full sample (in fact slightly higher for these brighter samples, although noisier). Therefore, the high amplitudes are not caused by poorly measured continuum breaks – if the breaks were there we would detect them.

We do notice in Figure 7.3 that this is the only redshift range that appears to contain an excess of small scale power. We did not fit the correlation function on scales of less than $5''$ so as to remove sensitivity to various possible systematic effects, including (but not limited to) seeing variations, source extraction errors around bright objects or merging galaxies, and possible unnoticed registration errors. Had we included the $\theta < 5''$ regime in the fit and not fixed our slope to $\delta = 0.8$, we could perhaps have found a steeper best–fit slope which would have reduced the amplitude at $1°$. However, as the $\delta = 0.8$ slope is an excellent fit at all angular scales above $5''$ we are hesitant to use one or two potentially biased data points to attempt to better match the theoretical predictions. We prefer instead to leave the measurement as it is, with all the above-mentioned caveats, and wait to compare with future clustering measurements in this important redshift range. Photometric redshift studies with deep near–IR data, which are currently underway, will have the redshift resolution to measure galaxy clustering in $\Delta z \sim 0.3$ bins at $z \sim 1.5$.

7.11 Recap of Clustering Evolution Results

We have measured the evolution of correlations in photometric redshifts bins from $0 \lesssim z \lesssim 3$ in the CFDF–PRS, rigorously incorporating the redshift likelihood function for each galaxy. Our results agree with previous measurements at all redshifts, and our errors are commensurate with those in the largest spectroscopic surveys, as expected since the dominant error source is cosmic variance. We conclude the technique is a powerful new tool with which to study galaxy evolution.

Our findings at $z \sim 3$ strongly support a biased structure formation scenario, and are inconsistent with the simple ϵ–models of the growth of structure. Finally, we make a tentative measurement at $z \sim 1.7$ of a high clustering amplitude, similar to that at $z \sim 3$, which conflicts with the predictions of recent semi–analytic models of galaxy formation.

Chapter 8

Summary and Conclusions

8.1   Summary of Results

Evolutionary measurements of statistical properties of the galaxy population, such as the redshift distribution, correlation function and luminosity density, will be measured in future surveys with unprecedented precision using galaxy redshifts efficiently determined from broadband photometric measurements. In this Thesis we have described a new survey designed to explore and fully characterize this novel technique, with careful attention paid to a proper treatment of the errors inherent in the method.

The CFDF–PRS is a deep 0.5 square degree *UBVRIZ* imaging survey in three fields containing 55,000 galaxies to $I_{\mathrm{AB}} = 25$, for which we have computed highly accurate photometric redshifts. Our large field sizes and multiple, widely separated lines of sight are far less affected by cosmic variance than previous surveys of similar depth. Our redshift algorithm was designed to incorporate hundreds of spectroscopic CFRS galaxies as a calibration sample to further improve the redshift accuracy. The algorithm produces typical redshift dispersions of only $\sigma/(1+z) \lesssim 0.06$ to $I_{\mathrm{AB}} = 24$ for $z \leq 1.3$ over the full survey area, and to $I_{\mathrm{AB}} = 25$ for $z \gtrsim 2.9$ for our two deepest fields. Our redshift code generates a redshift probability function for each galaxy, which produces confidence intervals consistent with Gaussian statistics. We have quantified the catastrophic error properties of the method using the CFRS spectroscopic sample, which allows us to estimate the systematic errors introduced into our science analyses through the use of photometric redshifts.

We have introduced a new technique to compute the redshift distribution which incorporates the full photometric redshift likelihood function for each galaxy to better reproduce the correct underlying redshift distribution. Direct summation of the likelihoods produces the Bayesian prior which accounts for the fact that all redshifts are not a priori equally likely. No information external to the survey is used

in the Bayesian technique, rather we iterate within our own dataset. We have presented Monte Carlo simulations which prove the validity of the technique and demonstrate that it is a significant improvement over previous methods. We compute the median redshifts of our I_{AB} and R_{AB} redshift distributions, as a function of limiting magnitude and in differential magnitude bins, with an error budget consisting of bootstrap resampled random errors, field–to–field variance and an empirical estimate of the systematic errors due to photometric redshift aliasing. We present our I_{AB} and R_{AB} redshift distributions in tabular form and provide parametrized fits with errors estimated from bootstrap resampling.

Finally we demonstrated how accurate clustering measurements can be made using photometric redshifts. We devised a method to incorporate the redshift likelihood functions into a consistent galaxy weighting scheme. The angular correlation function was measured in various redshift bins, with errors estimated from the field to field variance. We deprojected the angular amplitudes using our measured redshift distributions, and the derived correlation lengths agree with the best measurements from spectroscopic redshift surveys from $0 \lesssim z \lesssim 3$. Finally, we have made an intriguing detection of strong clustering at $z \sim 1.7$.

8.2   Conclusions and Future Work

This Thesis has conclusively demonstrated that photometric redshifts can and should be used for any statistical measurements of the galaxy population for which the redshift accuracy is not the leading source of error. We have specifically demonstrated this for the redshift distribution and the evolution of galaxy clustering, in which the number of fields and the field size are far more important factors, provided the redshifts have accuracies similar to those in the present work. In fact, we have demonstrated that cosmic variance remains the leading uncertainty in both measurements even on $30'$ scales. That this fact was not fully appreciated before this work is evidenced by the design of the two largest ongoing "legacy" spectroscopic redshift surveys, one of which (VVDS) only has a *single* deep field $2°$ across, and the other (DEEP2) which has four fields with dimensions between $15'–30' \times 2°$. As such, these surveys will not significantly improve upon the CFDF–PRS results presented here.

We draw several conclusions about the clustering evolution of galaxies based on our analysis described in Chapter 7. The two most robust conclusions are (1) the simple ϵ–models describing the evolution of correlations are incorrect, and (2) the paradigm of biased galaxy formation is strongly supported. With the exception of the stable clustering ($\epsilon = -1.2$) model, the ϵ–models all predict lower correlation lengths at $z \sim 3$ than locally. Our measurement confirms the high $z \sim 3$ clustering amplitude seen by other workers, repudiating the ϵ–models and adding to the evidence for biased galaxy formation. We

also observe a small but significant decline in the correlation function to $z \lesssim 0.8$, which rules out the stable clustering ϵ–model. The correlation function begins to rise at $z \sim 1$ and we find a surprisingly large clustering amplitude at $z \sim 1.7$ consistent with the $z \sim 3$ results. Our results are in agreement with the largest spectroscopic clustering measurements in all redshift regimes where they exist. We defer a detailed theoretical interpretation of the $z \sim 1.7$ measurement, which is in apparent contradiction with most biased galaxy formation models, until it can be independently confirmed.

Future goals for the CFDF–PRS dataset include demonstrating the luminosity dependence of clustering at $z \sim 1$, as well as measuring the dependence of the slope and amplitude on galaxy type. These measurements are in progress and the results thus far agree with extrapolations of lower redshift surveys. In addition, we are currently working on a measurement of the luminosity function evolution, as a function of spectral type, with the aim of computing the evolution of the UV luminosity density since $z \sim 1.3$ and at $z \gtrsim 2.9$. Finally, using these luminosity functions we can measure the evolution of correlations in evolution–corrected volume limited samples since $z \sim 1.3$.

The next big improvement will come from larger surveys exploiting the same methodology we have developed in this Thesis, specifically the CFHT and SIRTF Legacy Surveys. Using accurate photometric redshifts the CFHTLS will measure the redshift distribution and correlation evolution to $z \sim 1.3$ in imaging spanning 170 deg². The ~ 65 deg² SWIRE SIRTF Legacy Survey, along with a slightly deeper 10 deg² guaranteed–time project (the SIRTF Shallow Survey) will allow the important $1.5 < z < 2.5$ regime to be studied using mass–selected samples.

We conclude by returning to our original goal for this Thesis, to determine the applicability of the photometric redshift surveys as an alternative to traditional spectroscopic surveys. We point out that our single survey, carried out on a 4–m telescope, has produced clustering measurements equivalent, in terms of amplitude and accuracy, to the CNOC2, DEEP2 and the Steidel LBG samples combined. In addition, we have also made the first clustering measurement of the general galaxy population at $z \sim 1.7$, which, if confirmed, may offer new insights into the formation history of galaxies.

References

Adelberger, K. L., Steidel, C. C., Shapley, A. E., and Pettini, M. 2003, *ApJ,* **584**, 45

Arnouts, S., Cristiani, S., Moscardini, L., Matarrese, S., Lucchin, F., Fontana, A., and Giallongo, E. 1999, *MNRAS,* **310**, 540

Arnouts, S., et al. 2002, *MNRAS,* **329**, 355

Bacon, D. J., Massey, R. J., Refregier, A. R., and Ellis, R. S. 2003, *MNRAS,* **344**, 673

Bahcall, J. N. and Soneira, R. M. 1980, *ApJS,* **44**, 73

Bardeen, J. M., Bond, J. R., Kaiser, N., and Szalay, A. S. 1986, *ApJ,* **304**, 15

Baugh, C. M., Benson, A. J., Cole, S., Frenk, C. S., and Lacey, C. G. 1999, *MNRAS,* **305**, L21

Baum, W. A. 1962, in *IAU Symp. 15: Problems of Extra-Galactic Research,* (New Yok: Macmillan), p. 390

Benítez, N. 2000, *ApJ,* **536**, 571

Bertin, E. and Arnouts, S. 1996, *A&AS,* **117**, 393

Blanton, M. R., et al. 2003, *ApJ,* **592**, 819

Broadhurst, T. J., Ellis, R. S., Koo, D. C., and Szalay, A. S. 1990, *Nature* **343**, 726

Brodwin, M., Lilly, S., and Crampton, D. 1999, in *ASP Conf. Ser. 191, Photometric Redshifts and the Detection of High Redshift Galaxies,* ed. Weymann, R. J. et al. (San Francisco: ASP), 105

Brown, M. L., Taylor, A. N., Bacon, D. J., Gray, M. E., Dye, S., Meisenheimer, K., and Wolf, C. 2003, *MNRAS,* **341**, 100

Budavári, T., et al. 2003, *ApJ,* **595**, 59

Carlberg, R. G., Yee, H. K. C., Morris, S. L., Lin, H., Hall, P. B., Patton, D., Sawicki, M., and Shepherd, C. W. 2000, *ApJ,* **542**, 57

Chen, H., et al. 2002, *ApJ,* **570**, 54

Christian, C. A., Adams, M., Barnes, J. V., Hayes, D. S., Siegel, M., Butcher, H., and Mould, J. R. 1985, *PASP,* **97**, 363

Cohen, J. G., Hogg, D. W., Blandford, R., Cowie, L. L., Hu, E., Songaila, A., Shopbell, P., and Richberg, K. 2000, *ApJ,* **538**, 29

Coil, A. L., et al. 2004, *ApJ,* **609**, 525

Coleman, G. D., Wu, C.-C., and Weedman, D. W. 1980, *ApJS,* **43**, 393

Colless, M., et al. 2001, *MNRAS,* **328**, 1039

Connolly, A. J., et al. 2002, *ApJ,* **579**, 42

Connolly, A. J., Szalay, A. S., Dickinson, M., Subbarao, M. U., and Brunner, R. J. 1997, *ApJ,* **486**, L11

Crampton, D., Le Fèvre, O., Lilly, S. J., and Hammer, F. 1995, *ApJ,* **455**, 96 (**CFRS5**)

Csabai, I., et al. 2003, *AJ,* **125**, 580

Cuillandre, J., Luppino, G. A., Starr, B. M., and Isani, S. 2000, in *Proc. SPIE Vol. 4008, Optical and IR Telescope Instrumentation and Detectors,* ed. Iye, M. & Moorwood, A. F., 1010

Davis, M., et al. 2003, in *Proceedings of the SPIE, Vol. 4834, Discoveries and Research Prospects from 6- to 10-Meter-Class Telescopes II,* ed. Guhathakurta, P., 161

Davis, M., Huchra, J., Latham, D. W., and Tonry, J. 1982, *ApJ,* **253**, 423

Davis, M. and Peebles, P. J. E. 1983, *ApJ,* **267**, 465

Fernández–Soto, A., Lanzetta, K. M., Chen, H., Pascarelle, S. M., and Yahata, N. 2001, *ApJS,* **135**, 41

Fernández-Soto, A., Lanzetta, K. M., Chen, H.-W., Levine, B., and Yahata, N. 2002, *MNRAS,* **330**, 889

Firth, A. E., et al. 2002, *MNRAS,* **332**, 617

Fontana, A., et al. 1999, *A&A,* **343**, L19

Foucaud, S., McCracken, H. J., Le Fèvre, O., Arnouts, S., Brodwin, M., Lilly, S. J., Crampton, D., and Mellier, Y. 2003, *A&A,* **409**, 835

Gardner, J. P. and Satyapal, S. 2000, *AJ,* **119**, 2589

Gehrels, N. 1986, *ApJ,* **303**, 336

Glazebrook, K., et al. 2003, in *IAU Sympsium 216*

Glazebrook, K. and Bland-Hawthorn, J. 2001, *PASP,* **113**, 197

Groth, E. J., Kristian, J. A., Lynds, R., O'Neil, E. J., Balsano, R., Rhodes, J., and WFPC-1 IDT 1994, *BAAS,* **26**, 1403

Groth, E. J. and Peebles, P. J. E. 1977, *ApJ,* **217**, 385

Gwyn, S. D. J. 1995, *Master's thesis*, MS Thesis, University of Victoria (1995)

Gwyn, S. D. J. and Hartwick, F. D. A. 1996, *ApJ,* **468**, L77

Hamana, T., et al. 2003, *ApJ,* in press (astro–ph/0210450)

Hamilton, A. J. S. 1993, *ApJ,* **417**, 19

Hogg, D. W. 1999, astro-ph/9905116

Hogg, D. W., Cohen, J. G., and Blandford, R. 2000, *ApJ,* **545**, 32

Hogg, D. W., et al. 1998, *AJ* **115**, 1418

Hogg, D. W., Pahre, M. A., McCarthy, J. K., Cohen, J. G., Blandford, R., Smail, I., and Soifer, B. T. 1997, *MNRAS,* **288**, 404

Jing, Y. P. 1998, *ApJ,* **503**, L9

Kaiser, N. 1984, *ApJ* **284**, L9

Kaiser, N. and Peacock, J. A. 1991, *ApJ,* **379**, 482

Karkut, A. 1998, PhD thesis, University of Cambridge

Kauffmann, G., Colberg, J. M., Diaferio, A., and White, S. D. M. 1999, *MNRAS,* **307**, 529

Kinney, A. L., Calzetti, D., Bohlin, R. C., McQuade, K., Storchi–Bergmann, T., and Schmitt, H. R. 1996, *ApJ,* **467**, 38

Koo, D. C. 1985, *AJ,* **90**, 418

Kurucz, R. 1996, *CD-ROM No. 13, GSFC*

Landolt, A. U. 1992, *AJ,* **104**, 340

Landy, S. D. and Szalay, A. S. 1993, *ApJ,* **412**, 64

Le Fèvre, O., Hudon, D., Lilly, S. J., Crampton, D., Hammer, F., and Tresse, L. 1996, *ApJ,* **461**, 534

Le Fèvre, O., et al. 2003, *A&A,* submitted (astro–ph/0306252)

Lee, A. T., et al. 2001, *ApJ,* **561**, L1

Lilly, S. J., Cowie, L. L., and Gardner, J. P. 1991, *ApJ,* **369**, 79

Lilly, S. J., Hammer, F., Le Fèvre, O., and Crampton, D. 1995a, *ApJ,* **455**, 75

Lilly, S. J., Le Fèvre, O., Crampton, D., Hammer, F., and Tresse, L. 1995b, *ApJ,* **455**, 50

Lilly, S. J., Le Fèvre, O., Hammer, F., and Crampton, D. 1996, *ApJ,* **460**, L1

Lilly, S. J., Tresse, L., Hammer, F., Crampton, D., and Le Fèvre, O. 1995c, *ApJ,* **455**, 108

Limber, D. N. 1954, *ApJ,* **119**, 655

Lin, H., Yee, H. K. C., Carlberg, R. G., Morris, S. L., Sawicki, M., Patton, D. R., Wirth, G., and Shepherd, C. W. 1999, *ApJ,* **518**, 533

Loh, E. D. and Spillar, E. J. 1986, *ApJ,* **303**, 154

Loveday, J., Maddox, S. J., Efstathiou, G., and Peterson, B. A. 1995, *ApJ,* **442**, 457

Madau, P. 1995, *ApJ,* **441**, 18

Madau, P., Ferguson, H. C., Dickinson, M. E., Giavalisco, M., Steidel, C. C., and Fruchter, A. 1996, *MNRAS,* **283**, 1388

Magliocchetti, M. and Maddox, S. J. 1999, *MNRAS,* **306**, 988

Maoli, R., Van Waerbeke, L., Mellier, Y., Schneider, P., Jain, B., Bernardeau, F., Erben, T., and Fort, B. 2001, *A&A,* **368**, 766

McCracken, H. J., Le Fèvre, O., Brodwin, M., Foucaud, S., Lilly, S. J., Crampton, D., and Mellier, Y. 2001, *A&A,* **376**, 756 (**CFDF1**)

Metcalfe, N., Shanks, T., Campos, A., McCracken, H. J., and Fong, R. 2001, *MNRAS* **323**, 795

Metzger, M. R., Luppino, G. A., and Miyazaki, S. 1995, *BAAS,* **27**, 1389

Mo, H. J. and White, S. D. M. 1996, *MNRAS,* **282**, 347

Monet, D. G. 1998, *BAAS,* **30**, 1427

Netterfield, C. B., et al. 2002, *ApJ,* **571**, 604

Norberg, P., et al. 2002a, *MNRAS,* **332**, 827

Norberg, P., et al. 2001, *MNRAS,* **328**, 64

Norberg, P., et al. 2002b, *MNRAS,* **336**, 907

Oke, J. B. 1974, *ApJS,* **27**, 21

Peebles, P. J. E. 1993, *Principles of physical cosmology,* Princeton Series in Physics, Princeton, NJ: Princeton University Princeton Series in Physics, Princeton, NJ: Princeton University Press

Pen, U., Lu, T., van Waerbeke, L., and Mellier, Y. 2003, *MNRAS,* **346**, 994

Phleps, S. and Meisenheimer, K. 2003, *A&A,* **407**, 855

Porciani, C. and Giavalisco, M. 2002, *ApJ,* **565**, 24

Postman, M., Lauer, T. R., Szapudi, I. ., and Oegerle, W. 1998, *ApJ,* **506**, 33

Pryke, C., Halverson, N. W., Leitch, E. M., Kovac, J., Carlstrom, J. E., Holzapfel, W. L., and Dragovan, M. 2002, *ApJ,* **568**, 46

Réfrégier, A., Rhodes, J., and Groth, E. J. 2002, *ApJ,* **572**, L131

Sawicki, M. and Yee, H. K. C. 1998, *AJ,* **115**, 1329

Sawicki, M. J., Lin, H., and Yee, H. K. C. 1997, *AJ,* **113**, 1

Schlegel, D. J., Finkbeiner, D. P., and Davis, M. 1998, *ApJ,* **500**, 525

Shectman, S. A., Landy, S. D., Oemler, A., Tucker, D. L., Lin, H., Kirshner, R. P., and Schechter, P. L. 1996, *ApJ,* **470**, 172

Shepherd, C. W., Carlberg, R. G., Yee, H. K. C., Morris, S. L., Lin, H., Sawicki, M., Hall, P. B., and Patton, D. R. 2001, *ApJ,* **560**, 72

Smail, I., Hogg, D. W., Yan, L., and Cohen, J. G. 1995, *ApJ,* **449**, L105

Somerville, R. S., Lee, K., Ferguson, H. C., Gardner, J. P., Moustakas, L. A., and Giavalisco, M. 2003, *ApJ,* in press (astro–ph/0309071)

Spergel, D. N., et al. 2003, *ApJS,* **148**, 175

Steidel, C. C., Adelberger, K. L., Giavalisco, M., Dickinson, M., and Pettini, M. 1999, *ApJ,* **519**, 1

Steidel, C. C., Adelberger, K. L., Shapley, A. E., Pettini, M., Dickinson, M., and Giavalisco, M. 2003, *ApJ,* **592**, 728

Steidel, C. C., Giavalisco, M., Pettini, M., Dickinson, M., and Adelberger, K. L. 1996, *ApJ,* **462**, L17

Szalay, A. S., Connolly, A. J., and Szokoly, G. P. 1999, *AJ,* **117**, 68

Tonry, J. and Davis, M. 1979, *AJ,* **84**, 1511

Van Waerbeke, L., Mellier, Y., Pelló, R., Pen, U.-L., McCracken, H. J., and Jain, B. 2002, *A&A,* **393**, 369

Van Waerbeke, L., et al. 2001, *A&A,* **374**, 757

Weynmann, R. J., Storrie–Lombardi, L. J., Sawicki, M., and Brunner, R. J. 1999, in *ASP Conf. Ser. 191 — Photometric Redshifts and the Detection of High Redshift Galaxies*

Williams, R. E., et al. 1996, *AJ,* **112**, 1335

Yasuda, N., et al. 2001, *AJ,* **122**, 1104

Yee, H. K. C. 1998, in *Proceeding of the Xth Rencontres des Blois: Birth of Galaxies* ed. Guiderdoni, B. et al. (astro–ph/9809347)

Yee, H. K. C., Ellingson, E., and Carlberg, R. G. 1996, *ApJS,* **102**, 269

Yee, H. K. C., et al. 2000, *ApJS,* **129**, 475

York, D. G., et al. 2000, *AJ,* **120**, 1579

Zehavi, I., et al. 2002, *ApJ,* **571**, 172

Appendix A

Examples of Reduction Procedures

A.1   Superflat Algorithm

As a demonstration of the method of generating superflats discussed in Section 2.2.2, in Figure A.1 we present before and after science images in two UH8k chips. These images show different fields observed the same night. A superflat constructed of a simple median of all the frames in the I–band filter results in severe ghosting in the vicinity of bright, extended objects in each field (foreground chips). Application of the method of Section §2.2.2 prevents the ghosting from occurring by masking out the objects responsible for it (background chips).

A.2   De–Fringing Algorithm

Figure A.2 shows before and after images of the defringing process in the Z–band. In the CFDF images the fringing pattern is reduced from a $\sim 10\%$ amplitude of variations to $\lesssim 0.5\%$, as is shown for two chips in this Figure.

A.3   Astrometry

Figure A.3 shows an example of computing the astrometric solution using the USNO standard stars. The top panel shows a single astrometrically corrected CFH12k exposure, with USNO stars overplotted. The bottom panel shows the WCS solution in a single chip, where the blue circles represent stars whose (α, δ) positions are well fit by a third order polynomial in (x,y) pixel values, and the red stars are outliers, typically caused by improper centering due to saturation or proper motions of these nearby stars.
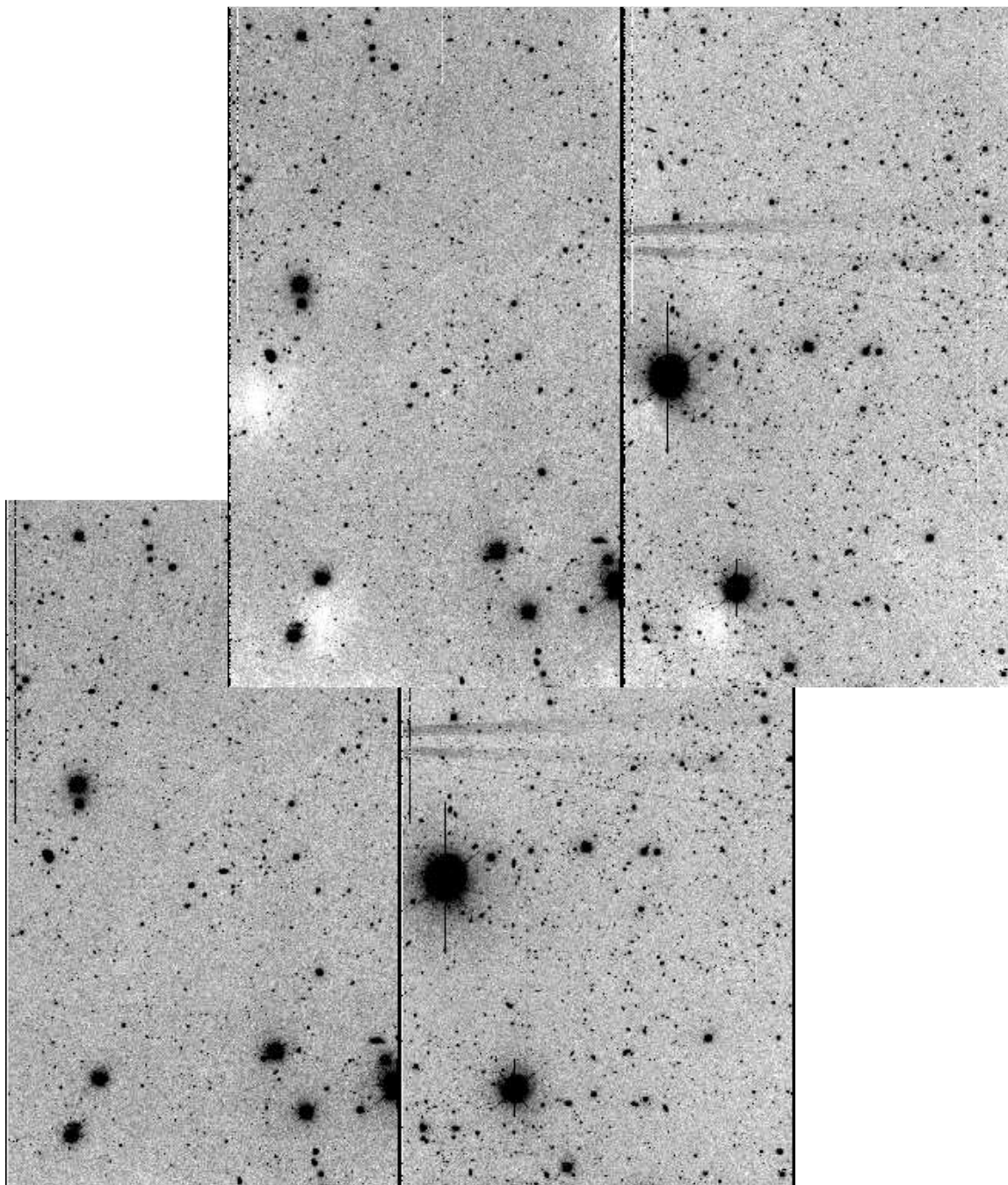
Figure A.1 Example of improvement in flatfielding using the algorithm of Section 2.2.2 (background chips), compared with a simple median of the science frames (foreground chips). The sky background variations are reduced from $\sim 5\%$ to $\sim 0.1\% - 0.3\%$.
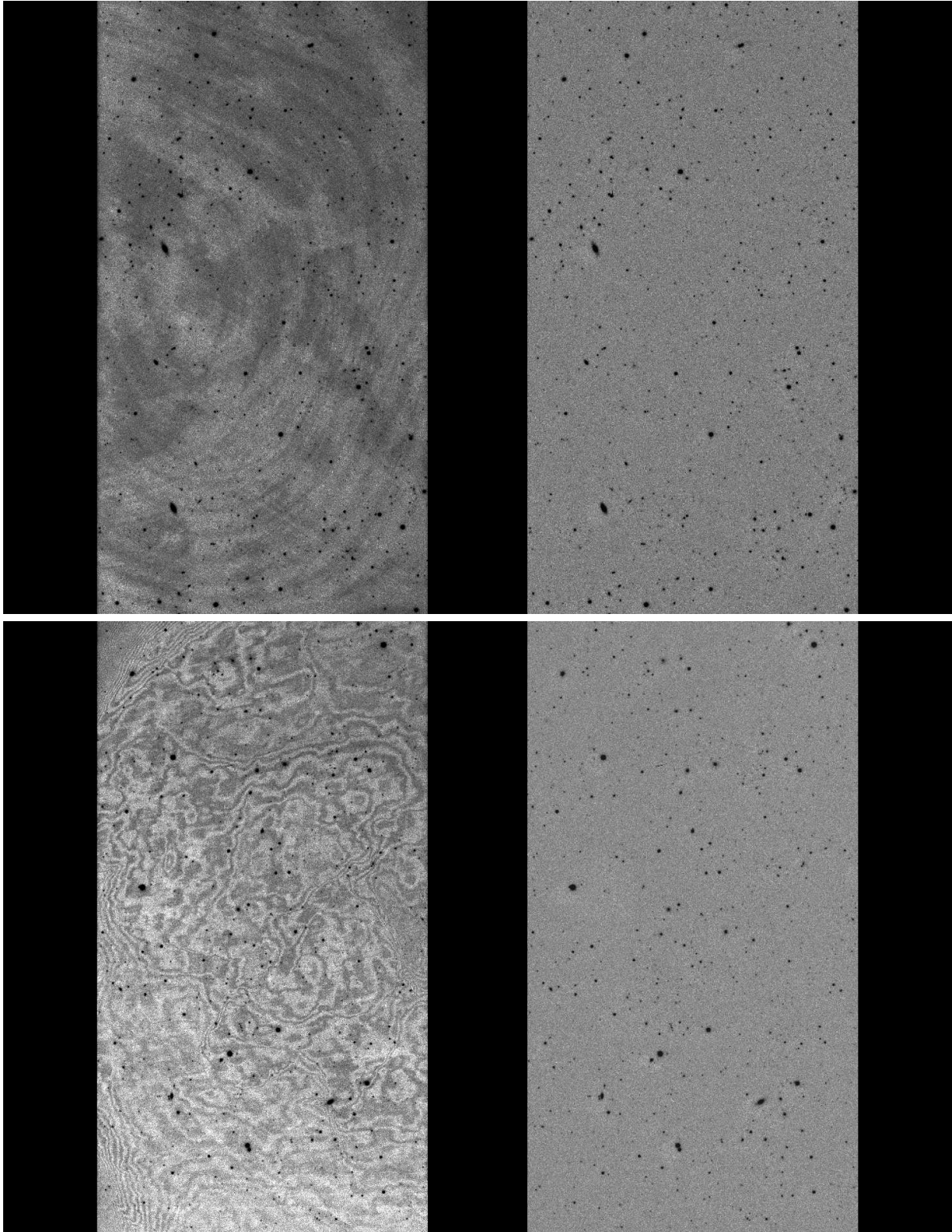
Figure A.2 Examples of the de–fringing algorithm. Although some of the Z–band fringing was quite substantial, as shown in this Figure, the algorithm described in Section §2.2.3 worked remarkably well. The fringing residuals were reduced from $\sim 10\%$ to below 0.5%.
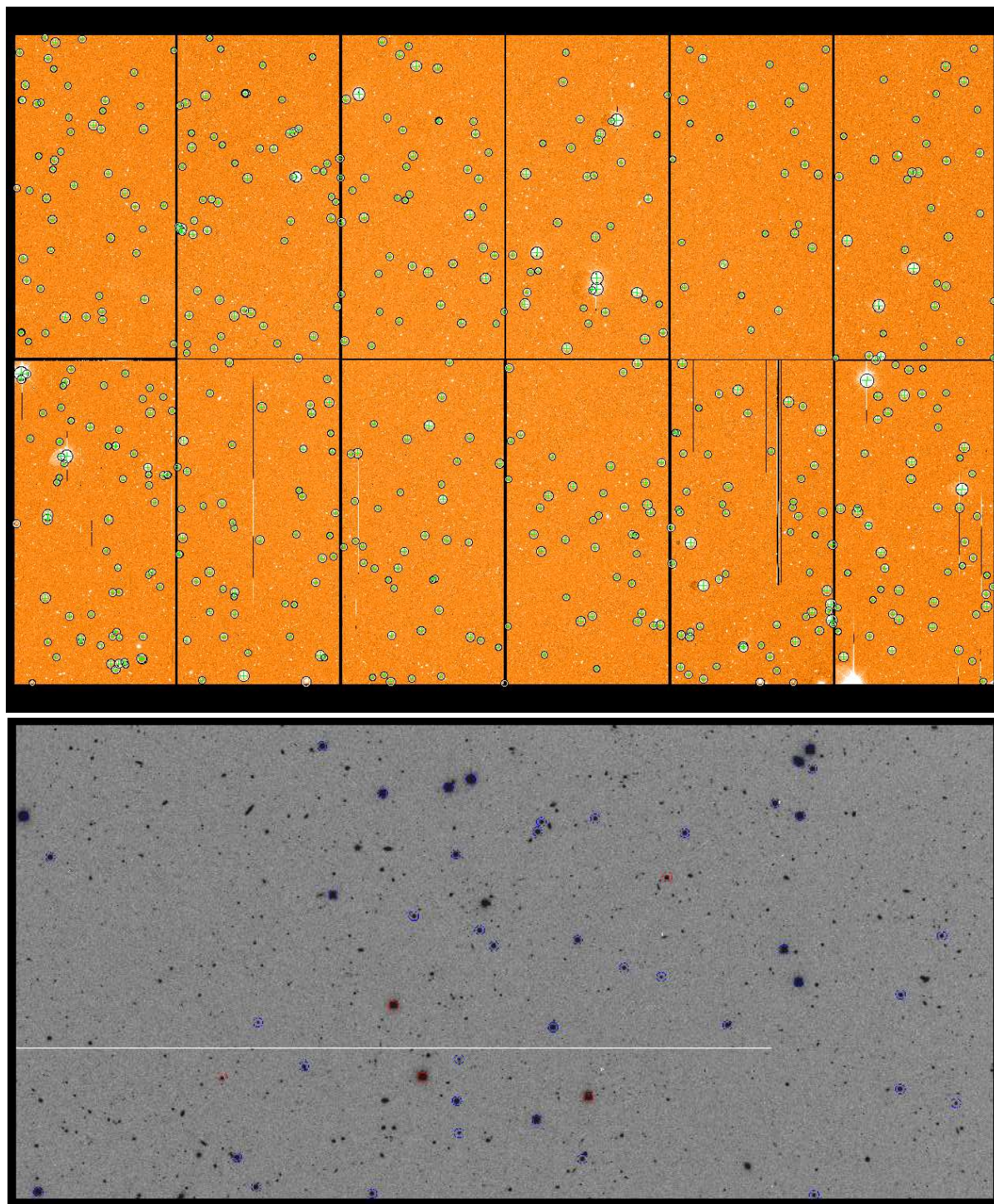
Figure A.3 The top panel shows the USNO stars plotted on a single astrometrically corrected CFH12k exposure. The bottom panel shows the solution in a single chip, including the rejection of some USNO stars due to proper motions and/or saturation.

Appendix B

Analysis Techniques

B.1   Faint Image Simulations

This technique, used in Sections §3.4.1 and §4.3, allows us to accurately simulate what specific stars or galaxies would look like if observed at much fainter flux levels. The technique consists of multiplying an image containing the objects in question by a factor f, translating the resultant image by several (~ 10) arcminutes and adding it back to the original image, with f chosen such that the target objects become Δm magnitudes fainter. The procedure is slightly more involved due to the necessity of maintaining the original noise properties of the image.

The noise level, N, in this process undergoes the transformation

$$N \to \sqrt{N^2 + (f \times N)^2} = N\sqrt{1 + f^2}, \tag{B.1}$$

whereas the signal, S, in the objects transforms as

$$S \to f \times S. \tag{B.2}$$

To keep the noise level constant we divide by $\sqrt{1 + f^2}$, leaving only N as in the original image. The effect of this operation on the new object signal is:

$$f \times S \to \frac{f}{\sqrt{1 + f^2)}} \times S \equiv F \times S \tag{B.3}$$

Therefore to achieve a multiplicative factor, F, on the original objects, we have to apply our method using the scale factor f from Equation B.3. Solving for f:

$$f = \frac{F}{\sqrt{1 - F^2}} \tag{B.4}$$

So to produce images fainter by $\Delta m = \{1.0, 1.5, 2.0, 2.5\}$ magnitudes, requiring flux fractions $F = \{0.4, 0.2512, 0.15849, 0.1\}$, we follow the above prescription, first adding translated images scaled by $f = \{0.436436, 0.259521, 0.160507, 0.100504\}$ and then dividing by $\sqrt{1 + f^2}$.

Appendix C

Detailed Comparison of CFDF and CFRS Redshift Distributions

In this Appendix we describe in detail the quantitative comparison between the CFRS and CFDF redshift distributions, in particular the clustering–corrected significance tests. We extend these ideas and apply them to the full $18.5 \leq I_{AB} \leq 24$ redshift distributions to determine the significance of the field–to–field variations within the CFDF–PRS. Unless otherwise stated all distances in this Appendix are comoving, calculated for a $\{\Omega_M = 0.27, \Omega_\Lambda = 0.73\}$ cosmology with $h = 0.71$.

C.1   Statistical Significance of the CFDF/CFRS Variance

As Figure 6.1 shows, the shapes of the redshift distributions in the 3 CFRS fields match extremely well with the CFDF results. In these individual fields the CFRS distributions are normalized to have the same density of objects as in the corresponding CFDF fields. The relative over– and under–densities of objects at $z \sim 0.3$ and $z \sim 0.7$ in the CFRS 22hr field, compared with the full survey $N(z)$, persists in the much larger CFDF. The striking difference between this field and the 03hr field, where the redshift distribution is strongly peaked at $0.6 < z < 0.7$, is also reproduced. The formal K–S results for the two surveys, listed in Table C.1, would seem to indicate that the surveys are marginally inconsistent with each other. However, as Crampton et al. (1995) pointed out, small–scale galaxy clustering reduces the number of truly independent galaxies (an assumption on which the K–S test rests). Each galaxy contributes, on average, more than just one galaxy (itself) to the sample due to this clustering. We have devised an empirical method similar to that used in the CFRS to estimate how this clustering reduces

Table C.1.   Significance of CFDF/CFRS Redshift Distribution Variations.

Field	N	K–S	p
03hr	156	0.154	0.001
14hr	141	0.109	0.066
22hr	94	0.137	0.053
All Common Fields[a]	391	0.077	0.018
All Fields[b]	582	0.088	0.001

[a]Includes the fields common to both surveys.

[b]Includes all five original CFRS survey fields.

the effective number of independent galaxies.

We have computed the number of pairs as a function of separation in redshift space. At small scales, we expect an excess of pairs due to clustering, whereas at large redshift separations the number of pairs should drop due to the steeply declining correlation function and the variation of the underlying redshift distribution. An example for the 03hr field is shown in the middle panel of Figure C.1. The top panel of the Figure shows the $18.5 \leq I_{AB} \leq 22.5$ CFRS redshift distribution in the this field. The bottom panel is a zoom in on the smallest ($\Delta z \leq 0.10$) separations and clearly shows the excess pairs due to small–scale clustering. We estimate the excess number of pairs by subtracting the expected number of pairs, as estimated from the average in the region $0.01 \leq \Delta z \leq 0.05$ (delimited by the red arrows), from the total number of pairs at separations smaller than $\Delta z \leq 0.005$ (indicated by the blue arrow). Both scales were empirically determined from Figure C.1 subject to the joint constraints of the CFRS redshift accuracy ($\sigma_z \sim 0.002$) and the rapid decline of small–scale clustering power. Large–scale clustering beyond ~ 14 Mpc ($10\ h^{-1}$ Mpc) is virtually negligible (e.g. Carlberg et al. 2000), and our inclusion limit of $\Delta z \leq 0.005$ is greater than this physical separation for $0 \lesssim z \lesssim 1$, meaning we are including all the excess pairs. The regime used to estimate the Poisson contribution to the pair counts is well outside the non–linear clustering regime — at these redshifts our lower limit of $\Delta z \geq 0.01$ corresponds to over ~ 25 Mpc separations. The upper limit (≤ 0.05) is quite modest so as to minimize differential volume effects and $N(z)$ variation, effects which are expected to be important for larger separations since we are summing the pair counts from galaxies over a huge redshift range.

Dividing the excess number of pairs by the number of galaxies in the field yields the excess number of galaxies per galaxy. Adding 1 to this result produces the average number of galaxies per galaxy,
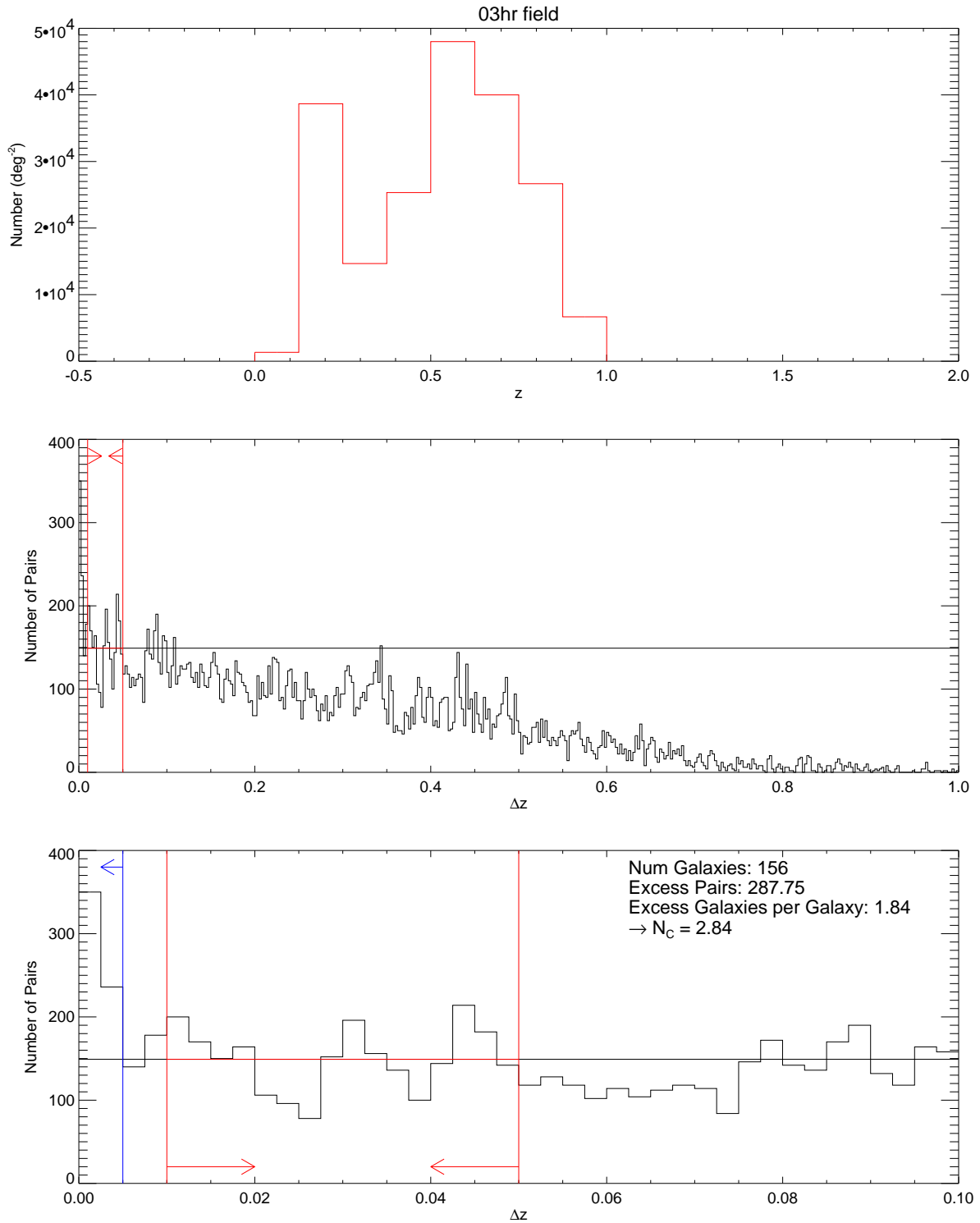
Figure C.1 Estimation of N_C in the CFRS. *Top:* CFRS 03hr redshift distribution; *Middle:* 1–D redshift–space pair counts; *Bottom:* Zoom in on pair counts at $z \leq 0.10$. The counts inside $\Delta z \leq 0.005$ minus the average at $0.01 \leq z \leq 0.05$ are taken to be the excess pairs due to clustering.

Table C.2.   Significance of Clustering–Corrected CFDF/CFRS Redshift Distribution Variations.

Field	N_C	N_{eff}	K–S	p
03hr	2.84	55	0.154	0.134
14hr	2.25	63	0.109	0.428
22hr	1.85	51	0.137	0.275
All Common Fields	2.17	180	0.077	0.227
All Fields	1.74	334	0.080	0.026

N_C. In the limit of no excess pairs $N_C = 1$ as expected in a Poissonian distribution. Dividing the number of galaxies in each field by N_C yields an estimate of the correct number of *independent* galaxies. This number is then used as the effective number of galaxies in the K–S test. Table C.2 shows the clustering–corrected results of the statistical comparison between the surveys.

The probabilities indicate the likelihood of the distributions being consistent with having been randomly drawn from the same underlying redshift distribution. The ideal probability, in some sense, is $1 - 0.68 = 0.32$, corresponding to a 1σ agreement between two realizations of a Poisson point process. Clearly the redshift distributions in each CFDF/CFRS field and over all common fields are completely consistent with each other.

C.2   Field to Field Variations Within the CFDF

An interesting question is whether the different fields in the CFDF are themselves consistent with having been drawn from the same underlying redshift distribution. In the CFRS the obvious field–to–field differences were not statistically significant due to the small number of galaxies involved. However the CFDF contains thousands of galaxies in each field to the CFRS depth. With $30'$ diameter fields and a redshift baseline extending thousands of Mpc (even to the CFRS depth), the CFDF redshift distribution is expected to be reasonably homogeneous from field to field. However, a direct application of the K–S test to the redshift distributions in Figure 6.1 seems to indicate (see Table C.3) that the visually striking differences between the different fields (in particular between the 03hr and 22hr fields) are in fact statistically significant.

In spite of the impressive CFDF field size, the 3–dimensional power spectrum is still being sampled by a "skewer", in which the redshift dimension is much larger than the survey width. In the CFDF–PRS to the CFRS limit of $I_{\mathrm{AB}} \leq 22.5$, the survey depth (taken as the comoving distance at $z_{\mathrm{max}} \sim 1.3$)

Table C.3.   Significance of Field–to–Field $N(z)$ Variations in the CFDF.

Fields	χ^2	p	K–S	p
03hr/14hr	22	0.0	0.12	10^{-20}
03hr/22hr	41	0.0	0.18	10^{-37}
14hr/22hr	33	0.0	0.09	10^{-9}
03hr/All	13	0.0	0.09	10^{-16}
14hr/All	4	10^{-7}	0.04	0.002
22hr/All	16	0.0	0.10	10^{-14}

is over 200 times the field size at the median redshift of $\bar{z} \sim 0.55$. This calls to mind the Broadhurst et al. (1990) paper, discussed in Section §6.3, that claimed to find periodic structure in the Universe on 128 h^{-1} Mpc scales. Kaiser and Peacock (1991) later showed that it was merely a geometrical effect of pencil–beam surveys in which the small scale clumpiness dominates the observed 3–D power spectrum. They conclude that pencil beam surveys are relatively insensitive to power on scales larger than the smallest survey dimension.

The clustering–corrected statistics computed in §C.1 take exactly this effect into account. It is difficult to empirically estimate the N_C factor for the CFDF, since the photometric redshift errors ($\sigma_z \sim 0.06$) completely wash away the small–scale 1–D clustering signal in the z direction. Instead we try to scale the results for the CFRS up to field sizes appropriate to the CFDF. The excess pairs in a given survey is simply the integral of the correlation function over the survey volume

$$N_{\text{Excess Pairs}} \;=\; \Phi^2 \int \int \xi(\vec{r}_{12}) \, dV_1 \, dV_2 \tag{C.1}$$

$$=\; \Phi^2 \int \int \xi(\vec{r}_{12}) \, W(\vec{r}_{12}) \, dV_{12} \, dV \tag{C.2}$$

where Φ is the galaxy number density and $W(\vec{r}_{12})$ is a window function such that $\vec{r}_{12}^{\,2} \, W(\vec{r}_{12})$ gives the probability distribution function of pairs at separation $\vec{r}_{12}$ for a given survey geometry. As an example, the appropriate window function for a circular survey geometry, presented in Porciani and Giavalisco (2002), is a spherical Bessel function. For both the CFDF and CFRS, the proper window functions would be analytically intractable due to masked regions in the former and a complicated sampling pattern in the latter. As we are only interested in deriving a scaling relation we take $W(\vec{r}_{12})$ for both surveys to be simple Heaviside functions, $\Theta(|\vec{r}_{12}| < R)$, equal to unity inside the survey diameter R and zero outside:

$$N_{\text{Excess Pairs}} \;\approx\; \Phi^2 \int \int \xi(\vec{r}_{12}) \, \Theta(|\vec{r}_{12}| < R) \, dV_{12} \, dV \tag{C.3}$$

$$\approx \quad \Phi^2 V \int \xi(\vec{r}_{12})\, \Theta(|\vec{r}_{12}| < R)\, dV_{12}. \tag{C.4}$$

We rewrite Equation C.4 in terms of the components of $\vec{r}_{12}$ along (r_π) and perpendicular (r_p) to the redshift direction

$$N_{\text{Excess Pairs}} \approx 2\pi\, r_0^\gamma\, \Phi^2 V \int_0^{r_\pi^{\max}} \int_0^R (r_p^2 + r_\pi^2)^{-\gamma/2}\, r_p\, dr_p\, dr_\pi \tag{C.5}$$

where we have assumed a power law form for $\xi(r) = (r/r_o)^{-\gamma}$. Dividing by the number of galaxies in the field (ΦV) produces the specific number of excess galaxies, which is the very quantity we measured empirically in the CFRS:

$$N_{\text{Specific Excess Galaxies}} \approx 2\pi\, r_0^\gamma\, \Phi \int_0^{r_\pi^{\max}} \int_0^R (r_p^2 + r_\pi^2)^{-\gamma/2}\, r_p\, dr_p\, dr_\pi. \tag{C.6}$$

We have integrated this equation to a maximum $r_\pi^{\max} = 16$ Mpc corresponding to $\Delta z = 0.005$ at $\bar{z} \sim 0.55$, in analogy with the empirical method of Section §C.1. For simplicity we have adopted a correlation scale length $r_0 = 7$ Mpc ($5\ h^{-1}$ Mpc) and slope $\gamma = 1.8$ in broad agreement with the results of the largest survey to date in this redshift range (Carlberg et al. 2000), although, not surprisingly, the clustering scale length cancels out in the final scaling relation. Variations in the slope do affect the result, by about 10% for $\delta\gamma \sim 0.1$. However, as we show in Chapter 7, our sample has a measured angular correlation slope quite consistent with $\delta = 0.8$ ($\gamma = 1.8$). Figure C.2 shows the result as a function of the linear field size R. The approximately linear scaling relation in this Figure indicates that the CFDF fields should have N_C factors ~ 2.75 times larger than those empirically determined in the CFRS, assuming the galaxy space densities Φ are the same.

The unusual CFRS sampling pattern, originally motivated for reasons of spectroscopic efficiency, consists of three rows of spectroscopic slits per field with unsampled gaps in between. The survey was never intended to be spatially complete, and in fact only samples about 1 in 3 galaxies, leading to fewer pairs per unit area compared with the CFDF. In the absence of window functions, we account for this effect by scaling by the ratio of the measured mean angular space densities, $\bar{n}$, in the two surveys in each field, listed in Table C.4.

The clustering–corrected K–S test results for the CFDF are listed in Table C.5. The redshift distributions in each field are in perfect agreement with the mean N(z) to this depth. The 03hr and 22hr fields are discrepant with each other at roughly the 2.5 σ level, but both are entirely consistent with the 14hr field. Given the approximate nature of the above calculations, there is no convincing evidence of anisotropies on the scales probed, beyond those attributable to small–scale galaxy correlations. However, those correlations do cause significant N(z) variations on at least 30$'$ scales (~ 30 Mpc at $z = 1$). This
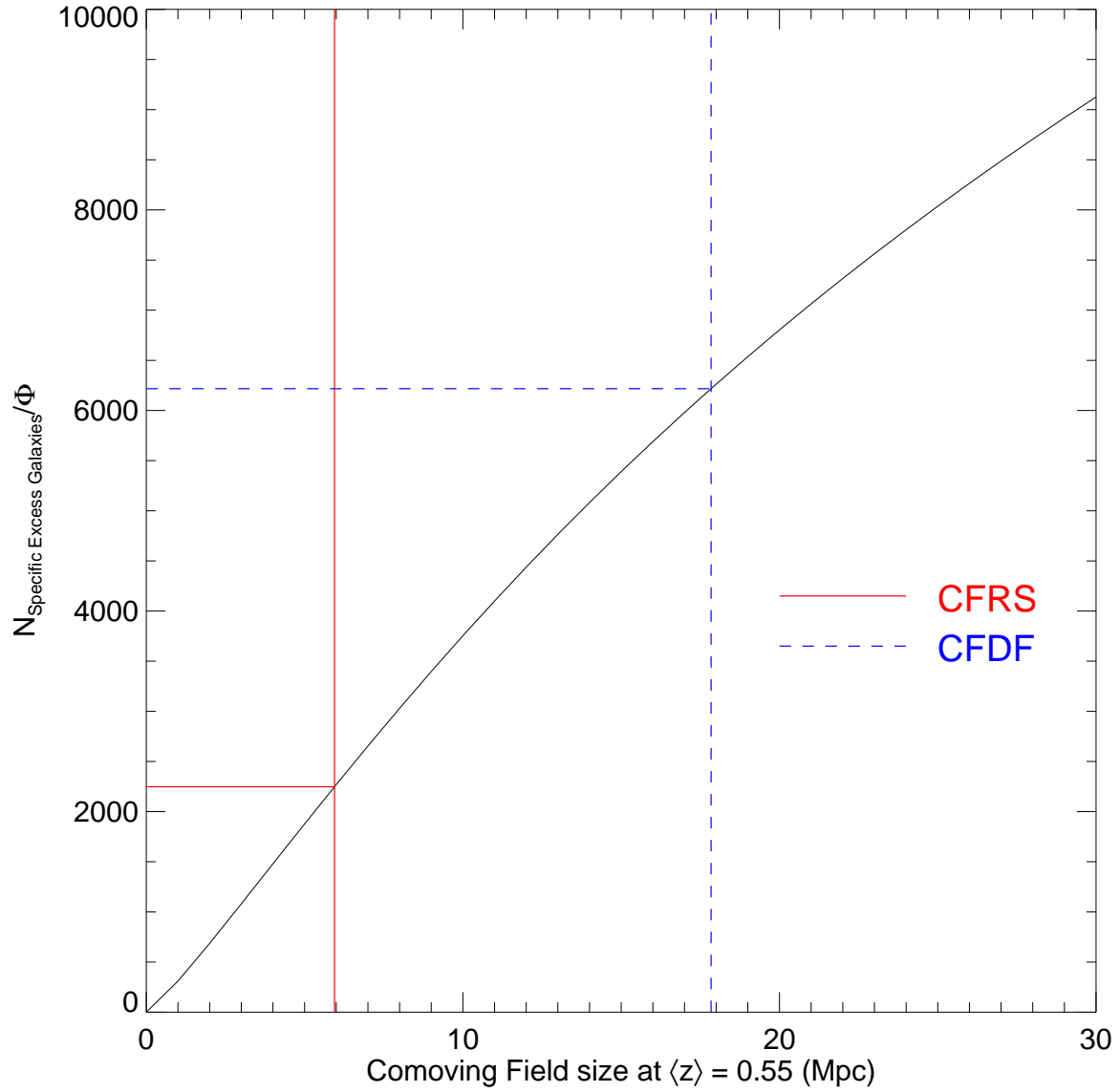
Figure C.2 Scaling of N_C between the CFRS and the CFDF.

study strongly suggests that weak lensing studies using redshift distributions derived from the Hubble Deep Field are drastically underestimating their systematic errors.

Table C.4.   Number of Galaxies, Densities, and Clustering Correction Factors N_C for CFDF Fields to $I_{AB} \leq 22.5$ and $I_{AB} \leq 24$.

CFDF Field	Area (arcmin^2)	N_{gal}	$\bar{n}$ (arcmin^{-2})	η^{a} ($\bar{n}$ Ratio)	$N_C{}^{b}$
03hr	622.3	3384 (10908)	5.44 (17.53)	3.49 (11.24)	18.8 (58.3)
14hr	631.9	3474 (10636)	5.50 (16.83)	3.90 (11.94)	14.5 (42.3)
22hr	371.0	2002 (6386)	5.40 (17.21)	5.74 (18.31)	14.5 (44.1)
All	1625.2	8860 (27930)	5.45 (17.19)	4.19 (13.22)	14.6 (43.8)

[a]Ratio of CFDF/CFRS angular space densities, $\eta \equiv \bar{n}_{\mathrm{CFDF}}/\bar{n}_{\mathrm{CFRS}}$

[b]To be exact, $N_C = (N_C^{\mathrm{CFRS}} - 1) \times \eta \times 2.77 + 1$, where 2.77 is the scaling relation factor derived in Equation C.6

Note. — Values in brackets are for the $I_{AB} \leq 24$ sample.

Table C.5.   Significance of Clustering–Corrected Field–to–Field $N(z)$ Variations in the CFDF.

Fields	$I_{AB} \leq 22.5$		$I_{AB} \leq 24$	
	K–S	p	K–S	p
03hr/14hr	0.12	0.11	0.12	0.10
03hr/22hr	0.18	0.01	0.10	0.42
14hr/22hr	0.09	0.44	0.08	0.58
03hr/All	0.09	0.25	0.06	0.59
14hr/All	0.04	0.96	0.06	0.53
22hr/All	0.10	0.19	0.04	0.99

Appendix D

Derivation of Relativistic Limber Equation

In this Appendix we derive the expression for the relativistic Limber equation valid in all spatially flat cosmologies. We neglect non–flat world models in light of the overwhelming evidence for $\Omega_{\text{tot}} = 1$ from recent cosmic microwave background experiments (Spergel et al. 2003, Netterfield et al. 2002, Pryke et al. 2002, Lee et al. 2001).

D.1 The Limber Equation

We relate $\omega(\theta)$ and $\xi(r)$ by equating the physical observable, the number of pairs of galaxies at an angular separation θ,

$$\bar{n}^2 \left[1 + \omega(\theta)\right] d\Omega_1 d\Omega_2 = \iint_z \Phi(x_1)\Phi(x_2) \left[1 + \xi(r_{12})\right] dV_1 dV_2, \tag{D.1}$$

where the integral of $\xi(r_{12})$ is taken over all possible redshifts, $\bar{n}$ and $\Phi(x)$ are the angular and real–space galaxy densities, and the subscripts refer to the two galaxies depicted in Figure D.1. The comoving volume element for $\Omega_M + \Omega_\Lambda = 1$ cosmologies is

$$dV = \frac{c}{H_0} \frac{x^2(z)}{E(z)} d\Omega \, dz, \tag{D.2}$$

where the comoving radial coordinate, $x(z)$, is defined as

$$x(z) = \frac{c}{H_0} \int_0^z \frac{dz}{E(z)} \tag{D.3}$$

or in differential form
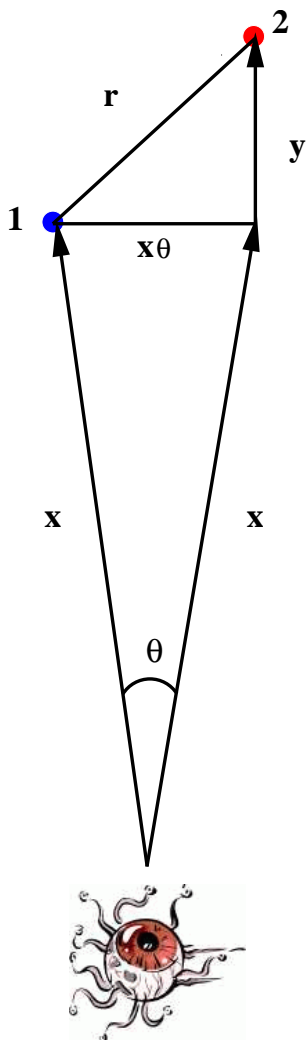
$$dx = \frac{c}{H_0} \frac{dz}{E(z)}. \tag{D.4}$$

Figure D.1 Schematic diagram of a galaxy pair used in the derivation of the Limber equation. Galaxies 1 and 2, separated by a projected angle θ and comoving distance r, at comoving line–of–sight distances x and $u \equiv x + y$ from the observer.

For a zero curvature metric, $\Omega_k = 1 - \Omega_M - \Omega_\Lambda = 0$, we deduce from Equation 7.8 that

$$E(z) = \sqrt{\Omega_M(1+z)^3 + \Omega_\Lambda}. \tag{D.5}$$

Substituting D.4 in D.2 we can therefore write

$$dV = x^2(z)\, dx\, d\Omega \tag{D.6}$$

which makes intuitive sense in a spatially flat Universe. With x as the comoving distance to galaxy 1, and defining

$$u \equiv x + y \tag{D.7}$$

as the comoving distance to galaxy 2 in the small–angle approximation, Equation D.1 becomes

$$\bar{n}^2 \left[1 + \omega(\theta)\right] d\Omega_1 d\Omega_2 \;\; = \;\; \int_{-\infty}^{\infty} \int_{-\infty}^{\infty} \Phi(x)\Phi(u) \left[1 + \xi(r_{12})\right] x^2 \, dx \, d\Omega_1 \, u^2 \, du \, d\Omega_2 \tag{D.8}$$

$$= \;\; \left[\int_{-\infty}^{\infty} \Phi(x) \, x^2 \, dx\right] \left[\int_{-\infty}^{\infty} \Phi(u) \, u^2 \, du\right] d\Omega_1 d\Omega_2 \, +$$

$$\int_{-\infty}^{\infty} \int_{-\infty}^{\infty} \Phi(x)\Phi(u)\xi(r_{12}) \, x^2 \, dx \, u^2 \, du \, d\Omega_1 d\Omega_2. \tag{D.9}$$

Since

$$\bar{n} = \int_{-\infty}^{\infty} \Phi(x) \, x^2 \, dx \tag{D.10}$$

the random component on both sides of the equation cancels out. The remaining integrals over the correlation function can be simplified somewhat by taking advantage of the fact that the galaxy selection function or space density, $\Phi(x)$, varies much more slowly than $\xi(r)$ which is sharply peaked at $x \approx u$ and quickly falls to zero when this condition does not hold. Therefore we write

$$\bar{n}^2 \omega(\theta) \;\; = \;\; \int_{-\infty}^{\infty} \int_{-\infty}^{\infty} \Phi^2(x)\xi(r_{12}) \, x^4 \, dx \, du. \tag{D.11}$$

Approximating the correlation function as a power law, $\xi(r) = (r/r_0)^{-\gamma}$, and expressing the comoving separation between the two galaxies in terms of the components parallel and perpendicular to the plane of the sky

$$r_{12} = \sqrt{x^2\theta^2 + y^2} = \sqrt{x^2\theta^2 + (u - x)^2}, \tag{D.12}$$

we can write

$$\bar{n}^2 \omega(\theta) \;\; = \;\; \int_{-\infty}^{\infty} \int_{-\infty}^{\infty} \Phi^2(x)\xi\left(\sqrt{x^2\theta^2 + (u - x)^2}\right) x^4 \, dx \, du \tag{D.13}$$

$$= \;\; \int_{-\infty}^{\infty} \int_{-\infty}^{\infty} \Phi^2(x) \, x^4 \, dx \, \frac{r_0^{\gamma}}{(x^2\theta^2 + (u - x)^2)^{\gamma/2}} \, du \tag{D.14}$$

$$= \;\; \int_{-\infty}^{\infty} \Phi^2(x) \, x^4 \, (x\,\theta)^{-\gamma} r_0^{\gamma} \, dx \int_{-\infty}^{\infty} \frac{1}{(1 + ((u - x)/x\,\theta)^2)^{\gamma/2}} \, du \tag{D.15}$$

We now apply a quick change of variables

$$\eta \;\; \equiv \;\; \frac{u - x}{x\,\theta} \tag{D.16}$$

$$\Rightarrow d\eta \;\; = \;\; \frac{du}{x\,\theta} \tag{D.17}$$

and define a constant, H_γ, as the standard integral

$$H_\gamma \equiv \int_{-\infty}^{\infty} \frac{1}{(1 + \eta^2)^{\gamma/2}} d\eta = \frac{\Gamma[1/2]\,\Gamma[(\gamma - 1)/2]}{\Gamma[\gamma/2]}. \tag{D.18}$$

Thus we arrive at

$$\bar{n}^2 \omega(\theta) = H_\gamma \int_{-\infty}^{\infty} \Phi^2(x) \, x^4 \, (x\,\theta)^{1-\gamma} r_0^{\gamma} \, dx. \tag{D.19}$$

Equating the relation in Equation D.10 to the integral over redshift of the simple redshift distribution, $N(z)$,

$$\bar{n} = \int_{-\infty}^{\infty} \Phi(x)\, x^2\, dx \;=\; \frac{1}{\Omega} \int_{-\infty}^{\infty} N(z)\, dz \tag{D.20}$$

$$\int_{-\infty}^{\infty} \left(\Phi(x)\, x^2\, \frac{dx}{dz} \right) dz \;=\; \frac{1}{\Omega} \int_{-\infty}^{\infty} N(z)\, dz \tag{D.21}$$

$$\Rightarrow \Phi(x)\, x^2\, \frac{dx}{dz} \;=\; \frac{1}{\Omega} N(z) \tag{D.22}$$

$$\Phi^2(x)\, x^4 \;=\; \frac{1}{\Omega^2} N^2(z) \left(\frac{dz}{dx} \right)^2 \tag{D.23}$$

where Ω is the solid angle of the survey. Expressing $\bar{n}$ in terms of $N(z)$ via Equation D.20 and substituting D.23 in D.19 yields

$$\omega(\theta) \;=\; H_\gamma \frac{\int_{-\infty}^{\infty} N^2(z) \left(\frac{dz}{dx} \right)^2 (x\,\theta)^{1-\gamma} r_0^\gamma\, dx}{\left[\int_{-\infty}^{\infty} N(z)\, dz \right]^2} \tag{D.24}$$

$$\;=\; H_\gamma \frac{\int_0^{\infty} N^2(z) \frac{dz}{dx} (x\,\theta)^{1-\gamma} r_0^\gamma\, dz}{\left[\int_0^{\infty} N(z)\, dz \right]^2} \tag{D.25}$$

$$\;=\; \frac{H_0 H_\gamma}{c} \frac{\int_0^{\infty} N^2(z)\, (x\,\theta)^{1-\gamma} r_0^\gamma\, E(z)\, dz}{\left[\int_0^{\infty} N(z)\, dz \right]^2} \tag{D.26}$$

where in the last step we have once again used the comoving radial coordinate in differential form (Equation D.4). Finally we have

$$\omega(\theta) = \frac{H_0 H_\gamma}{c}\, \theta^{1-\gamma} \frac{\int_0^{\infty} N^2(z)\, r_0^\gamma(z)\, [x(z)]^{1-\gamma} E(z)\, dz}{\left[\int_0^{\infty} N(z)\, dz \right]^2} \tag{D.27}$$

as given in Equation 7.6, where we have explicitly noted the redshift dependence of the comoving radial coordinate, $x(z)$, and the comoving correlation length, $r_0^\gamma(z)$.